Lehrstuhl für Umformtechnik und Gießereiwesen
Fakultät für Maschinenwesen
Technische Universität München

A Material Model for Foundry Cores

The Brittle Fracture Behaviour of Chemically-Bound Foundry Sands

Philipp Johnathan Lechner

Vollständiger Abdruck der von der Fakultät für Maschinenwesen der Technischen Universität München zur Erlangung des akademischen Grades eines Doktor-Ingenieurs (Dr.-Ing.) genehmigten Dissertation.

Vorsitzender:
Prof. Dr.-Ing. Michael W. Gee

Prüfer der Dissertation:
1. Prof. Dr.-Ing. Wolfram Volk
2. Prof. Dr. phil. Peter Schumacher

Die Dissertation wurde am 08.02.2021 bei der Technischen Universität München eingereicht und durch die Fakultät für Maschinenwesen am 10.05.2021 angenommen.

Für meine lieben Eltern, die diese Arbeit mit ihrer bedingungslosen
Unterstützung möglich gemacht haben und Marie die Liebe meines Lebens.

Vorwort

Die vorliegende Dissertation entstand während meiner Tätigkeit als wissenschaftlicher Mitarbeiter am Lehrstuhl für Umformtechnik und Gießereiwesen der Technischen Universität München.

Mein besonderer Dank gilt meinem Doktorvater, Herrn Prof. Dr.-Ing. Wolfram Volk, Ordinarius des Lehrstuhls für Umformtechnik und Gießereiwesen der Technischen Universität München, für das außerordentliche Vertrauen, das er seinen Doktoranden in allen Bereichen entgegenbringt. Dieses Vertrauen macht den Lehrstuhl utg zu einem Arbeitsplatz, der seinen Mitarbeitern großartige Möglichkeiten zur persönlichen und fachlichen Entwicklung bietet und den ich jeden Morgen gerne betrete.

Herrn Univ.-Prof. Dipl.-Ing. Dr. phil. Peter Schumacher, Leiter des Lehrstuhls für Gießereikunde an der Montanuniversität Leoben, danke ich für die Übernahme des Korreferats und die aufmerksame Durchsicht der Arbeit. Herrn Prof. Dr.-Ing. Michael W. Gee, Professor für Mechanik auf Höchstleistungsrechnern an der Technischen Universität München, danke ich für die Übernahme des Prüfungsvorsitzes.

Darüber hinaus möchte ich mich bei allen Mitarbeiterinnen und Mitarbeitern des Lehrstuhls bedanken, die mich begleitet und unterstützt haben. Besonders danke ich Herrn Jens Stahl, Herrn Dr.-Ing. Christoph Hartmann, Herrn Thomas Greß, Herrn Florian Ettemeyer, Herrn Dr.-Ing. Benjamin Himmel und Herrn Dr.-Ing. Tim Mittler für die vielen fachlichen Anregungen und die spannenden Diskussionen. Weiterhin bedanke ich mich bei Frau Stefanie Prauser, Frau Marina Ziller, Frau Brigitte Resch, Frau Maria Schmuck, Frau Corinna Sutter, Herrn Tim Schönstädt, Herrn Marco Olbrich-Baier und Herrn Andreas Fuhrmann für die wichtige Arbeit, die Sie am Lehrstuhl leisten. Außerdem danke ich allen Studierenden, insbesondere Frau Anna Luber, Herrn Nils Kraschinski, Herrn Dario Arcuti und Frau Bianca Tananau-Blumenschein, die mich im Rahmen ihrer Tätigkeit als wissenschaftliche Hilfskräfte und ihrer Studienarbeiten bei meiner Forschung unterstützt haben.

Schließlich gilt mein besonderer Dank meinen lieben Eltern und Marie-Kathrin Sekretaruk, die durch ihre Geduld und ihre liebevolle Unterstützung diese Arbeit erst möglich gemacht haben.

München, im Februar 2021 *Philipp Lechner*

Executive Summary

In the last decade, inorganically-bound core materials have gradually replaced their organically-bound pendants in large light-metal foundries, due to stricter environmental laws. Inorganic silicate-based binder systems are utilised to produce foundry cores and moulds with natural sands. The cores are usually produced on core shooting machines, which shape and harden the sand-binder system. After production, they are transported by handling systems and stored until the casting starts. Subsequently, the cores inside of the cast part are destroyed by hammer systems in the "decoring" process. Finally, the resulting used sand is recycled or disposed of. With that step the life-cycle of the foundry core is concluded.

During this whole life-cycle, process problems may arise due to the mechanical material properties of the sand cores. Firstly, the core may be deformed by the handling gripper system. Furthermore, the core might be deformed during the storage time due to creep resulting from its own mass. The decoring process after the casting is challenging with inorganic core materials, since it has to be adapted specifically to the residual material strength of the core and the geometry of the cast part.

All of these problems during the process could be improved with a process optimisation in FEM. However, today's state of the art offers not enough knowledge to implement such simulations, since the necessary material behaviour and properties are unknown. This dissertation fills this research gap and develops methods, which allow the general material behaviour to be determined and the material parameters for specific material models to be quantified. I have developed an acoustic test bench to reach this goal which allows the Young's and shear modulus of core materials to be determined non-destructively. Additionally, several bi-axial test setups for a universal testing machine have been designed, which allow investigation and validation of failure criteria. Furthermore, I developed a novel testing machine which is able to perform bending and compression tests with an additional hydrostatic pressure in a nitrogen atmosphere. This allows to characterise a failure surface at arbitrary points in principal stress space, which can be compared to classical failure criteria.

With these methods a novel failure criterion has been proposed, which combines the weakest-link theory of brittle materials with the Mohr-Coulomb criterion. The material strength is influenced by both, the effective loaded volume (weakest-link theory) and the hydrostatic pressure (Mohr-Coulomb).

To broaden the knowledge of inorganic core materials and their mechanical behaviour, several studies have been performed on the influence of varying binder amount, storage time and humidity. The binder amount has a linear influence on the material strength, while the material strength is increasing after the core shooting with a logarithmic function of the storage time. Rising humidity decreases the material strength considerably.

Furthermore, I studied the creep behaviour of core materials, which has a significant impact on core deformation during storage. The creep of core materials depends on the ratio of the actual load and the material strength, which is influenced by the binder amount and several parameters like hydrostatic pressure, storage time and humidity.

The dissertation closes with an example of a core handling problem at BMW AG. The example gives an insight, how the novel material models can be utilised in an industrial environment for process simulation. At the moment, technical problems with inorganic core materials are being solved with experience and a trial and error process. The material models developed in this dissertation can predict the process problems and can be used to solve them before the core's production begins.

Kurzbeschreibung

Im letzten Jahrzehnt haben aufgrund von strenger werdenden Umweltbestimmungen anorganisch gebundene Formstoffe ihre organisch gebundenen Pendants in großen Leichtmetallgießereien Schritt für Schritt ersetzt. Anorganische wasserglasbasierte Bindersysteme werden eingesetzt, um aus Sand Gießereikerne und –formen herzustellen. Diese werden vor allem auf Kernschießmaschinen produziert, die dem Formstoffsystem Gestalt geben und es aushärten. Nach der Herstellung werden die Kerne durch Handhabungsprozesse in sogenannte Kernlager verbracht und dort bis zum Abguss gelagert. Nach dem Abguss werden sie mit Hammersystemen aus dem Gussteil entfernt und der zerbrochene Kernsand entweder wiederaufbereitet oder entsorgt. Damit ist der Produktlebenszyklus eines Gießereikerns abgeschlossen.

Entlang dieses Zyklus kann es an verschiedenen Stellen zu Prozessproblemen kommen, die auf die mechanischen Materialeigenschaften des Kerns zurückzuführen sind. So kann der Kern durch Greifer bei der Handhabung verformt werden. Des Weiteren kann es während der gesamten Lagerzeit zu Abweichung durch Kriechen unter dem Eigengewicht der Kerne kommen. Schlussendlich ist der Entkernprozess nach dem Abguss bei anorganischen Formstoffen sehr herausfordernd und muss sehr gut auf die verbleibende Restfestigkeit des Kernes und die Gussteilgeometrie abgestimmt sein.

Für all diese Prozessprobleme bietet sich eine simulative Prozessoptimierung an. Jedoch ist nach dem Stand der Technik das Wissen über die Materialeigenschaften von anorganisch gebundenen Formstoffen so beschränkt, dass diese Simulationen am fehlenden Wissen zum Materialverhalten und der Materialeigenschaften scheitern. An diesem Punkt setzt diese Dissertation an und schafft neue Untersuchungsmethoden, die es ermöglichen, sowohl das allgemeine Materialverhalten von Formstoffen zu bestimmen als auch für konkrete Materialmodelle deren Parameter zu quantifizieren. So wurde ein Prüfstand zur zerstörungsfreien akustischen Analyse der elastischen Eigenschaften von Formstoffen entwickelt, der den Elastizitätsmodul und den Schubmodul bestimmt. Zusätzlich wurden zahlreiche biaxiale Prüfaufbauten für eine Universalprüfmaschine konstruiert, die es ermöglichen Versagenskriterien für Formstoffe zu validieren. Im Besonderen wurde eine Prüfmaschine entwickelt, die unter einstellbaren hydrostatischen Drücken in einer Stickstoffatmosphäre verschiedene Biege- und Druckversuche durchführen kann. So können beliebige Punkte im Hauptspannungsraum angefahren werden und eine Versagensoberfläche bestimmt werden, die mit klassischen Bruchkriterien verglichen wird.

So konnte ein neuartiges Bruchkriterium für Formstoffe geschaffen werden, das die Eigenschaften eines Mohr-Coulomb Kriteriums mit den Eigenschaften eines spröden Materials verbindet. Darin ist die Materialfestigkeit abhängig vom effektiven belasteten Volumen (spröde Eigenschaft) und dem vorliegenden hydrostatischen Druck (Mohr-Coulomb Eigenschaft). Um das Verständnis zum mechanischen Verhalten von anorganischen Formstoffen zu erhöhen, wurde der Einfluss von typischen Einflüssen wie der Bindermenge, der Lagerzeit und der Luftfeuchtigkeit auf die Materialparameter des Materialmodells untersucht. Es konnte gezeigt werden, dass im untersuchten Rahmen die Festigkeit linear mit der Bindermenge steigt, während die Aushärtung nach dem Kernschießen einer logarithmischen Funktion folgt. Steigende Luftfeuchtigkeit senkt die Bruchfestigkeit und die Bruchdehnung signifikant.

Außerdem wurden die Kriecheigenschaften von Formstoffen analysiert, die sich stark auf den Kernverzug während der Lagerung auswirken. Es konnte gezeigt werden, dass die Kriechneigung abhängig vom Verhältnis der anliegenden Spannung zur Materialfestigkeit ist und von Umweltbedingungen, hydrostatischem Druck und der Bindermenge abhängt.

Abschließend wurde anhand eines industriellen Kerns, der in der Serie von der BMW AG eingesetzt wird, der Einsatz der neuen Materialmodelle mit verschiedenen Prozesssimulationen aufgezeigt. Aktuell werden in der Praxis Probleme mit anorganischen Kernen durch Erfahrungswerte und Ausprobieren gelöst. Es konnte gezeigt werden, dass die bei der Inbetriebnahme des Kerns aufgetretenen Probleme mit den in dieser Dissertation erarbeiteten Materialmodellen vorhergesagt und behoben werden können, bevor der Kern in die Produktion geht.

Contents

Prior Publications and Presentations

The following articles and presentations arose during my time as a research associate at the Technical University of Munich. Several parts of this dissertation have been published a priori under my co-authorship in journal papers, conference proceedings and presentations. All relevant prior publications (*) are registered according to the valid doctoral regulations.

Journal papers:

* LECHNER, P.; STAHL, J.; HARTMANN, C.; ETTEMEYER, F.; VOLK, W. (2021). Mohr-Coulomb Characterisation of Inorganically-Bound Core Materials. In: *Journal of Materials Processing Technology*, **296**, 117214

HARTMANN, C.; LECHNER, P.; VOLK, W. (2021). In-situ measurement of higher-order strain derivatives for process analysis using spatio-temporal optical flow methods. In: *CIRP Annals Manufacturing Technology*, **70**, 251-254

ETTEMEYER, F.; SCHWEINEFUSS, M.; LECHNER, P.; STAHL, J.; GRESS, T.; KAINDL, J.; DURACHA, L.; VOLK, W.; GÜNTHER, D. (2021). Characterisation of the decoring behaviour of inorganically bound cast-in sand cores for light metal casting. In: *Journal of Materials Processing Technology*, **296**, 117201

* LECHNER, P.; HARTMANN, C.; ETTEMEYER, F.; VOLK, W. (2021). A Plane Stress Failure Criterion for Inorganically-Bound Core Materials. In: *Materials*, **14(2)**, 247

HARTMANN, C.; WEISS, H.A; LECHNER, P.; VOLK, W.; NEUMAYER, S.; FITSCHEN, J.H.; STEIDL, G. (2021). Measurement of strain, strain rate and crack evolution in shear cutting In: *Journal of Materials Processing Technology*, **288**, 116872

* LECHNER, P.; FUCHS, G.; HARTMANN, C.; STEINLEHNER, F.; ETTEMEYER, F.; VOLK, W. (2020). Acoustical and Optical Determination of Mechanical Properties of Inorganically-Bound Foundry Core Materials. In: *Materials*, **13**, 2531

ETTEMEYER, F.; LECHNER, P.; HOFMANN, T.; ANDRÄ, H.; SCHNEIDER, M.; GRUND, D.; VOLK, W.; GÜNTHER, D. (2020). Digital sand core physics: Predicting physical properties of sand cores by simulations on digital microstructures. In: *International Journal of Solids and Structures*, **188–189**, 155-168

LECHNER, P.; FILIPPOV, P.; KRASCHIENSKI, N.; ETTEMEYER, F.; VOLK, W. (2020). A Novel Method for Measuring Elastic Modulus of Foundry Silicate Binders. In: *International Journal of Metalcasting*, **14**, 423–431

HARTMANN, C.; LECHNER, P.; HIMMEL, B.; KRIEGER, Y.; LUETH, T.C.; VOLK, W. (2019). Compensation for Geometrical Deviations in Additive Manufacturing. In: *Technologies*, **7**, 83

* LECHNER, P.; STAHL, J.; ETTEMEYER, F.; HIMMEL, B.; TANANAU-BLUMENSCHEIN, B.; VOLK, W. (2018). Fracture Statistics for Inorganically-Bound Core Materials. In *Materials*, **11**, 2306.

SCHNEIDER, M.; HOFMANN, T.; ANDRÄ, H.; LECHNER, P.; ETTEMEYER, F.; VOLK, W.; STEEB, H. (2018). Modelling the microstructure and computing effective elastic properties of sand core materials. In: *International Journal of Solids and Structures*, **143**, 1-17

Further publications:

* LECHNER P.; ETTEMEYER F.; VOLK W. (2021). Mechanisches Bruchmodell für wasserglasgebundene Kerne. *Gießerei* (accepted)

* LECHNER P.; VOLK W.; ETTEMEYER F. (2020). Ein mechanisches Bruchmodell für wasserglasgebundene Formstoffe. *3. Formstoffforum*, München

ETTEMEYER, F.; SCHWEINEFUSS, M.; LUSTIG, C.; REINOLD, L. M.; LECHNER, P.; VOLK, W.; GÜNTHER, D. (2020). Charakterisierung des Entkernverhaltens von anorganisch gebundenen Kernen für den Leichtmetallguss. *3. Formstoffforum*, München

ETTEMEYER, F.; SEHRSCHÖN, H.; LECHNER, P.; VOLK, W.; GÜNTHER, D. (2019). Simulation und Optimierung des Entkernprozesses von anorganischen Sand-Binder-Systemen für das Leichtmetallgießen. *Leichtbau in Guss, Nürtingen*

ETTEMEYER F.; STEINLEHNER F.; LECHNER P.; VOLK W.; GÜNTHER D. (2019). Detection of Core Fracture in Inorganically Bound Cast-in Sand Cores by Acoustic Microphony. In: *Advances in Production Research*, WGP 2018

* LECHNER P.; VOLK W.; ETTEMEYER F.; SCHNEIDER, M.; HOFMANN, T.; ANDRÄ, H. (2018). Mikrostrukturbasierte Vorhersage von Materialeigenschaften anorganischer Formstoffe. *2. Formstoffforum*, Aachen

VOLK, W.; BAUMGARTNER, G.; LECHNER, P.; ETTEMEYER, F. (2017). Prognose von Werkstoffeigenschaften mit Hilfe einer Mikrostrukturanalyse im Bereich des Kokillengusses und anorganischer Formstoffe. *Deutscher Gießereitag*

List of Symbols

Symbol	**Unit**	**Meaning**
α	-	Drucker-Prager friction angle
γ	$^\circ$	Shear angle
ϵ	-	Strain
$\dot{\epsilon}$	s^{-1}	Strain rate
θ	-	Lode angle
μ	-	Expectation value
ν	-	Poisson's number
Σ	-	Standard deviation
σ	MPa	Stress
$\boldsymbol{\sigma}$	MPa	Cauchy stress tensor
τ	MPa	Shear stress
ϕ	$^\circ$	Mohr-Coulomb friction angle
A	m^2	Area
B	mm^4	Geometrical moment of inertia
C	MPa	Stress limit
c	MPa	Mohr-Coulomb cohesion
D	mm	Diameter
E	GPa	Young's modulus
F	N	Force
f	Hz	Eigenfrequency
G	GPa	Shear modulus
h	mm	Height
I	MPa	Invariant of Cauchy stress
J	MPa	Deviatoric invariant of Cauchy stress
K	$\mathrm{MPa\,s}^{-1}$	Norton Bailey constant
k	-	Weibull scale parameter
l	mm	Length
m	-	Weibull shape parameter
M	Kg	Mass
n	-	Norton-Bailey exponent
N	-	Sample size

o	-	Creep exponent
P	-	Failure probability
p	$\mathrm{N\,mm^{-2}}$	Pressure
R	mm	Radius
s	-	Probability of survival
t	s	Time
V	$\mathrm{m^3}$	Volume
w	mm	width

Index	**Meaning**
ϕ	Tangential
0	Reference
$1, 2, 3$	Principal directions
$10s$	10 s after tool opening
$120s$	120 s after tool opening
$24h$	24 h after tool opening
$3PB$	Three-point-bending
$4PB$	Four-point-bending
$aniso$	Anistropic
b	Brazilian
b_1	First bending eigenfrequency
c	Compression
DP	Drucker-Prager
eff	Effective
l_1	First longitudinal eigenfrequency
M	Mises
MC	Mohr-Coulomb
max	Maximum
n	Normal
r	Radial
sh	Shear
T	Tresca
t	Tension
t_1	First torsional eigenfrequency
x, y, z	Coordinate directions

xx, yy, zz	Cauchy components
xy, xz, yz	Cauchy components
I, II, III	first, second, third

List of Abbreviations

Abbreviation	**Meaning**
utg	Institute for metal forming and casting
FEM	Finite element method
DIC	Digital image correlation
CAD	Computer aided design
SEM	Scanning electron microscope
RVE	Representive volume element

1 Introduction

Casting is one of the oldest production techniques known. The basic principle has not changed for thousands of years: Material is heated beyond its liquidus temperature and poured into a mould, where the material solidifies into the cast part. During that process, the mould is shaping the geometry of the cast part. The first moulds were lost moulds, which could only be used one time. If the goal is to cast geometries which cannot be generated by the mould alone, lost cores are used to shape internal contours. Today, there are several more casting techniques, but the concept of lost moulds and cores is still relevant and an important part in modern mass production.

While the basic principle of casting has not changed over time, the process has been studied and optimised to achieve a more productive process with products of higher quality. A big step forward was the introduction of numerical simulations of the casting process. Every step in the manufacturing process is duplicated in virtual design and can be optimised based on simulation results (virtual twin). The most important simulations for the casting process after the first draft in Computer Aided Design (CAD) are the mould filling simulation with a subsequent solidification simulation. With such simulations, casting defects like cavities and pores can be avoided.

Based on the solidification rate, the local strength of the material can be predicted and compared with the minimum strength, which is demanded by the mechanical design process. In this design process the geometry of the component is dimensioned based on finite-element method (FEM) calculations for expected load cases over the whole product life cycle. This life cycle starts with the cast part in the mould and ends with the recycling of the component. These calculations help to ensure that the component can fulfil its objectives, without excessive material usage. This has economical and ecological benefits, since producing optimised components saves material and energy.

In short, various simulations form a digital twin for cast components, which provides data for both sides of the dimensioning process: The expected requirements and the expected performance of the future component. For foundry cores on the other hand, this digital twin is still incomplete. Today, the material requirements for the cores are not derived directly from load cases, but from experience and empirical knowledge. This leads to inefficient core designs which use unnecessary amounts of resources to safely achieve the objectives of the cores.

The required strength of a foundry core defines the minimal amount of the chemical binder needed. This is mainly influenced by two factors: The necessary handling strength until the core is placed in the mould and the desired hot strength of the core during casting.

In this dissertation, the main objective is to find and validate a material model for chemically-bound foundry sands. This will help to complete the digital twin for foundry cores and enable FEM simulations to optimise the cores and their related processes and thus saving material and energy.

2 State of the Art and Theoretical Foundations

In this chapter, I will introduce the state of the art and the theoretical foundations for this work. There are four sections: Foundry Core Life-Cycle, Microscale Modelling, Macroscale Modelling and Mechanical Testing Methods. These sections detail the theoretical basis, which builds the starting point for this work.

2.1 Foundry Core Life-Cycle

In general, cores made of foundry sand or ceramics can only be used for a single casting, as they are destroyed to remove the product from the mould (Campbell, 2015, p. 89). Cores are used to form contours, which cannot be realised by the mould alone due to undercuts (Bührig-Polaczek and Träger, 2010). The basic concept in manufacturing of such lost moulds or cores is that a base material, usually consisting of sand, whose grains have little cohesion, is solidified by adding further components, which act as a binder agent (Hans-Jürgen Warnecke, 1993). If the base material is magnetic, the hardening can be achieved with electro-magnetic forces and without a binding agent (Sahade et al., 2016). However, this is a rare exception. In most cases a binding agent is utilised to solidify the individual grains. Figure 2.1 shows an overview of the foundry core life cycle from the individual constituents to the disposal or regeneration after the casting. The structure of this section follows this life-cycle.

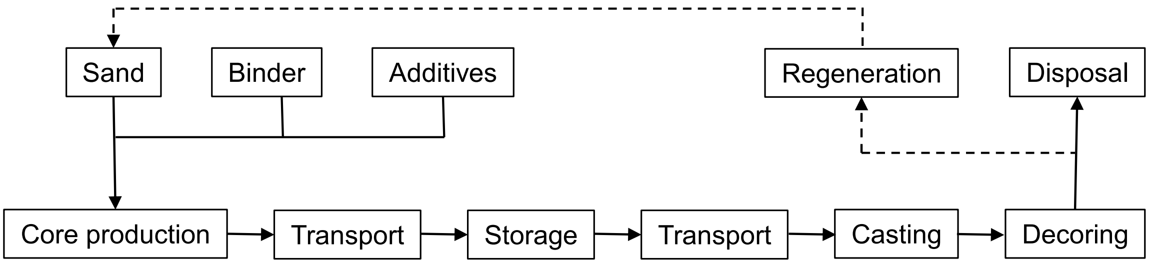

Figure 2.1: Overview of the foundry core life cycle. (after Ettemeyer et al., 2021 and Sobczyk, 2008, p. 8)

2.1.1 Foundry Sand

Kogel defines foundry sands as a material composed of granular particles of mineral matter (Kogel, 2006, p.1433). According to Pasternak, foundry sands and their properties have to be adjusted to their respective use case. Important properties for loose sand are

- gas permeability,
- plasticity (ability to copy the pattern),
- heat resistance.

Gas permeability describes the ability of foundry sand to allow the gases, which are generated during the casting process, to escape quickly. Insufficient permeability of the sand leads to gas bubbles in the casting (DeGarmo et al., 2008, p. 289). Thus, this is one of the advantages of sand moulds compared to steel moulds, which have no permeability. Mainly, the gas permeability depends on the porosity of the sand. Grains of the same size and spherical shape result in good gas permeability, with coarse-grained sand being more gas-permeable than fine-grained sand. Large and small grains together result in poor gas permeability, as the small grains clog the spaces between the large sand grains. (Pasternak, 1989, p. 33)[1]

Plasticity describes the ability of the foundry sand to copy the model. It must not be destroyed under process-specific mechanical compression and must not form cracks. The plasticity depends on the number, size, shape and contact surfaces of the sand grains, as well as the properties of the binder. Fine-grained sand has better plastic properties than coarse-grained sand. (Pasternak, 1989, p. 33)

Heat resistance of the sand describes the behaviour of the sand grains for high temperatures. Silica sand has several possible phase-changes in the interval from room-temperature to casting temperatures, with the transition from low quartz to high quartz at 573 °C as the most notable (Pabst and Gregorova, 2013). Furthermore, the sintering-temperature of the specific sand has to be higher than the casting temperature (Rao, 2003, p. 18).

---

[1] Citation note: A reference is quoted behind a word or a group of words, when relating exclusively to them. The punctuation is located behind the reference in this case. A reference refers to a paragraph, when being placed behind the punctuation.

2.1.2 Binder

Fundamentally, we differentiate chemical and physical bonding mechanisms in foundry cores. These bonding mechanisms hold the individual grains together and lead to the material cohesion. Figure 2.2 shows an overview of the most important binder systems. The physical binder systems are closely related to the relevant mechanical mechanisms in soils: In the absence of chemical bonding, the main contributors to the material strength are the frictional forces between the grains and the kinematic constraints between the particles (Mitchell and Soga, 2005, p. 370). The frictional forces heavily depend on the size, form and surface of the grains (Kieslinger, 1962). Soils are classified as cohesive soils if the portion of fines exceeds 50 % (Gautam, 2018). The main contributions to this cohesion are cementation, electrostatic as well as electromagnetic attraction, primary valence bonding and adhesion (Gautam, 2018). Analogously, there are several physical binder systems, which are utilised to shape foundry sands into moulds and cores and harden them enough to withstand the thermal and mechanical stresses of the casting process. The most frequent mechanical mechanism is based on clay-bonded foundry sands (green sand). The clay component is mainly a bentonite (Abichou et al., 2000). Green sand moulds are based on the constituents bentonite, a lustrous-carbon former and sand (Waters, 1996, p. 18). They are hardened by compaction.

On the other hand, there are two types of chemical binders: organic and inorganic binders. Organic binders are mostly resins, with furan, phenol and urethane being the most important representatives. (Beeley, 2001, p. 209)

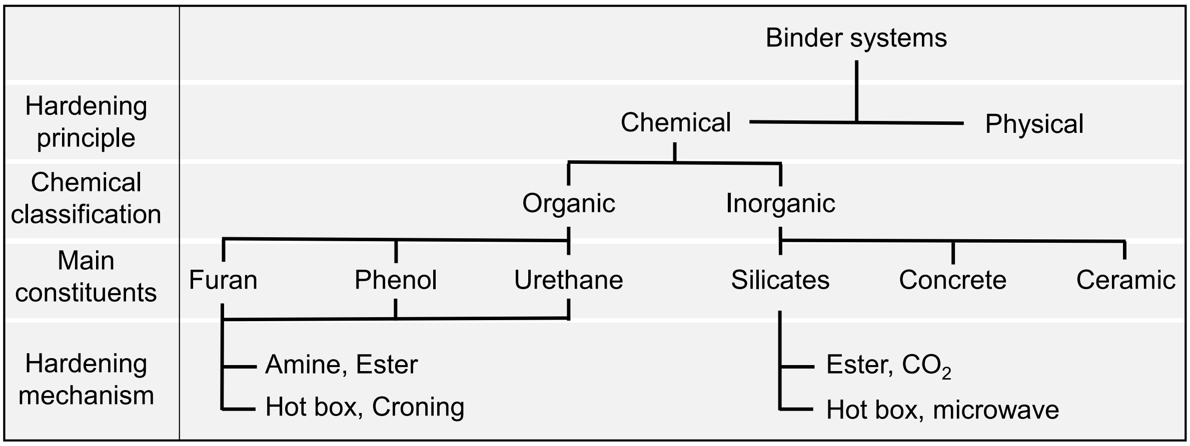

Figure 2.2: Overview of binder systems for core materials, categorised by hardening principle, chemical classification, main constituents and hardening mechanisms.

The most important inorganic chemical binder systems are silicates, cements and ceramics (Czerwinski et al., 2015). Silicate binder systems can be categorised into chemical hardening and thermal hardening binder systems (Liu et al., 2014). Sodium silicate, which is also called water-glass, can be hardened chemically with ester or CO_2 or it can be hardened with thermal activation. The most important process is the hot gassing of water-glass. The Inotec and the Cordis process are commercially available binder systems, which are based on sodium silicate. Concrete-based binders and the ceramic process of investment casting are not relevant for this dissertation, which focuses on foundry sand, bound by a chemical binder agent.

Chemical Fundamentals of Organic Binder Systems Concerning organic binders, a distinction is made between heat hardening and cold setting binder systems (Strauss, 2014, p. 321). The heat hardening process is utilised in the hot/warm box or shell processes (Campbell, 2015, p. 811). The hot box process uses liquid phenolic or furan resins, mixed with an acid catalyst. The exothermic hardening takes up to 120 s at 180 - 340 °C. The warm box process is very similar with the exception of a process temperature under 180 °C. The shell process utilises sand precoated with a resin. The precoated sand is pressed to a heated pattern tool, which starts the reaction hardening the binder system. This reaction stops at a depth of 4 - 10 mm resulting in a sand shell. Subsequently, the remaining loose precoated sand can be reused. (Bührig-Polaczek and Träger, 2010)

Cold setting binder systems are mainly represented by the No-Bake and the gas-hardening processes. The most important No-Bake processes utilise furan, ester hardened phenolic resins or phenolic urethane binders. The sand is mixed with the liquid binder and an additional catalyst. The reaction and setting time is mainly controlled by the relative amount of catalyst and the sand temperature. (Beeley, 2001, p. 209)

The main representatives of the gas hardening processes are the phenolic urethane and the ester cured phenolic cold box systems. Both systems use a gas as a reaction catalyst. Phenolic urethane is hardened with tertiary amine. Both gas-hardening systems are used for rapid volume production of cores due to the short process cycle time. (Beeley, 2001, p. 213)

Chemical Fundamentals of Water-Glass Binder Systems The constituents of water-glass production are silica sand (Si_2O) and sodium carbonate (Na_2CO_3). The production process has three steps. First, the two components are fused at 1300 - 1500 °C. The liquid melt is quickly cooled down and solidifies to amorphous glass. This amorphous glass is dissolved in water at 140-180 °C and a pressure of 4-9 bar. The gained solution is called sodium silicate or water-glass. Sodium silicate is characterised by its modulus. The modulus can be calculated as the ratio of SiO_2 and Na_2O. Typically, the modulus ranges between 2.0 and 3.3. The modulus correlates with the tensile strength of the hardened binder and the subsequent cores. Furthermore, the water-glass is characterised by the concentration of the Si_2O-NaO_2 particles in the water. The viscosity of the solution is determined by this concentration. (Polzin, 2014, p. 15-18)

There are two different hardening mechanisms for water-glass, thermal and chemical hardening. Independently of the hardening mechanism, the water-glass solidifies in a polymerisation reaction. Figure 2.3 shows the chemical reactions which solidify the binder system in a thermal hardening process. After an activation step, a condensation reaction follows, which builds a bigger water-glass molecule from the original two silanol molecules (Si-ONa). By repeating this process, the molecule grows by adding more silanol molecules with silox bonds (Si-O-Si) to the already existing molecules. (Wallenhorst, C., 2010)

Figure 2.4 shows the polymerisation of silicate clusters from monomers to cyclics and particles (1 nm). From the particle status, the further reaction is dependent on the pH value of the surrounding medium. If the pH value is between 7 and 10 and if there are no salts, the particles grow further to a sol particle, while with a pH value under 7 or with salts present, more particles are built in a gel network (Iler, 1979, p.174).

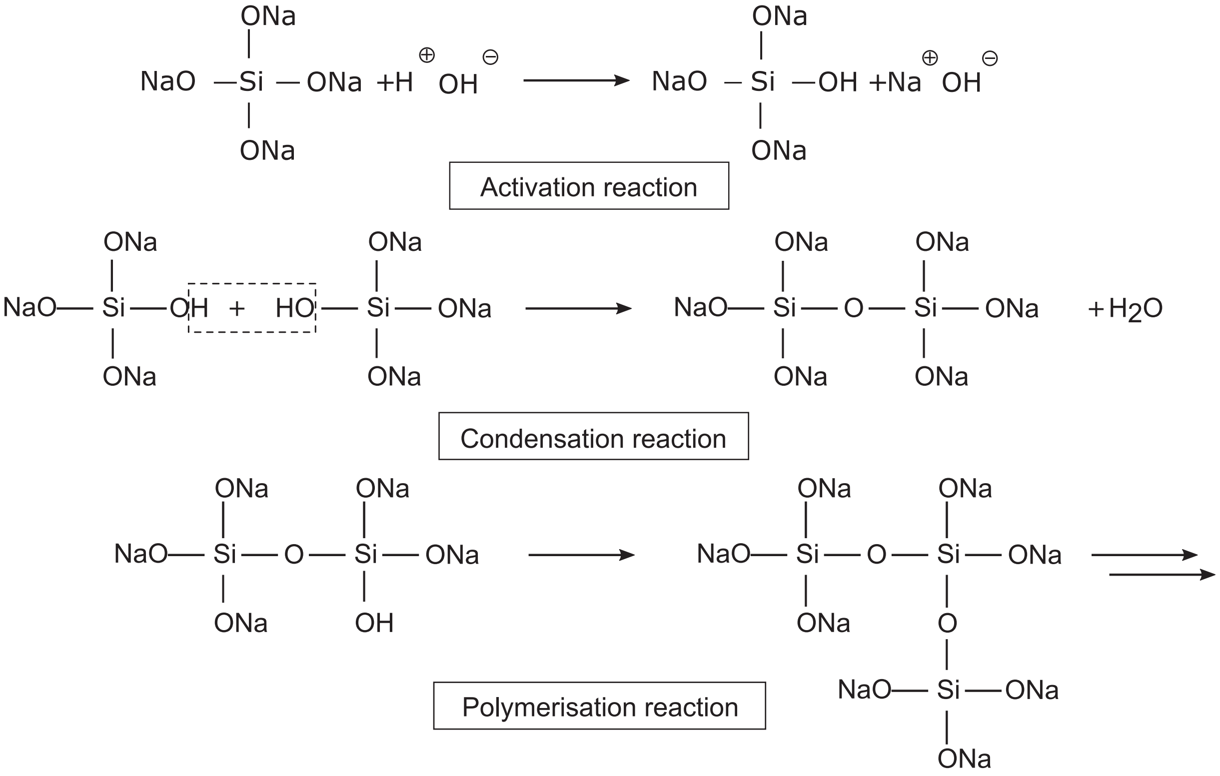

Figure 2.3: Chemical reactions of water-glass. The condensation and the polymerisation reaction are reversible. (Wallenhorst, C., 2010)

These gel-networks build the binder bridges between the individual sand grains (Polzin, 2014, p.20). In both cases the reaction is a condensation reaction under separation of water. In case of chemical hardening, this process is induced with inorganic or organic additives. The most important organic hardener is ester, while aluminium-phosphate is the most important inorganic one (Masoudi Alavi, 2019, p. 8). Furthermore, sodium silicate can be hardened with CO_2, which leads to a significantly lower core strength than the thermal hardening, because of the existence of sodium carbonate in the binder bridges, which builds needle-shaped structures and therefore reduces the strength of the bridges (Polzin, 2014, p.56).

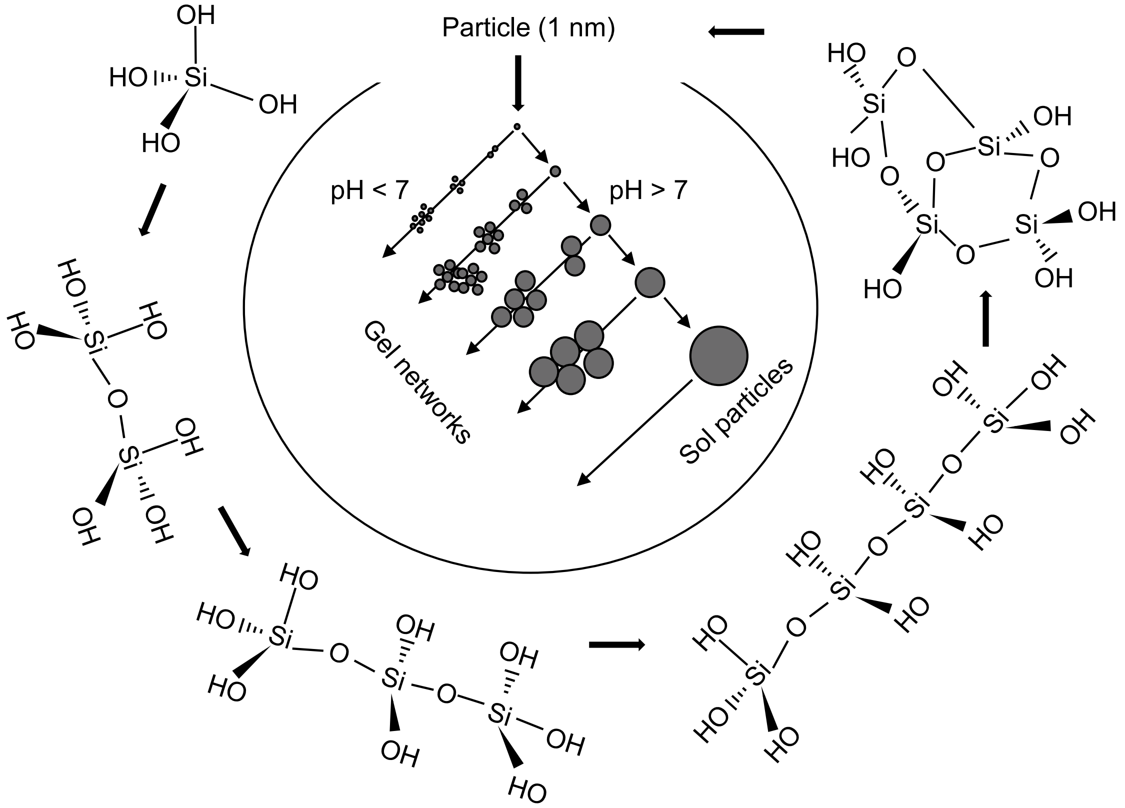

Figure 2.4: Polymerisation of silicates after Iler and McIntosh. The reaction starts at monomers and leads through further polymerisation to particles of the size 1 nm. Depending on the pH value in the surrounding medium the further reaction leads to sol particles or a gel network. (after Iler, 1979, p. 174; McIntosh, 2013)

2.1.3 Production

Pasternak differentiates four different core production processes by the method of filling the core box and compacting the sand (Pasternak, 1989, p. 142-145): core pressing, core tamping, core blowing and core shooting. In core pressing, a predetermined amount of sand-binder mixture is pressed into a die. Core tamping uses a screw to carry the sand into the tool and to compact it. Core blowing uses a continuous stream of pressurised air to fluidise the sand-binder mixture and to carry it into the tool. In contrast, core shooting uses a short burst of pressurised air to fill the tool and to compact it (Winartomo et al., 2005). Today, core shooting is the main production technique for cores, while the core blowing technique is not used any more due to the high amount of pressurised air necessary (Ni et al., 2016). This led to a change in the terminology. The term core blowing is now often used for the original core shooting, as well (Beeley, 2001, p. 477). Figure 2.5 shows a scheme of a core blowing (left) and a core shooting (right) machine.

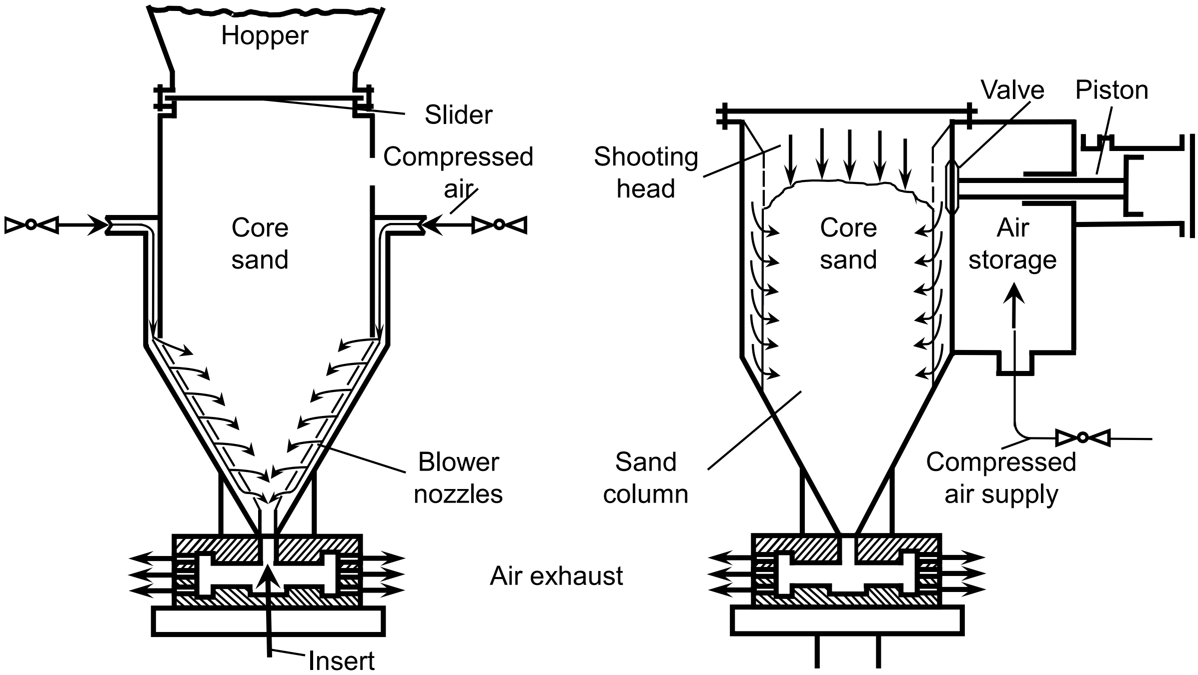

Figure 2.5: Core production principles. Scheme of the core blowing principle (left) and core shooting principle (right). The pressurised air is flowing continuously through the sand in the core blowing process. In the core shooting process, the pressurised air is controlled by the valve and released in form of a shot, which carries the sand into the core box (after Pasternak, 1989, p. 144).

In the core shooting process, a sand-binder mixture is prepared and stored in the shooting cylinder. This shooting cylinder is connected through a controllable valve to a tank with pressurised air. Furthermore, there are shooting nozzles connected to the shooting cylinder. To fill the core box with sand, the valve is opened for a short period of time, which carries the sand through the shooting nozzles into the core box. Because of the high kinetic energy of the sand grains, they are pressed against the tool surface and the sand binder mixture is compacted in the core box, while air excess air escapes through vents. (Pasternak, 1989, p. 144)

During the last two decades, the additive manufacturing of cores has been developed. There are two main additive production techniques to manufacture cores and moulds. Firstly, there is the laser-melting of resin-coated sand. The sand grains are precoated with a resin-based binder system, which is activated with the thermal energy of a laser (Dini et al., 1999). This is a classical laser-powder-bed technique.

The second is the binder jetting of sand cores. It is a powder-bed process as well, but the sand grains are bound by a binder, which is added into the sand bed by a binder-jetting module. Binder-jetting has several advantages over the laser-based processes. The manufacturing speed scales with the amount of printing modules, which are less expensive than laser systems. Furthermore, it is more flexible regarding the binder system. There are processes for both organic and inorganic binder systems, while the laser-based process only is suitable for organic binder systems. (Ramakrishnan et al., 2014)

Both processes build up the cores layer by layer, which results in a typical anisotropy of the material properties. In the direction of the build-up, the material properties typically differ from the other two directions (Ramakrishnan, 2016, p. 86). This dissertation will focus on the fundamental determination of the material properties of cores manufactured on a core blowing machine. Those cores are assumed isotropic. However, the methods described in the following chapters could be applied to additively manufactured cores in the future, as well.

2.1.4 Handling

Lotter and Wiendahl structure handling devices into devices for storing, changing quantity, moving, holding and inspecting (Lotter and Wiendahl, 2006). All of those handling processes are relevant for foundry cores, as well. Cores can be handled manually, partially automated or fully automated.

There is little research on the topic of core and mould handling, yet. Most of it describes storage systems and the algorithms how to decide which core or mould is transported to casting. Lee describes a storage system, which copes with typical core problems like low immediate strength, an upper storage time limit and the need for manual rework (Lee, 1983).

While there is little research on core handling, a multitude of patents have been granted for automated core and mould handling machines. Landua and Müller describe the high cycle time and low precision of manual core assembly and propose a machine for automated core handling (Landua and Müller, 1988). Common describes an invention for automated handling of large sized cores (Common, 1940). These are only two examples of the high number of patents in this area, which shows the industrial relevance and an obvious research gap.

In this dissertation the focus will lie on automated handling, since the deterministic movements of an automated handling system are the foundation for the application of a mechanical simulation.

Figure 2.6 shows a typical example of core handling with a robot. The core is clamped by the gripper on the short sides, which leads to bending moments in the core because of its weight and the acceleration of the robot.

Figure 2.6: Core handling robot with specialised gripper (Muschna, 2020). In modern core production, cores often are handled with robots. Depending on the gripper and the geometry and the weight of the core, the stresses in the core are significant.

2.1.5 Casting

According to the standard DIN 8580, casting belongs to the main group of shaping (DIN 8580, 2003). Typical metal casting processes belong to the subgroup "shaping from the liquid state" and can be subdivided into processes with non-permanent (lost) moulds and permanent moulds. Lost moulds are made of foundry sand or ceramics, while permanent moulds are mostly made of steel (Bührig-Polaczek and Träger, 2010). Lost moulds can be produced with permanent or lost patterns. Permanent patterns are removed from the mould after the sand is hardened, which makes a partition of the mould necessary. Lost patterns stay in the mould and are combusted during the casting. (Pasternak, 1989, p. 26)

Figure 2.7 shows an overview of casting methods. Relevant for this dissertation are casting methods, which use chemically-bound foundry sands either for the mould or for cores. This can apply to non-permanent sand moulds (hand or machine) and the core package mould, which is an assembly of sand cores. Foundry cores can be used in gravity, low-pressure, tilt and centrifugal die casting. In pressure die and squeeze casting, sand cores are not in use yet, due to the pressure induced stresses on the cores (Schwickal, 2015).

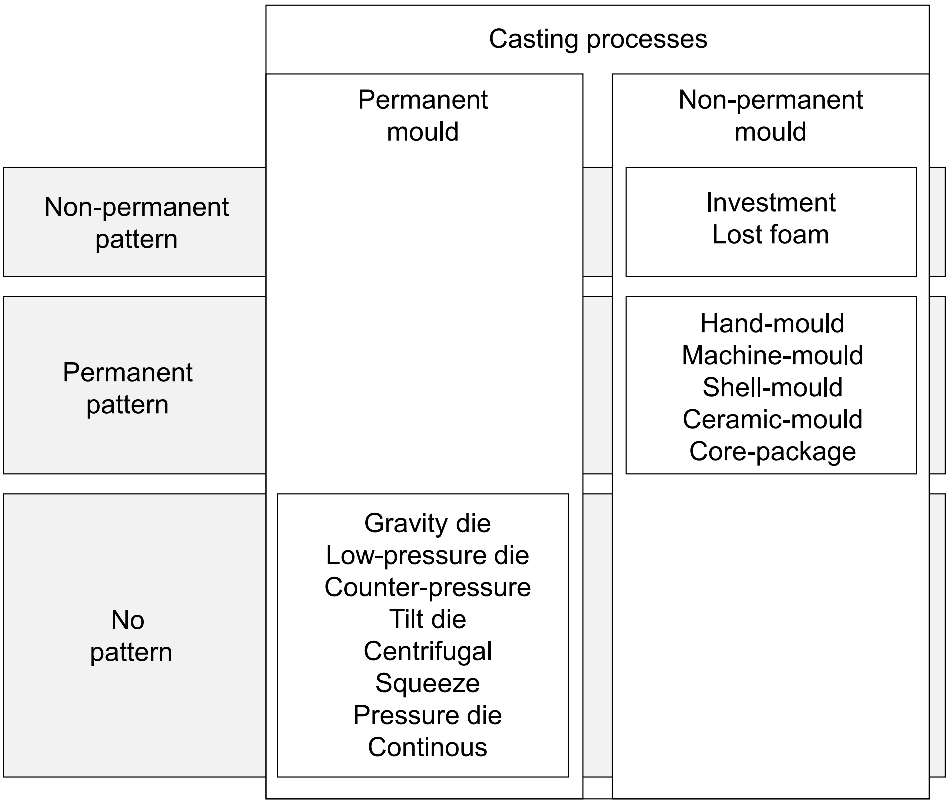

Figure 2.7: Overview of the most important casting methods, categorised by the type of patterns and the type of mould (Bührig-Polaczek and Träger, 2010; Grote, 2007).

2.1.6 Decoring

At the end of the core's product life cycle stands the decoring process. After the casting, the cores still remain in the cast part. The heat of the casting process has weakened the cores, which have to be destroyed in order to remove them from the cast part (Conev et al., 2017). According to Gamisch the decoring can be achieved thermally, by hammers, by mechanical oscillating or with electric shock-waves. The thermal deactivation of the binder is very energy intensive, even if the process is simultaneously used as a heat treatment for the cast part. Decoring by pneumatic hammers is widely used. The cast part has to be manipulated in different poses to effectively remove the core sand, either manually or by an automatic system. Typically, the mechanical oscillating needs cores with pre-induced fractures to work, which is achieved with a short hammering interval. Decoring with shock-waves uses water as a medium which transmits the shock wave of an electrical discharge (Konzack, 2013). This has the disadvantage that the sand has to be dried in the subsequent recycling process. (Gamisch, 2002)

One disadvantage of inorganically-bound cores is that the binder has more residual strength after the casting than the organic pendants, because of the inorganic chemical structure which does not combust during the casting. However, the heat of the casting is weakening the binder bridges. There have been several studies, which material and process conditions help the decoring process of inorganically-bound core materials. Stauder et al. showed that the de-agglomeration rate during decoring is increasing with increasing thermal load (Stauder et al., 2018a). Major-Gabryś and Dobosz claim that additives, which decrease the thermal expansion of cores during casting also reduce the decoring effort, since the thermal expansion of the cores lead to internal stresses (Major-Gabryś and Dobosz, 2007).

The decoring concludes the life-cycle of the core. In the next sections, I will introduce the mechanical and experimental fundamentals, which are necessary to determine all relevant material properties of core materials.

2.2 Microscale Modelling

Core materials which consist of a granular sand and a binding agent are an open porous medium. The binder forms bridges between the sand grains and builds a complex microstructure, which has to be considered for all mechanical calculations. (Ettemeyer et al., 2019)

2.2.1 Micromechanics of Core Materials

Schneider et al. modelled this microstructure for a sand-binder system consisting of a H32 silica sand and an inorganic sodium silicate binder (Schneider et al., 2018). They extracted the geometry of typical grains from computer-tomography data and arranged them with an artificial packing algorithm according to the density of the real material. The contact interfaces between the grains are modelled with binder bridges. They performed elastic FEM stress calculations on this micro-structure and studied the influence of the grain shape, the binder amount and the physical properties of the silica sand and the binder bridges. Figure 2.8 shows an example of such a calculation. The cube is extended uni-axially in x-direction. The stress is localising in the binder bridges. Ettemeyer at al. adapted this model from purely elastic to fracture calculations by introducing a damage model in the material description of the binder bridges (Ettemeyer et al., 2019). This microstructural simulation is based on the mechanical behaviour of the individual constituents of the porous structure: the sand and the hardened binder. Therefore, the physical properties of these constituents have to be known for an accurate calculation of the mechanical behaviour of the compound. In a previous article, it was shown that the elastic properties of hardened binder can be quantified with a nanoindenter (Lechner et al., 2019).

However, the computational effort for this complex structure is significant. This problem is common for microstructural simulations. Therefore, these models are utilised to predict the material properties of the compound on a small scale, while simulations on a larger scale are performed with macroscopic simulations which are parameterised based on the effective material

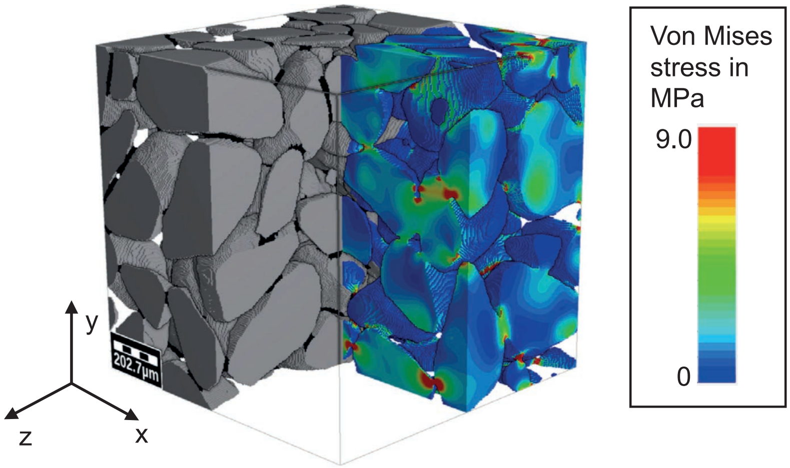

Figure 2.8: Microstructure and von Mises stress field of core materials for 0.5 % extension in x-direction (Schneider et al., 2018).

parameters from the microstructure simulations. This method is called multi-scale hierarchical modelling. (Quayum et al., 2015)

2.2.2 Multi-Scale Modelling

The small volume which is utilised in the microstructural calculation is called the representative volume element (RVE). Its size has to be chosen such, that the computational effort is tolerable. Furthermore, the RVE has to be big enough to contain sufficient micro-structural information for a representative estimation of the macroscopic effective properties of the compound of sand grains and binder bridges. (Quayum et al., 2015)

Schneider et al. determined that a RVE of 64 grains is sufficient to calculate the effective elastic parameters of inorganically-bound core materials. This coincides with a cubic edge length of 1.28 mm with the average grain size utilised in this article. The effective properties which can be calculated with this RVE are in turn validated with macroscopic experiments on the sand-binder compound. (Schneider et al., 2018)

Therefore, one has to differentiate the physical properties and stress states on the microstructural level and the effective properties and stresses of the macroscopic level which are calculated with an RVE. The article showed that it is possible to calculate effective macroscopic elastic properties from the microstructure and to validate them with macroscopic experiments.

Luding et al. showed that the contact stresses between the individual spheres in unbound granular media are proportional to the macroscopic effective shear stresses in the medium (Luding et al., 2001). Analogously, this holds true for core materials. The stresses on the microstructural level and the macroscopic stresses which are induced on the RVE are directly proportional for small deformations and load-independent physical properties of the constituents.

However, the absolute stress values differ. It is possible that the stress in some binder bridges exceeds the macroscopic stress as long as the stress does not exceed the strength of binder bridges themselves. Thus, the effective macroscopic fracture strength depends on the microscopic fracture strength. Ettemeyer et al. calculated the effective macroscopic fracture strength for core materials based on their microstructure (Ettemeyer et al., 2019).

2.3 Macroscale Modelling

The section before showed that the microstructure of materials can be represented by a mechanic continuum with effective physical properties. This abstract description models the average mechanical behaviour sufficiently to perform mechanical calculations. However, the local mechanical properties and the exact microstructure are deviating from their average, which is represented by the macroscale material parameters. Therefore, fracture always follows a probability distribution. Stochastic errors in the test setup and defects in the material itself always lead to scatter when repeating experiments (Weißbach, 2004, p. 233). The physical properties of the material determine, which statistical distribution describes this scatter best.

2.3.1 Fracture Statistics

The most important statistical distribution is the Gauss or normal distribution (Rooch, 2014, p. 60). Its probability density function follows (Bauer, 1991):

$$f(x) = \frac{1}{\sqrt{2\pi\Sigma^2}} e^{-\frac{(x-\mu)^2}{2\Sigma^2}}, \tag{2.1}$$

where μ is the mathematical expectation and Σ^2 is the variance. Most material failure is normal-distributed. A notable exception are lifetime failures (Weibull, 1951) and brittle materials, which show no plastic flow and follow the weakest link theory. The failure probability P of a brittle fracture with arbitrary stresses σ can be calculated as (Weibull, 1939, p.8):

$$P = \int_V \nu(\sigma) dV, \tag{2.2}$$

where $\nu(\sigma)$ is the material function, which expresses the strength properties of the material. For isotropic materials, $\nu(\sigma)$ is independent of the position of the volume element dV as well as the direction of the stress σ. Weibull fitted $\nu(\sigma)$ to experimental data and derived:

$$\nu(\sigma) = k \left(\frac{\sigma}{\sigma_0}\right)^m, \tag{2.3}$$

where k, σ_0 and m are constants. This leads to the probability of rupture for the Volume V

$$P = 1 - e^{-V\left(\frac{\sigma}{\sigma_0}\right)^m}, \tag{2.4}$$

where σ is the uniform stress applied to the specimen, σ_0 is the scale and m is the shape parameter of the Weibull distribution.

The weakest link theory implies, that the most critical defect in the specimen leads to failure. It also implies that for a given defect density it is more probable to find a critical defect in a bigger specimen than in a smaller specimen. This means that bigger specimens have a lower fracture stress than smaller specimens, which is in contrast to materials which fracture in a normal distributed manner, like metals. Analogously, it can be argued that the stress concentrations in the microstructure in figure 2.8, which depend on the size, the shape and the orientation of the grains and binder bridges (Schneider et al., 2018), are randomly distributed and that a bigger volume is more likely to contain a critical stress concentration than a small one. This would lead to a size effect as well, which will be discussed in section 6.1.

In order to compare different geometries and stress states in components, there has to be a volume correction to compare them at the same effective volume. For non constant uni-axial stress fields the effective volume can be calculated as (Gong, 2003):

$$V_{eff} = \int_V \left(\frac{\sigma}{\sigma_{max}} \right)^m dV, \tag{2.5}$$

where σ is the local stress in the integrated volume cell and σ_{max} is the maximum stress in the specimen. Weibull extended his theory to bi-axial stress states and concludes that the probability of rupture for a specimen loaded with principal stresses σ_1 and σ_2 follows (Weibull, 1939):

$$P = 2k \int_0^{\pi/2} \int_{-\psi_0}^{\psi_0} \cos^{2m+1} \Phi (\sigma_1 \cos^2 \psi + \sigma_2 \sin^2 \psi)^m d\Phi d\psi, \tag{2.6}$$

where Φ and ψ are elevation and azimuth angles in the spherical coordinate system. Barnett et al. proposed an approximation for multi-axial stress states by treating each principal stress independently and adding up the their failure probabilities (Barnett et al., 1967):

$$P = 1 - \exp \left[- \int_V \left(\frac{\sigma_1}{\sigma_0} \right)^m + \left(\frac{\sigma_2}{\sigma_0} \right)^m + \left(\frac{\sigma_3}{\sigma_0} \right)^m dV \right]. \tag{2.7}$$

This equation is called the Barnett-Freudenthal approximation. The idea of treating the fracture probabilities of each principal stress independently is called the principle of independent action (Lamon, 1988). Equation 2.7 describes the fracture probability, which depends on the three principal stresses. Therefore, it describes fracture in a three-dimensional space, called principal stress space. Weibull calculated the probability for rupture by comparing the principal stresses to a scale parameter σ_0. This implies that fracture occurs once the stress state exceeds a certain threshold. In the next section, I will show how this threshold can be calculated based on the stress state of the specimen in question.

2.3.2 Yield Criteria

Yield criteria describe the failure surface of materials on a macroscopic scale. They model the transition from elastic to plastic strains, based on the stress state. This transition coincides with fracture for ideal brittle materials (Leckie and Bello, 2009). For porous materials this is a simplification, since the continuous stress state in the specimen neglects the geometry of the microstructure and is therefore an "effective" stress, which is directly proportional to the microstructural stresses, but not identical, as described in section 2.2.2.

This section will describe yield criteria with increasing complexity, which are relevant for engineering materials in general and for porous and brittle materials specifically. The stress state is described by the Cartesian Cauchy stress tensor:

$$\boldsymbol{\sigma} = \begin{pmatrix} \sigma_{xx} & \tau_{xy} & \tau_{xz} \\ \tau_{yx} & \sigma_{yy} & \tau_{yz} \\ \tau_{zx} & \tau_{zy} & \sigma_{zz} \end{pmatrix}, \tag{2.8}$$

where the tensor entries are the stresses in the respective coordinate direction. The eigenvalues of the Cauchy stress tensor are the principal stresses σ_{1-3}. With a matrix diagonalisation, the Cauchy stress tensor reduces to (Har and Kumar, 2012):

$$\boldsymbol{\sigma} = \begin{pmatrix} \sigma_1 & 0 & 0 \\ 0 & \sigma_2 & 0 \\ 0 & 0 & \sigma_2 \end{pmatrix}. \tag{2.9}$$

Yield criteria are often described in terms of stress invariants. They describe the Cauchy stress tensor independently of the coordinate system. In principal stress space the stress invariants are (Hearn, 1997, p. 244):

$$I_I = \sigma_1 + \sigma_2 + \sigma_3, \tag{2.10}$$

$$I_{II} = -\sigma_1\sigma_2 - \sigma_2\sigma_3 - \sigma_3\sigma_1, \tag{2.11}$$

$$I_{III} = \sigma_1\sigma_2\sigma_3. \tag{2.12}$$

Furthermore, there are deviatoric (reduced) stress invariants, which describe the stress tensor minus the hydrostatic pressure $\sigma - I_1/3$. In the following they will be utilised for mechanical effects which are unaffected by the hydrostatic pressure in the stress tensor. The deviatoric stress invariants are calculated as follows (Hearn, 1997, p. 246):

$$J_I = 0, \tag{2.13}$$

$$J_{II} = \frac{1}{3}\left(I_I^2 + 3I_{II}\right), \tag{2.14}$$

$$J_{III} = \frac{1}{27}\left(2I_I^3 + 9I_1 I_{II} + 27I_{III}\right). \tag{2.15}$$

Von Mises The von Mises yield criterion states that plastic deformation starts when the second deviatoric stress invariant of the stress tensor reaches a specific limit (Mises, 1913). It is also called maximum distortion energy criterion, which explains the physical reasoning behind it. The work necessary for the distortion in the material is calculated with the second deviatoric invariant and compared with an upper limit. The von Mises yield surface is calculated as follows (Gross and Seelig, 2011, p. 25):

$$\sqrt{J_{II}} - C_M = \sqrt{\frac{1}{6}[(\sigma_1 - \sigma_2)^2 + (\sigma_2 - \sigma_3)^2 + (\sigma_3 - \sigma_1)^2]} - C_M = 0, \tag{2.16}$$

where J_{II} is the second deviatoric stress invariant and σ_{1-3} are the three principal stresses. C_M is the yield limit. The Mises yield surface in principal stress space is a cylinder along the hydrostatic axis ($\sigma_1 = \sigma_2 = \sigma_3$), as shown in figure 2.9a.

Tresca The Tresca yield criterion, which is also known as maximum shear stress hypothesis, suggests that material yields if the maximum shear stress exceeds a specific limit C_T. This leads to a yield surface in shape of a hexagonal prism along the hydrostatic axis, as shown in figure 2.9b, which is defined by the following equation (Gross and Seelig, 2011, p. 25):

$$\max(|\sigma_1 - \sigma_2|; |\sigma_2 - \sigma_3|; |\sigma_3 - \sigma_1|) - C_T = 0. \tag{2.17}$$

Rankine The principal stress (Rankine) yield criterion, describes a fracture induced by the maximum principal stress in the material. If one of the principal stresses exceeds the tensile or compressive strength, the material yields. Both minor principal stresses are neglected for this calculation. This leads to a cubic yield surface in principal stress space. Figure 2.9c shows the yield criterion.

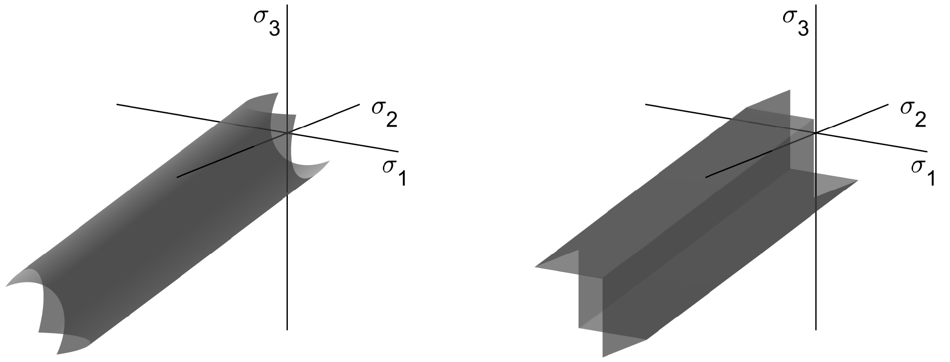

a) Mises b) Tresca

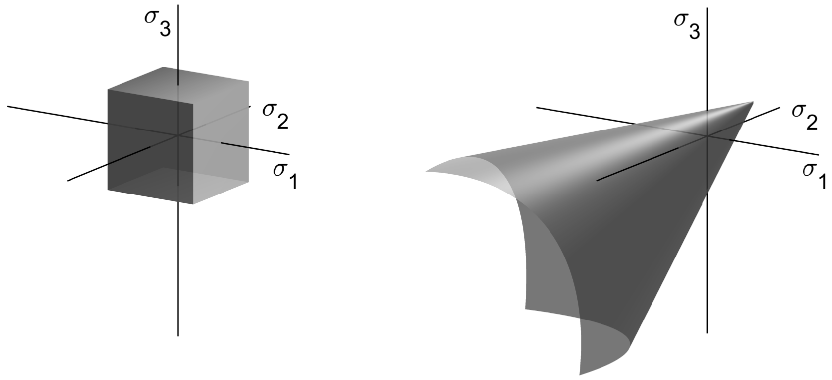

c) Rankine d) Drucker-Prager

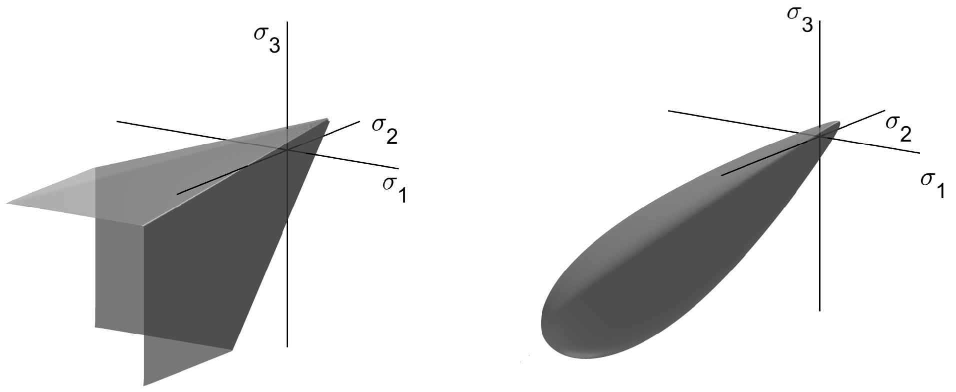

e) Mohr-Coulomb f) Ehlers

Figure 2.9: Yield criteria in principal stress space. The von Mises (a) and Tresca (b) are one parameter models. Rankine (c), Drucker-Prager (d) and Mohr Coulomb (e) are two parameter models. The Ehlers criterion (f) is defined with seven parameters.

Equation 2.18 describes the surface of this yield criterion in principal stresses, where σ_t and σ_c are the tensile and compressive strength, respectively (Gross and Seeliger, 2016, p. 47).

$$\sigma_i = \begin{cases} \sigma_t, & \sigma_i \geq 0 \\ \sigma_c, & \sigma_i < 0 \end{cases} . \tag{2.18}$$

The principal stress hypothesis is mainly applied to brittle materials like ceramics (Gross and Seeliger, 2016). For ceramics, compressive stresses usually are neglected, since the compressive strength is more than five times higher than the tensile strength (Danzer, 1992). Dong et al. use the principal stress criterion to model fracture of shell moulds (Dong et al., 2010).

Drucker-Prager The Drucker-Prager yield criterion is mainly used for problems of soil mechanics. In three-dimensional principal stress space, it's yield surface has the shape of a cylindrical cone along the hydrostatic axis. The following equation describes the Drucker-Prager yield surface, which is shown in figure 2.9d (Drucker and Prager, 1952):

$$\alpha I_I + J_{II}^{1/2} - C_{DP} = 0, \tag{2.19}$$

where I_I and J_{II} are the first and second invariants of the Cauchy stress tensor and the deviatoric stress tensor, respectively. α and C_{DP} are the parameters describing the shape of the cone. This dependence on the first stress invariant is called "pressure sensitivity" and is typical for frictional materials (soil, concrete, rock, granular media and others) (Bigoni and Piccolroaz, 2004). Similar to the von Mises criterion, material failure depends also on the second deviatoric stress invariant, which leads to the round shape of the cone.

Underlying is the theory that the fracture occurs at a certain distortion energy limit. Galles and Beckermann used the morphological similarity of foundry sand cores to soils to argue for a Drucker-Prager material model for foundry cores during casting (Galles and Beckermann, 2015). Thorborg et al. proposed to utilise the Drucker-Prager model to simulate the mechanical behaviour of core materials, as well (Thorborg et al., 2020).

Mohr-Coulomb The Mohr-Coulomb criterion describes shear-induced failure. It is a two parameter model which has the shape of a six-sided pyramid along the hydrostatic axis. The yield surface is shown in figure 2.9e and described by the equations (Benz and Schwab, 2008):

$$\tau_{max} = c + \sigma_n \tan(\phi), \tag{2.20}$$

where τ_{max} is the shear stress in the failure plane, σ_n the normal stress acting on the respective failure plane, c is the cohesion of the material and ϕ is the friction angle. In principal stress space this translates to a material failure if one of the following conditions is met:

$$\frac{|\sigma_1 - \sigma_2|}{2} = \frac{\sigma_1 + \sigma_2}{2} \sin(\phi) + c \cdot \cos(\phi), \tag{2.21}$$

$$\frac{|\sigma_3 - \sigma_1|}{2} = \frac{\sigma_3 + \sigma_1}{2} \sin(\phi) + c \cdot \cos(\phi), \tag{2.22}$$

$$\frac{|\sigma_2 - \sigma_3|}{2} = \frac{\sigma_2 + \sigma_3}{2} \sin(\phi) + c \cdot \cos(\phi). \tag{2.23}$$

The Mohr-Coulomb yield criterion is often used in geo-sciences, as well. In contrast to the Drucker-Prager criterion, it is a maximum shear stress criterion, which leads to the hexagonal shape in the deviatoric plane (normal to the hydrostatic axis). Since soil is known to fail in shear bands (Ehlers and Volk, 1997), the Mohr-Coulomb criterion is widely used in geo-sciences. Colmenares and Zoback compared different yield criteria and showed that the Mohr-Coulomb criterion fits especially well for sandstone, which is the closest analogy to foundry cores in geo-sciences (Colmenares and Zoback, 2002). However, the original criterion is not continuously differentiable, due to the edges of the hexagonal cone. This leads to several attempts to achieve a C1 (Sloan and Booker, 1986) or C2-continuous (Abbo et al., 2011) formulation of the Mohr-Coulomb criterion.

Ehlers Ehlers developed a yield criterion for soil problems, which is determined by seven parameters (Ehlers, 1993, p. 373):

$$\sqrt{J_{II}\left(1 + e_\iota \frac{J_{III}}{J_{II}^{3/2}}\right)^{e_\eta} + \frac{1}{2} e_\rho I_I^2 + e_\zeta^2 I_I^4} + e_\kappa I_1 + e_\xi I_1^2 - e_\chi = 0, \tag{2.24}$$

where J_{II} and J_{III} are the second and third invariant of the deviatoric stress tensor and I_I is the first invariant of the stress tensor. $e_{\iota - \eta}$ are the parameters, which describe the shape of the yield surface. The yield surface is shaped like a cigar along the hydrostatic axis, as shown in figure 2.9. In contrast to the Drucker-Prager and the Mohr-Coulomb models, the Ehlers model is able to describe a fracture due to pure hydrostatic pressure. Furthermore, the general shape of the yield surface can be adapted flexibly to a broad range of stability problems of porous frictional materials, due to the high number of parameters. In order to quantify the parameters at least one independent data point in principal stress space is necessary for each parameter. These data points are acquired with mechanical tests, which are described in the next section.

2.4 Mechanical Testing Methods

In this section, I will asses the state of the art for material testing methods with focus on uni- and multi-axial stress states. Literature with foundry core materials will be used where available, otherwise I will focus on articles, which are evaluating brittle materials, due to the similarity and transferability to foundry core materials. It is important to describe the whole stress field in the specimens precisely for later studies regarding the fracture statistics of the specimens. The mechanical representation of the test setups and the parameters in the following equations can be found in figure 2.10.

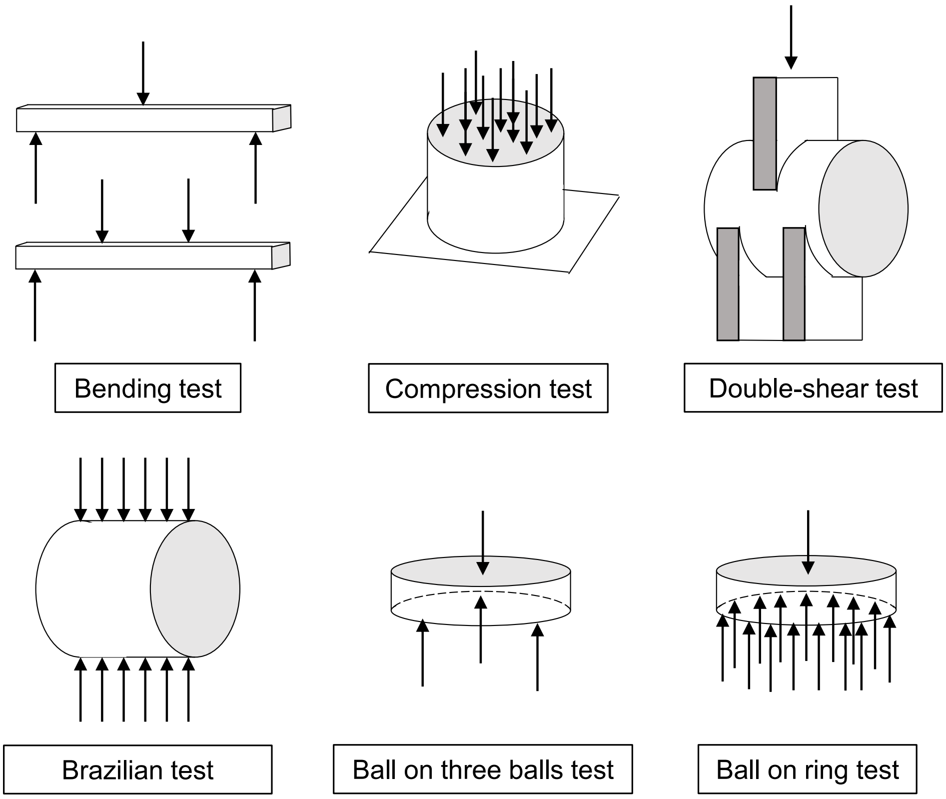

Figure 2.10: Mechanical testing methods for brittle materials and various stress states.

2.4.1 Uni-axial Testing

Bending Three-point-bending tests are the most commonly used tests of fracture strength for core materials. Stauder et al. test the properties of foundry sand cores this way (Stauder et al., 2016). The four-point-bending test uses two symmetrical load points to induce stresses in the specimen, as shown in figure 2.10. The advantage over the three-point-bending test is that the stress is more evenly distributed in the beam.

Griebel et al. used a four-point-bending setup to determine the Young's modulus of various foundry core materials (Griebel et al., 2016). The stress of three-point-bending σ_{3PB} and of four-point-bending σ_{4PB} is (Assmann and Selke, 2004):

$$\sigma_{3PB}(x,z) = \frac{\frac{F_{3PB}}{2}(x - 2\langle x - a\rangle^1)}{B} z, \tag{2.25}$$

where F_{3PB} is the force applied by the testing machine and a is the distance between the supports and the load point. B is the geometrical moment of inertia, and z is the distance from the neutral layer.

$$\sigma_{4PB}(x,z) = \frac{\frac{F_{4PB}}{2}(x - \langle x - a\rangle^1 - \langle x - (a+b)\rangle^1)}{B} z, \tag{2.26}$$

where F_{4PB} is the force applied by the testing machine, a is the distance from the supports to the load point and b is the distance between the load points. Both equations are in Föppl notation.

Compression Similar to bending, the compression test is widely used for foundry core materials. Izdebska-Szanda et al. use the compression test to characterise the strength of foundry core materials (Izdebska-Szanda et al., 2012). The stress σ_c in the specimen can be described as:

$$\sigma_c = \frac{F_c}{A}, \tag{2.27}$$

where F_c is the force of the testing machine and A is the area of the specimen which is loaded by the testing machine.

Brazilian test The Brazilian test consists of a cylindrical disc which is diametrically loaded by two parallel plates. The Brazilian test is often used as a test for tensile strength (Stauder et al., 2019). However, according to Li and Wong, the main stresses in the region around the plates are shear stresses, while in the middle tensile stresses predominate. (Li and Wong, 2013).

According to the norm ASTM (2008) D 3967-08 the most basic way to calculate the tensile stress in the disc is:

$$\sigma_b = \frac{2F_b}{\pi D h}, \tag{2.28}$$

where F_b is the testing force, D is the diameter of the disc and h is its thickness. There are several approaches to approximate the stress field in the disc more accurately (Li and Wong, 2013). However, Fairhust showed that due to the complex stress states in the disc the tensile strength of brittle materials is greatly underestimated by the Brazilian test. (Fairhurst, 1964)

Shear test From a kinematic point of view, shear stress can be induced by a torsional load or by a linear punch. Stauder et al. use a test setup called double shear test to induce stresses in cylindrical specimen of core materials (Stauder et al., 2019). The cylinder lies on two supports, while a punch induces stresses into the specimen, similar to a three-point-bending setup, as shown in figure 2.10. Since the clearance between the supports and the punch is near zero, the shear stresses predominate in the loaded part of the specimen. Stacey used a similar test to determine the shear strength of rock (Stacey, 1980). If the double shear test is applied for foundry sands the following equation is used to calculate the shear stress (Stauder et al., 2019):

$$\sigma_{sh} = \frac{2F_{sh}}{D^2 \pi}, \tag{2.29}$$

where F_{sh} is the testing force and D is the disc's diameter. Torsional tests aren't applied to foundry core materials, yet. However, they are used for ceramics, for example Ferraris et al. used a torsional test to determine the shear strength of silicon carbide (Ferraris et al., 2012).

2.4.2 Bi-axial Testing

Ball on ring/ ring on ring test The ball on ring and the ring on ring tests can be associated with a group of material tests, which are mainly used for brittle materials like ceramics and glass. This group of material tests uses mostly circular discs as specimens, which are loaded with bi-axial stresses. The load is induced by balls (point contact), which are arranged in a ring concentric to the disc, or by an actual ring (line contact). The support of the disc is realised analogously. There are multiple balls (point contact) arranged in a concentric circle or a ring (line contact), which support the disc. Depending on the number of balls in the rings, the contact is either modelled as a point contact or approximated as a line contact. The diameter of the ring of balls correlate with their quantity and diameter. The extreme case is one single ball in the middle of the disc.

Godfrey et al. first performed the ball on three balls test for ceramics, which uses one singular ball to induce the load and three balls as support (Godfrey, 1985). Ramakrishnan et al. adapted this test for core materials (Ramakrishnan et al., 2014). Fett et al. utilised a three ball on three ball test setup to determine the fracture strength of ceramics and compared the results to the ball on three balls test (Fett et al., 2007).

With and Wagemans analysed the ball on ring test regarding the evaluation of the stresses in ceramic specimen (With and Wagemans, 1989). They used multiple balls as supports and calculated the stresses in the plate with Bassali's solution (Bassali, 1960), which considers multiple support points as a point contact as follows:

$$\sigma_{1/2} = \frac{3p(1+\nu)}{4\pi h^2}\left(1 + 2(\ln\frac{a}{b}) + \frac{(1-\nu)a^2}{(1+\nu)R^2}(1 - \frac{b^2}{2a^2})\right), \tag{2.30}$$

where p is the load, h the disk thickness, a the radius of the circle of support points, b the radius of the region of uniform loading at the centre, R the radius of the disk and ν is Poisson's number. Please note that it is debated how the "region of uniform loading" can be determined best, since the ball contact is a point contact in theory only. Furthermore, this equation is an approximation for the symmetrical stress maximum in the disc. It is not possible to describe a continuous stress field in the whole disk with this equation.

Morell compares the various manifestations of these tests with their respective advantages and disadvantages. A ring contact offers a symmetrical stress field, which can be calculated easily, but can not cope with an out-of-flatness error of the specimen. A three-ball contact can cope with an out-of-flatness error, while the stress field under each ball can only be calculated with an approximation and the loaded volume is very small. (Morrell, 1998)

Uniform pressure on ring Shetty et al. developed the uniform pressure on ring test to compensate the main disadvantages of the ball on ring test: The approximation of the contact stress under the loading ball which is the point of likely fracture, and the small loaded volume in the specimen. The specimen is loaded with uniform pressure, which eliminates stress concentrations and is increasing the effective volume of the specimen through a more evenly distributed load. (Shetty et al., 1983)

According to Morell, the uniform pressure on ring test, can cope with out-of-flatness errors, if the support ring is flexible, but requires an expensive test jig (Morrell, 1998).

2.4.3 Tri-axial Testing

Tri-axial test-setups are designed such, that the specimen is loaded with a confining hydrostatic pressure. Additionally, an increasing deviatoric stress component is induced into the specimen until material failure occurs (Bésuelle et al., 2000). Tri-axial testing is widely applied in geo-sciences and rock mechanics. Bésuelle et al. investigated the localisation phenomenon in sandstone with tri-axial tests (Bésuelle et al., 2000). Roscoe and Poorooshasb studied the mechanical behaviour of normally consolidated clays (Roscoe and Poorooshasb, 1963). Li and Wong used tri-axial compression tests to build a failure envelope for granite and determined an increasing Young's modulus with increasing confining stress (Li and Wong, 2013). Müllerschön studied the elastic and plastic behaviour of unbound Berliner sand with tri-axial experiments (Müllerschön, 2000).

Kovari and Tisa introduced the multi-stage tri-axial test to reduce the amount of specimens needed for a failure envelope. As with the single-stage test, a hydrostatic stress is induced into the specimen. The deviatoric stress is increased until signs of failure are detected. Then the hydrostatic stress is increased while the deviatoric stress remains constant. This stops the failure and another point on the failure envelope can be determined. (Kovari and Tisa, 1975)

However, this method is debated, since it is difficult to stop the increase of deviatoric stresses in time without damaging the specimen excessively. This proves especially difficult for brittle specimens (Youn and Tonon, 2010). For this dissertation, the most promising articles study tri-axial compression tests on synthetic sandstone and core materials, since the material behaviour is more comparable and thus the results more relevant. Holt et al. found that for cement-bound, synthetic sandstone yield stresses increase with higher confining stresses (Holt et al., 1993). Caylak and Mahnken determined the thermo-mechanical behaviour of organic cold box foundry cores and found that from 1 to 10 bar confining pressure the yield shear stress of the specimen increases in a linear manner (Caylak and Mahnken, 2010).

All of these experiments lead to the conclusion that the yield stress of foundry cores is dependent on hydrostatic stress. However, all tri-axial experiments in literature are limited to compression, there is no tension or bending experiments under hydrostatic pressure for similar materials to foundry cores in literature. An extension of the specimen is usually achieved by reducing the pressure of one of the three principal stresses. This leads to an extension of the specimen in that direction due to transversal contraction.

2.4.4 Creep Behaviour

Some materials show an increasing and inelastic deformation, if subjected to constant loads below the limit of the material strength. This behaviour is called creep. Typically, creep shows under constant load three phases until material failure. (Scholz, 1968)

Figure 2.11 shows the strain and strain rate curve of a typical uni-axial creep experiment. The three phases primary, secondary and tertiary creep are marked. Primary creep with high and decreasing strain rates is followed by secondary creep with a constant strain rate. Eventually, the strain rate increases again, which is the beginning of the tertiary creep, which ends in fracture (Scholz, 1968). There are several mechanisms, which result in material creep. Typical mechanisms are diffusion (Herring, 1950), Harper-Dorn creep (Harper and Dorn, 1957) and grain boundary sliding (Langdon, 2000). Furthermore, there is evidence that in brittle rock the primary creep mechanism is micro-fracturing (Scholz, 1968).

The following power law, which is also called the Norton-Bailey creep law, describes the creep rate for uni-axial secondary creep (Bailey, 1935):

$$\dot{\epsilon} = K \left(\frac{\sigma}{\sigma_0} \right)^n , \tag{2.31}$$

where $\dot{\epsilon}$ is the strain rate, σ is the uni-axial stress, K, σ_0 and n are constants.

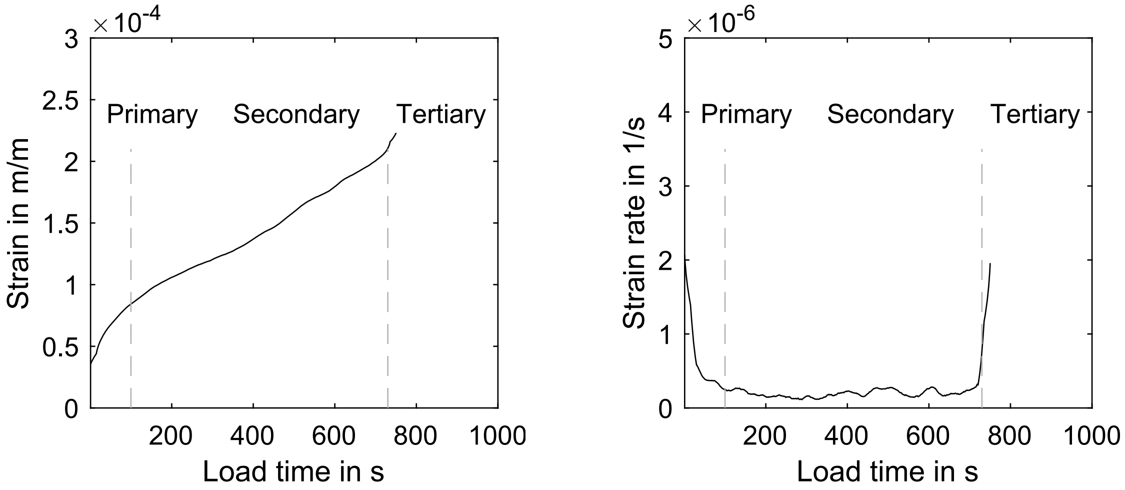

Figure 2.11: Creep experiment with constant load. The strain development for a bending experiment with constant load is shown. The plot starts as soon as the target load is reached and constant. The curve shows the typical three phases of creeping. On the right side the strain rate is shown.

This law can be adapted to describe primary and secondary creep (Murakami and Iwatsuki, 1969):

$$\dot{\epsilon} = K \left(\frac{\sigma}{\sigma_0} \right)^n \left(\frac{t}{t_0} \right)^o , \tag{2.32}$$

where t is the time, while o and t_0 are constants. The three constants K, σ_0 and t_0 can be combined to one single constant $\frac{K}{\sigma_0^n t_0^o}$, when the creep law is parameterised with experimental data. In literature, the creep behaviour of foundry cores is studied with regard only to hot distortion during casting at elevated temperatures. For example Bargaoui et al. studied the thermo-mechanical behaviour of resin-based binder for elevated temperatures (Bargaoui et al., 2017). Bakhtiyarov et al. modelled the hot distortion of core materials for aluminium castings (Bakhtiyarov et al., 2009). However, there is no specialised literature regarding the modelling of creep behaviour at room temperature, which could be used for handling and storage simulations of core materials.

2.4.5 Elastic Properties

The elastic properties of a material can be expressed as the Young's modulus E, the shear modulus G and the Poisson ratio ν. Only two of these variables are independent. If two of the parameters are known, the third can be calculated for isotropic materials (DIN 843-2, 2016):

$$\nu = \frac{E}{2G} - 1. \tag{2.33}$$

Generally, one can differentiate static and dynamic elastic properties (T. N. Keshishyan et al., 1975). The standard DIN 843-2 defines several static and dynamic methods to evaluate elastic properties of ceramics. Statically, the Young's modulus is quantified via three and four point bending. Dynamically, the Young's and shear modulus can be determined via ultrasound methods or via impulse excitation technique. Palachy et al. compared a static compression test with the impulse excitation technique for concrete and concluded, that the Young's modulus can be assessed more accurately with impulse excitation (Palachy et al., 2009).

Schneider et al. determined the Young's modulus of inorganically-bound core materials via ultrasound (Schneider et al., 2018). Stauder et al. evaluated the strain-stress-curve of a three-point-bending experiment to obtain the Young's modulus of foundry cores (Stauder et al., 2016). Griebel et al. assessed the static Young's modulus of foundry cores optically via four point bending (Griebel et al., 2016). However, currently there is no published work on the shear modulus or Poisson ratio of foundry cores.

For brittle materials like ceramics, the impulse excitation technique is common. The natural frequencies of the specimen are determined with this process (Atri et al., 1999). The specimen is excited by an impact, for example with a hammer. The subsequent free oscillations have to be recorded (Tognana et al., 2010), which can be achieved with several sensor concepts, like a contact-less vibrometer or piezo crystals (Roebben et al., 1997). Furthermore, the oscillations can be recorded with strain gauges or a microphone. Regardless of the method, the data is recorded in the time domain. Subsequently, the data is transformed from the time domain to the frequency domain via a Fast-Fourier-Transformation. Every eigenmode, which has been excited by the impulse is represented by a peak in the resulting spectrum.

Additionally, the dimensions and the mass of the specimen have to be known to calculate the elastic parameters from the spectrum. For a cuboid specimen with the mass M, the length l, the width w, and the height h, the approximate Young' modulus E and the shear modulus G can be calculated analytically (DIN 843-2, 2016):

$$E = 0.946\left(\frac{M f_{f_1}^2 l^3}{w h^3}\right)\left(1 + 6.585\left(\frac{h}{l}\right)^2\right), \tag{2.34}$$

$$G = \left(\frac{4 l M f_{t_1}^2}{w h}\right)\left(\frac{(h/w) + (w/h)}{4(h/w) - 2.52(h/w)^2 + 0.21(h/w)^6}\right), \tag{2.35}$$

where f_{f_1} and f_{t_1} are the first bending and torsional eigenfrequencies, respectively.

3 Research Gap, Objectives and Approach

Summarising the state of the art, it can be concluded that there is no validated mechanical material model for foundry cores. In order to facilitate mechanical FEM calculations of foundry cores, specific information is needed to fully parametrise the model:

- The density of the material has to be quantified.
- The yield criterion has to be known and validated.
- There have to be experiments to quantify all material parameters in the yield criterion. These experiments have to be comparable to contribute information to the same yield surface.
- The elastic parameters must be known.

The density of the core material can be easily quantified by determining the weight and the volume of a specimen. There are a few attempts to model foundry cores either with the Drucker-Prager (Thorborg et al., 2020) or the Mohr-Coulomb model (Stauder et al., 2019). However, all of them lack poly-axial validation experiments. The material models are simply parametrised with uni-axial experiments. The decision for the failure model type is based on the assumption that foundry cores behave analogously to soils or rocks. Dong et al. proposed to use a Rankine criterion for sand cores similar to ceramics (Dong et al., 2010).

Regarding the failure model, the state of the art is contradicting, since more recent publications utilise models from geo-sciences, which describe a fracture stress dependent on the hydrostatic pressure. They do not consider size effects for their parameterisation experiments, while Dong et al. utilise a tensile stress based criterion independent of hydrostatic pressure.

Material testing of foundry cores is mostly uni-axial, with the notable exception of the ball on three balls experiment of Ramakrishnan et al. (Ramakrishnan et al., 2014) and the tri-axial compression test (Caylak and Mahnken, 2010). In order to characterise the shape of a yield surface in the deviatoric plane, bi-axial experiments are needed in all quadrants of the plane stress state. There need to be test setups for tension-tension, tension-compression and compression-compression experiments. The state-of-the-art tension-tension experiment is the ball on three balls experiment, which is debated due its significant stress peaks under the load balls. The current tension-compression experiment is the double shear test, which introduces significant stress peaks into the surface of the specimen at the edges of the testing tool. At the moment there is no test setup for foundry cores to characterise the fracture with a bi-axial compressional load. In order to determine the friction angle of the yield surface, it would be desirable to determine the fracture stress with different hydrostatic stress states not only for compression but also with tension/bending experiments.

For a reliable parameterisation of material models, there needs to be a new set of poly-axial experiments, which cover all quadrants of the plane stress state, without unpredictable stress peaks.

For the calculation of strains and stresses with FEM, the elastic parameters have to be determined. The Young's modulus of cores is quantified with different methods in the state of the art. However, there is no method to measure the shear modulus or the Poisson number, yet. These values are usually taken from measurements on soils or rocks (Galles and Beckermann, 2015).

This leads to the research approach of this dissertation. The following research steps are built on one another in order to achieve the main goal of a material model, which can be used to calculate the mechanical reaction of foundry cores to typical loads in handling and storage processes.

- Analysis of the fracture statistics and validation of the volume correction according to the weakest link theory in case of a Weibull distribution.
- Development of a non-destructive method to determine the elastic parameters via impulse excitation.
- Development of bi- and tri-axial material tests to parametrise and validate a suitable model.
- Implementation of this material model into a FEM software and application to complex core geometries and stress states.
- Validation of this simulation with experiments on the same geometries.

An overview of the work in this dissertation is shown in figure 3.1

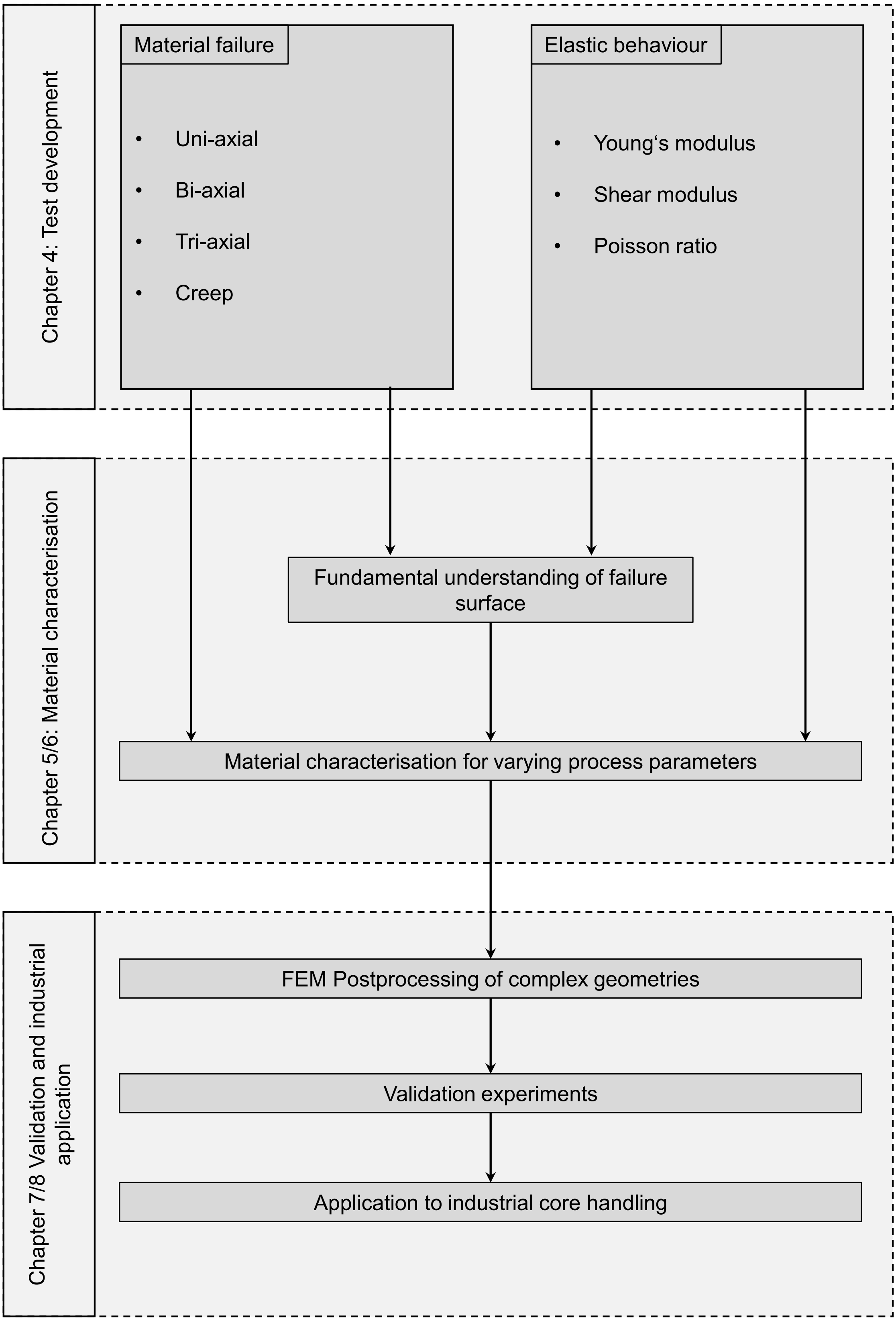

Figure 3.1: Overview and structure of the research in this dissertation.

4 Materials and Methods

This chapter describes the core materials which are utilised in characterisation experiments and the methods involved in performing and evaluating these experiments. It is structured in three sections. In the first section, the specimens necessary to characterise the mechanical behaviour are described. The second part details the testing methods which are applied to these specimens. The third section describes the simulation models of this thesis.

4.1 Specimens

In a first step, I will describe the specimens for all performed experiments. The differing requirements of the following experiments lead to different specimens for these experiments. This section details their geometry, the utilised sand-binder systems and their production process.

4.1.1 Geometry

There are four types of specimens, which are utilised for material characterisation in this work. Each type of specimen is utilised to study the mechanical reaction to specific stress states, which will be described in section 4.2. A bending beam with a quadratic cross-section with 22.8 mm edge length and a length of 173 mm, a disc with 45 mm diameter and 6.3 mm height and a cylinder with 50 mm diameter and 50 mm height. The bending beam is either used for bending experiments in its full length or shortened to a cubical shape and a length of 20 mm for compression tests. The disc is used for bi-axial bending tests, while the cylinder is utilised for Brazilian tests. They are shown in figure 4.1. For validation purposes, I also utilise a complex three cylinder water jacket core geometry, which is shown in figure 4.2. The core geometry is developed by the BMW AG (Munich, Germany) for its three cylinder combustion motor in the I8 automobile. In the validation section it will be subjected to different loads which result in complex stress states suitable to validate the material models found in this dissertation.

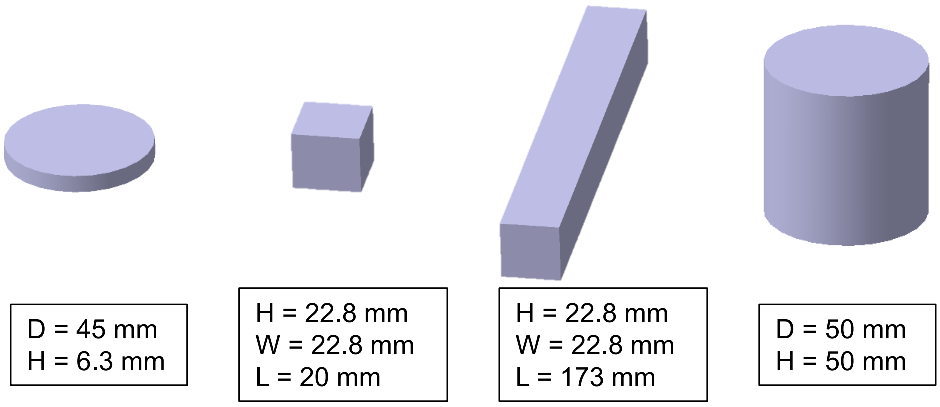

Figure 4.1: Specimens used for the experiments in this dissertation. A disc with 45 mm diameter and 6.3 mm height, two cuboids with a 22.8 x 22.8 mm^2 cross-section and a length of 20 mm and 175 mm, respectively and a cylinder with 50 mm diameter and 50 mm height.

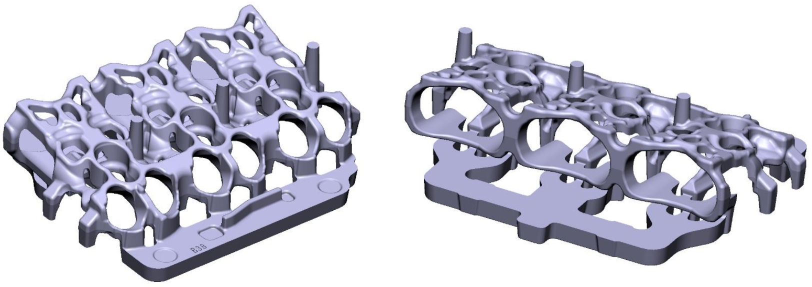

Figure 4.2: BMW I8 water jacket core geometry utilised for the validation of the material models.

4.1.2 Sand-Binder Systems

In this dissertation, I focus on inorganic core materials, bound with sodium silicates. Additionally, I compare important material parameters to typical organic furan-based cold box systems. This will show the differences of the mechanical behaviour between those universal binder classes, which have to be considered when modelling either organic or inorganic sand-binder-systems. Most experiments are performed with derivatives of the Inotec system from ASK Chemicals GmbH (Hilden, Germany). The main organic binder system is the Sigmacure system from Hüttenes-Albertus Chemische Werke GmbH (Düsseldorf, Germany), which is a classic furan-based binder system with amine hardening.

Several sand-binder systems for each chemical binder class are utilised for the experiments which characterise the probabilistic distribution of core fracture, since these results build the foundation for the subsequent experiments. Section 2.3.1 showed that the fracture statistics can influence the material strength. Therefore, it is important to generalise these findings and to show that they apply to several binder systems from two leading chemical companies. The following naming convention is utilised for these binder systems:

The chemical class is defined by the prefix "IN" for inorganic and "OR" for organic binder systems. The Inotec binder system from ASK Chemicals is denoted as IN-1, while the Cordis system from Hüttenes-Albertus is referenced as IN-2. The organic binder systems are referenced as OR-1 to OR-3. These organic binder systems represent furan systems from Hüttenes-Albertus, which utilise varying solvents and resins. The specifics for the sand-binder-systems can be found in table 4.1. The amount of binder and additives are noted, which account for most experiments. If the binder amount is varied, it will be explicitly stated in the respective section. Sand from Quarzwerke GmbH (Frechen, Germany) is utilised in all sand-binder systems. In most cases (IN-1 and OR-1-3) a H32 silica sand is used, while for the IN-2 system a F34 sand was chosen. The IN-2 differs from the IN-1 systems in binder and sand to show that the fundamental assumptions which build the basis for this work are valid and independent of the type of water-glass binder system and of the silica sand used.

Table 4.1: Overview of the sand-binder systems utilised. There are three commercial inorganic binder systems and three commercial organic binder systems.

Ref.	Sand	Binder system	Part 1	Part 2	Hardening
IN-1-1	H32	Innotec	EP 4158 2 wt-%	TC 4500 1.6 wt-%	heated core box
IN-1-2	H32	Innotec	EP 4158 2 wt-%	WJ 4500 1.8 wt-%	heated core box
IN-2	F34	Cordis	DSL 5 2.3 wt-%	DSL 6 1.3 wt-%	heated core box
OR-1	H32	Biocure	7241 P1 0.7 wt-%	6324 P2 0.7 wt-%	amine gas
OR-2	H32	Sigmacure	6966 P1 0.7 wt-%	8431 P2 0.7 wt-%	amine gas
OR-3	H32	Sipurid Silcure	9832 P1 0.7 wt-%	8484 P2 0.7 wt-%	amine gas

4.1.3 Production Process

The IN-1 specimens mainly utilised for the following experiments are produced on a Loramendi SLC2-25L core shooting machine (figure 4.3) at the Chair of Metal Forming and Casting, Technical University of Munich (utg). Specimens of type IN-2 and the organic specimens OR-1 to OR-3 are produced by Hüttenes-Albertus Chemische Werke GmbH on a core shooting machine from Multiserw and delivered in an air-tight package. The following description of the core production is applicable for the specimens produced at utg.

The appropriate quantity of liquid binder and powdered additives are measured on a precision scale Kern PCB 250 (KERN & SOHN GmbH, Balingen, Germany) with a maximum load of 250 g and a scale from Steinberg Systems SBS-LW-7500A for higher weights. The sand and the binder are brought together in a mixer from Loramendi of the type MDR-0.5. In a first step, the sand is mixed with the dry powdered constituents of the binder system for 60 s at a speed of 80 rpm. Secondly, the fluid binder is added to the mixture and processed for another 60 s. The sand has to be mixed long enough to ensure a homogeneous sand-binder system. On the other hand, the mixing process is increasing the temperature in the sand, due to the friction between the grains. The increased temperature may lead to premature hardening of the sand-binder system. Therefore, the mixing parameters have been chosen with preliminary experiments to meet both requirements. The mixing quality has been controlled continuously via visual inspection during core production. The sand-binder mixture is shaped to cores in the core shooting machine by shooting it into a core box, where it is hardened by the heated core box and a hot-gassing mechanism. The shooting and hardening process is characterised by the parameters in table 4.2. The shooting pressure describes the pressure of the air transporting the sand-binder mixture into the core-box. The air temperature and the gassing time describe

Figure 4.3: Loramendi core shooting machine SLC2-25L, which is utilised for the specimens of type IN-1 in this thesis.

the temperature and the length of the hot gassing. The tool time stands for the time span, the specimen is in contact with the heated core box, this includes the gassing time.

After the core shooting process, the produced cores are removed from the box by actuators in the tool and picked up by the operator. They rest until the end of the production session on a steel lattice and are then put into a climate chamber for 24 h-48 h at 10 % relative humidity and 20 °C. Experiments with different storage times and climatic conditions are indicated specifically.

Table 4.2: Production parameters for the core shooting of the specimens.

Ref.	Tool temp.	Tool time	Gas temp.	Gassing time	Shooting pressure
IN-1-1	155 °C	32 s	220 °C	15 s	5.5 bar
IN-1-2	155 °C	32 s	220 °C	15 s	5.5 bar
IN-2	170 °C	30 s	200 °C	30 s	4 bar
OR-1	-	-	-	10 s	4 bar
OR-2	-	-	-	10 s	4 bar
OR-3	-	-	-	10 s	4 bar

4.2 Material Testing

In the following section, I will describe the testing methods, which were utilised to characterise the mechanical behaviour of core materials. The objective is to develop methods to determine which failure model is suitable for core materials and to parametrise it. The elastic parameters of core materials will be calculated from eigenfrequencies in a non-destructive manner with a newly developed test bench. The material strength will be evaluated with test setups developed for specific load cases, which allow differentiating between the failure models described in section 2.3.2. The uni- and bi-axial tests are performed on a universal testing machine Zwick Z020 with a 20 kN force sensor (ZwickRoell GmbH & Co. KG, Ulm, Germany). One exception are the creep tests, which are performed on the Z020 with a 500 N force sensor. The tri-axial tests are performed in a novel testing machine, developed for compression and bending tests under hydrostatic pressure. The fracture strain is determined via a high-speed digital image correlation setup which was adapted from the work of Hartmann (Hartmann et al., 2018).

4.2.1 Test Setup for Acoustic Determination of Elastic Properties

In order to determine the elastic properties of core materials a novel test setup[1] has to be developed to accommodate all requirements. The most important feature is that it is possible to determine both, the Young's and the shear modulus, using only one test setup. The shear modulus and the Poisson ratio of core materials were never quantified before, while the Young's modulus has been evaluated with several destructive and non-destructive methods, as shown in section 2.4.5. I chose a non-destructive testing method, since the same specimen can be evaluated for its elastic constants and afterwards for its material strength. Besides the obvious economical advantage, this offers the chance to directly correlate individual specimen instead of whole data sets with their underlying fracture statistics. The most promising method to non-destructively determine the elastic constants is the impulse excitation technique, which calculates the elastic constants based on the eigenfrequencies of the specimen. Based on this, an automatic test setup was developed to acoustically acquire the eigenfrequencies of the test specimen and to evaluate the data based on the dimensions and the weight of the specimens. In a first step, this evaluation is performed based on equations 2.34 and 2.35. The test setup is shown in figure 4.4.

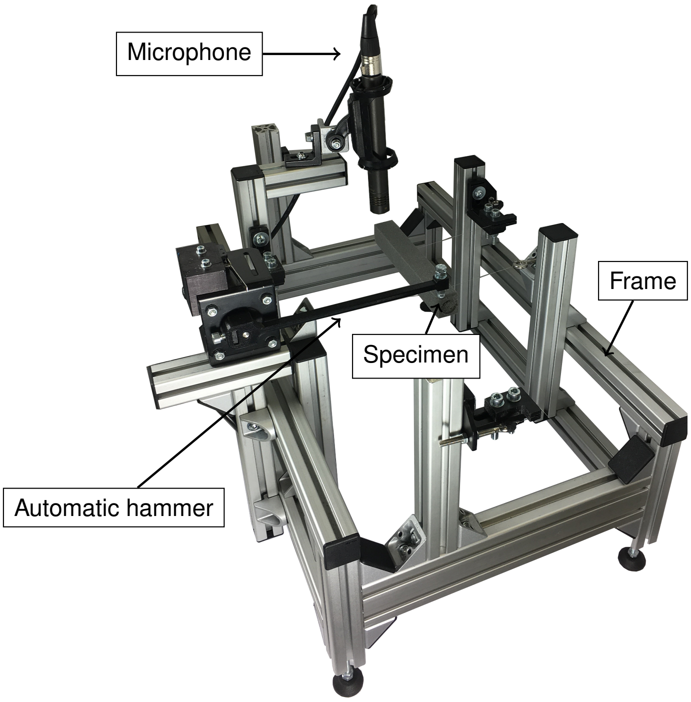

Figure 4.4: Test-bench for determining elastic properties via impulse excitation technique. An impulse is induced into the specimen and the subsequent oscillations are acquired with the microphone. (Lechner et al., 2020)

---

[1] The test bench was dimensioned and built in a master's thesis by Georg Fuchs under my supervision. It has been published with an additional signal evaluation and first results (Lechner et al., 2018 and Fuchs, 2016).

On a functional level, it has three modules:

- The automatic hammer, which hits the specimen to excite the oscillations needed to determine the eigenfrequencies.
- The control unit, which controls the hammer and records the oscillations of the specimen with a microphone.
- The support structure, which holds the hammer, the microphone and the specimen in place.

The specimen rests on two parallel steel wires, which allows almost free oscillations of the specimen. The impact on the specimen needed to excite the eigenfrequencies is induced by the automatic hammer system. The hammer itself is produced from an ABS polymer and designed to be flexible. Due to the oscillation of the hammer after the impact, one typical problem with automatic hammer systems are multiple hits of the specimen. The high flexibility of the hammer decreases the frequency of these oscillations. This makes it necessary to retract the hammer before a second hit of the specimen occurs. The hammer is controlled by a stepper motor, which in turn is controlled by a Raspberry Pi computer system. The Raspberry Pi is the central control unit of the test setup and triggers the hammer impact and the recording of the data with a S241 Superlux microphone. Furthermore, it calculates the eigenfrequencies from the recorded data with a Fast-Fourier-Transformation (FFT) and a peak finding algorithm. Based on these results a first estimation of the elastic constants is provided according to equations 2.34 and 2.35. The sampling frequency of the system is 96 kHz which leads to a resolution in the frequency domain of 6 Hz, which in turn leads to a resolution of approximately 36 Pa of the Young's and shear modulus.

Signal evaluation For technical ceramics, equations 2.34 and 2.35 can be used to calculate the Young's and shear modulus according to DIN 843-2. As a first estimation, the test bench evaluates the signal according to these equations. The first experiments with this test bench have shown, that these equations, which only use the first flexural and torsional eigenmode, do not model the oscillation behaviour of core materials accurately. To evaluate the acoustic signal more accurately, multiple eigenfrequencies are used to calculate the elastic constants.

In the following, this algorithm will be detailed. In a first step, the theoretical eigenfrequencies are calculated with the FEM-Software Abaqus 2018 (Dassault Systems, Velizy-Villacoublay, France). The simulation itself will be detailed in section 4.3. The eigenfrequencies resulting from the FEM calculation depend on the Young's modulus, the Poisson ratio, the weight and the dimensions of the specimen. I calculated the eigenfrequencies at several support points around the estimated values for the Young's modulus and Poisson ratio. The dimensions and the weight of the specimens remain constant. The production process of the specimens is precise enough to neglect the dimensional tolerances of the specimens and to assume a constant weight for the simulation. Thus, the simulation is parametrised with the average weight and dimensions of the specimens. The validity of this assumption was constantly checked during the experiments by determining the dimensions and the weight of the specimens.

The FEM results are utilised to build a linear model, which estimates the eigenfrequencies for the specific specimen at hand based on the input parameters Young's modulus and Poisson ratio. This model can be used to fit the eigenfrequencies found in FEM to the experimental frequency peaks in the experimentally obtained signal, with an error function which calculates the root-mean-square error for multiple peaks between experiment and simulation. A scheme for this algorithm is depicted in figure 4.5. I calculated the Young's modulus and the shear modulus based on experimental data from the first flexural and torsional eigenfrequencies with equations 2.34 and 2.35. Furthermore, the Poisson ratio was determined with equation 2.33. The higher eigenmodes were calculated based on these results and the FEM simulation. Figure 4.6 shows a spectral analysis of one exemplary data set. The peaks of the eigenmodes are very pronounced and the calculated eigenfrequencies are depicted as dashed lines. The notation is f, t, l for flexural, torsional and longitudinal eigenmode with the number in the index. Naturally, the first flexural and torsional eigenmode fit very well to the experimental data. However, the calculated eigenmodes >6 kHz do not fit to the experimentally obtained ones anymore. Especially the higher torsional eigenfrequencies are not modelled properly. The real mechanical behaviour differs from the elastic two parameter material model used for the FEM calculation. This can be quantified by calculating the ratio of two successive eigenfrequencies. For example, the ratio of the second and the first flexural eigenmode is 2.54 based on the FEM calculations

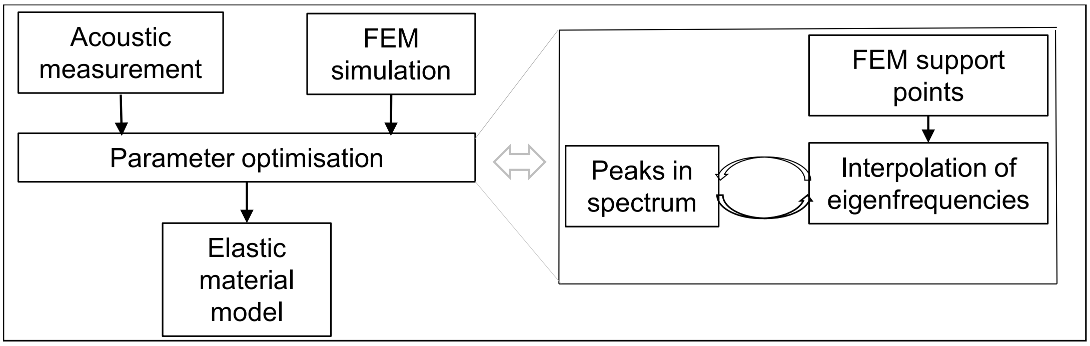

Figure 4.5: Scheme of the evaluation algorithm for the impulse excitation data. Peak positions for several combinations of Young's modulus and Poisson ratio are calculated as support points. The elastic parameters are optimised such that the error between the experimental and theoretical eigenfrequencies are minimised. (Lechner et al., 2020)

and it is independent of the elastic parameters themselves. Therefore, it can serve as an indicator how well the model itself fits the physical reality. Table 4.3 shows a comparison between the simulation and the experiment for six specimens. With one exception, all experimentally obtained frequency ratios are very close to the ratios from simulation. However, the ratio f_{t2}/f_{t1} is significantly smaller in the experiment than in the simulation (1.81 compared to 2.00), while the other torsional ratio f_{t3}/f_{t2} fits to the results of the simulation. This indicates that the first torsional eigenmode is an outlier compared to the other frequency peaks, which are described well by the elastic model in FEM.

To analyse this further, I changed the steel wire support from parallel wires to the shape of a cross. With impulse excitation technique, one tries to enhance one specific eigenmode with the support. If for example one would like to use specifically the second flexural eigenmode, the support wire should be parallel and in the nodes of the oscillation. The support wires will damp all eigenmodes to a certain degree, whose node do not coincide with the location of the steel wires. For torsional eigenfrequencies, the DIN 843-2 recommends a cross shaped wire support with the intersection of the wires in the middle of the beam. However, this did not change the results significantly, t_1 remained an outlier compared to the theoretical elastic model.

As a second test, I used a steel beam on the test bench. The ratio f_{t2}/f_{t1} was close to 2.00, which coincides with the theoretical model. This indicates that the outlier for core materials is due to the material itself and not the test bench. This leads to the decision that more eigenmodes have to be considered when calculating the elastic constants to model the mechanical behaviour best.

Figure 4.7 shows an example spectral analysis after the parameter optimisation (eigenmodes used: f_1, f_2, f_3, t_1, t_2, t_3, l_1, l_2). The simulated eigenmodes match significantly better to the measured spectrum. Therefore, I will utilise multiple eigenmodes for the calculation of the elastic parameters in this work.

Table 4.3: Ratios of successive natural frequencies. This value is independent from the elastic constants and can serve as an indicator for the model quality. The standard deviation is indicated in the brackets.

	f_{f_2}/f_{f_1}	f_{f_3}/f_{f_2}	f_{t_2}/f_{t_1}	f_{t_3}/f_{t_2}	f_{l_2}/f_{l_1}
Simulation	2.54	1.78	2.00	1.50	2.00
Experiment	2.57 (±0.03)	1.75 (±0.01)	1.81 (±0.01)	1.53 (±0.05)	1.95 (±0.07)

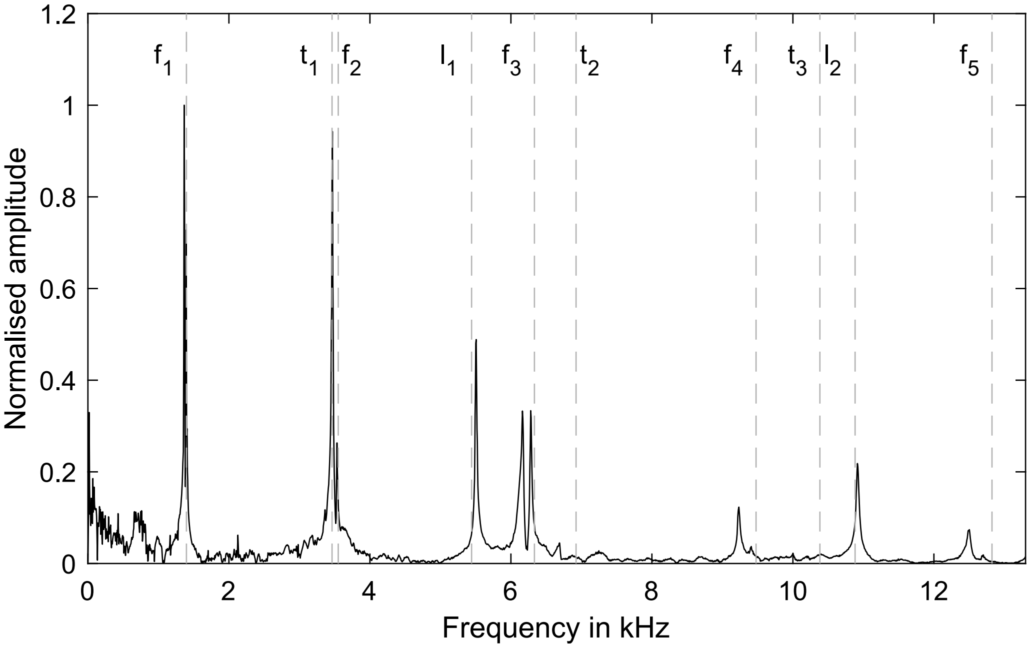

Figure 4.6: Spectrum of the impulse excitation data. The peaks in the spectrum indicate eigenfrequencies. The dashed lines show expected frequencies calculated with FEM, with elastic constants determined analytically using f_1 and t_1. (Lechner et al., 2020)

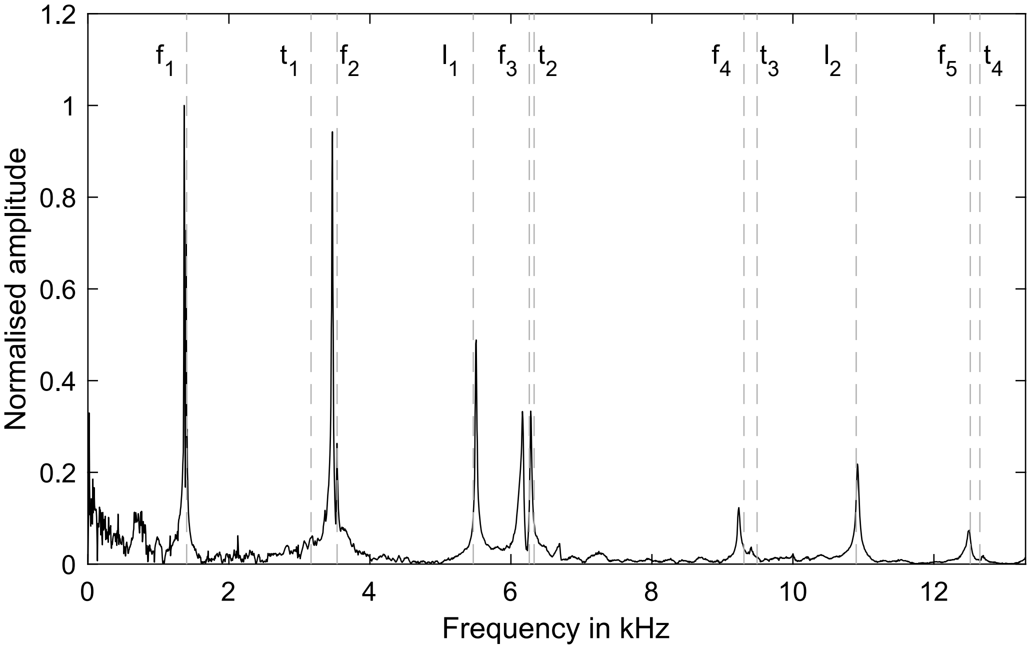

Figure 4.7: Spectrum of the impulse excitation data. The dashed lines show expected natural frequencies based on FEM calculations. The Young's and shear modulus of the material model are obtained with an error minimisation between the peaks in the experimental spectrum and the predicted eigenfrequencies. (Lechner et al., 2020)

4.2.2 Optical High-Speed Strain Measurement via Digital Image Correlation

The determination of the fracture strain for core materials has been performed with a digital image correlation (DIC) algorithm, which was developed by Hartmann et al. for the analysis of shear cutting operations (Hartmann et al., 2018). The images are recorded with a high-speed camera (Os3-S2 from IDT, Pasadena CA, USA) with magnification optics (Ultrasonic from Canon, Tokyo, Japan). The images are recorded at a frequency of 8500 Hz and in 8-bit greyscale format, which allows to evaluate the strain just before the first localisation of strains, which starts the subsequent fracture. The region of interest is illuminated by a Xenon Nova 300 W macro cold light source, which ensures sufficient exposure during high-speed recordings. DIC algorithms need sufficient texture on the specimen to calculate the strains in the material which is typically achieved by an artificial speckle pattern. Fortunately, the pores of the specimen can be utilised to evaluate the images without a speckle pattern (Lechner et al., 2020).

The algorithm is based on a classical block matching scheme and is an adapted version of the ICGN algorithm by Pan et al. (Pan et al., 2013). First-order shape functions for warping, a subset size of 15×15 pixels and a discrete cosine transform filter proposed by Garcia are used (Garcia, 2010). Further details on the precision, accuracy and implementation of the algorithm are presented by Hartmann et al. (Hartmann et al., 2018).

This DIC algorithm is utilised to evaluate the fracture strain in test setups, which do not allow to calculate the fracture stress in an analytic manner. In this case, the fracture strain and the elastic constants can be utilised to determine the fracture stress.

4.2.3 Uni-axial Testing

Uni-axial compression experiment The 20 mm × 22.8 mm × 22.8 mm cube is utilised for uni-axial compression tests. The load F_c is induced on the area A by the universal testing machine. Consequently, the fracture stress can be calculated as follows:

$$\sigma_c = \frac{F_c}{A}. \tag{4.1}$$

The test is performed between two parallel steel surfaces, as depicted in figure 4.8 on the right hand side. Additionally, a 1 mm polymer layer is placed between the steel tools and the specimen. This polymer layer compensates for minor out-of-flatness errors in the surface of the specimen and ensures a homogeneous stress field in the specimen. Thus in theory, the stress field is constant over the whole volume. This assumption will be checked later with a FEM simulation. In principal stress space this stress state can be be expressed with a uni-axial negative σ_2 stress. Figure 4.9 shows its position and the position of the following uni- and bi-axial test setups in principal stress space.

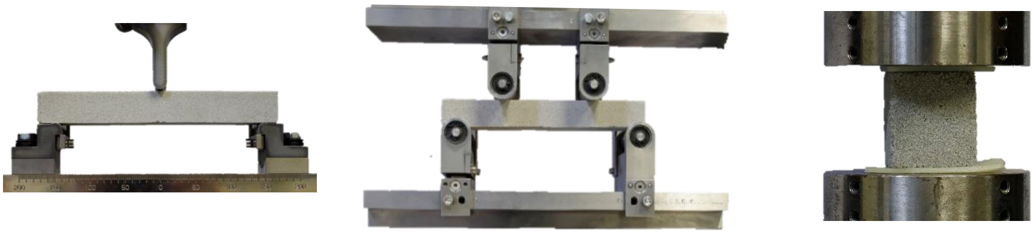

Three-point-bending

Four-point-bending

Compression

Figure 4.8: As uni-axial test methods a three-point-bending (left), a four-point-bending (middle) and a compression test setup (right) are utilised.

Uni-axial Tension Experiment As shown in section 2.4.1 several testing methods can be found in literature to determine tensile strength of frictional materials. In particular, bending, dog-bone and Brazilian tests would be a possible choice. For the experiments in this study, I chose bending experiments to determine the material strength under a uni-axial tensile stress state. This decision is due to the experimental and analytic disadvantages of the dog-bone and the Brazilian test. The dog-bone test, as for example utilised by Zaretztkiy, is in my experience experimentally less stable than the bending experiments, since the clamping of the specimen often leads to fracture in the vicinity of the clamping mechanism, instead of the intended area (Zaretskiy, 2016). This renders the result invalid. The Brazilian test induces a complex stress field into the specimen (Li and Wong, 2013). In theory, the two load points of the Brazilian test are line contacts, which is only an approximation for the small surface which is in contact with the testing machine. This load surface is smaller than the necessary RVE size (Schneider et al., 2018). Thus, the sand-binder compound can not be treated as an ideal continuum. This makes an analytic evaluation of the experiments difficult. Therefore, the Brazilian test is not suitable as a uni-axial characterisation experiment, but an adaption will be revisited as a validation experiment. The bending experiment offers experimental stability and an analytic solution, which can be easily validated with a FEM analysis. I utilised three-point-bending and four-point-bending test setups in the following experiments, as specimens served the bending beam described in section 4.1.1. The stress in the beam can be calculated with Bernoulli's beam theory for both cases and the equations 2.25 and 2.26.

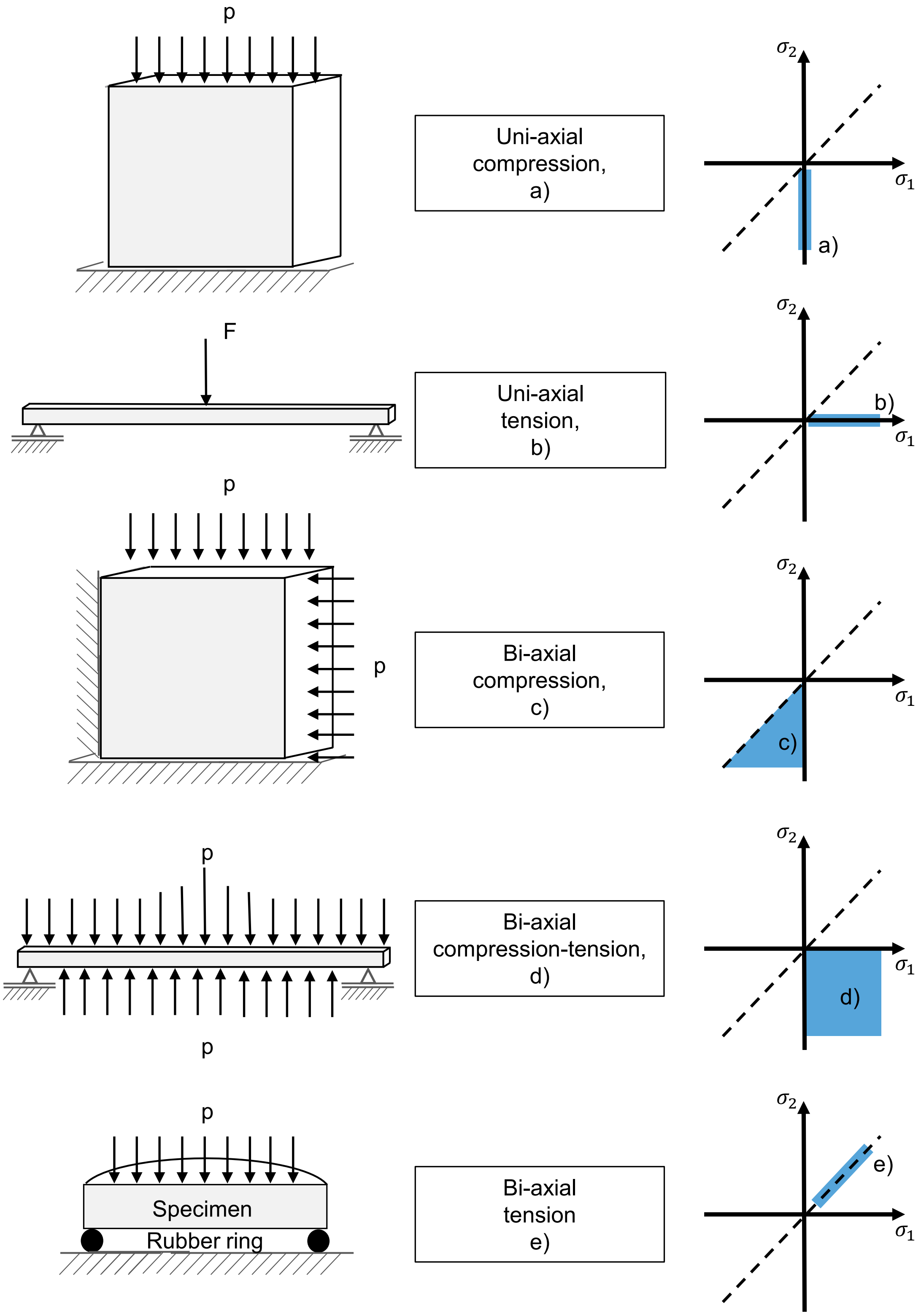

Figure 4.9: Uni- and bi-axial testing methods for compression (a), tensile (b), bi-axial compression (c), compression-tensile (d) and bi-axial tensile (e) stress states. The blue areas on the right side show their possible stress states in the principal stress space. The dashed line is the projection of the hydrostatic axis. (after Lechner, Hartmann et al., 2021)

4.2.4 Bi-axial Testing

Bi-axial Compression Experiment In order to induce a constant bi-axial compression stress state into the cubic test specimen shown in figure 4.1, a novel test setup was developed, which allows to use the single axis of movement from the testing machine to load the specimen with two orthogonal stress fields. The force of the testing machine is redirected by two wedges and a support to the vertical oriented sides of the cubic. The test jig is shown in figure 4.10.

The specimen can be positioned into the support tool with three orthogonal planes. The two remaining vertical sides of the cube are loaded by the wedges, which are guided by inclined planes in the support tool. Both the wedges and the planes in the support tool have an angle of 60°, which results in a constant compression of the specimen, if the wedge is forced down by the testing machine. All load-bearing contacts to the specimen are equipped with a 1 mm polymer pad to ensure a constant stress field and to allow for an approximately free transversal contraction of the cubic. The pads also allow inducing pressure into the surfaces up to the edges of the cubic; with a hard contact a collision between the wedges would occur. Additionally, the force of the wedge is transmitted by a plate to the polymer pad, since the downward movement of the wedge introduces friction to the contact surfaces. This plate ensures a contact to the specimen without movement and transmits only the pressure, while the frictional forces induced by the movement of the wedges are lead directly into the support tool. Additionally, all contacts of the wedges are coated with Teflon to decrease friction. The force of the testing machine is

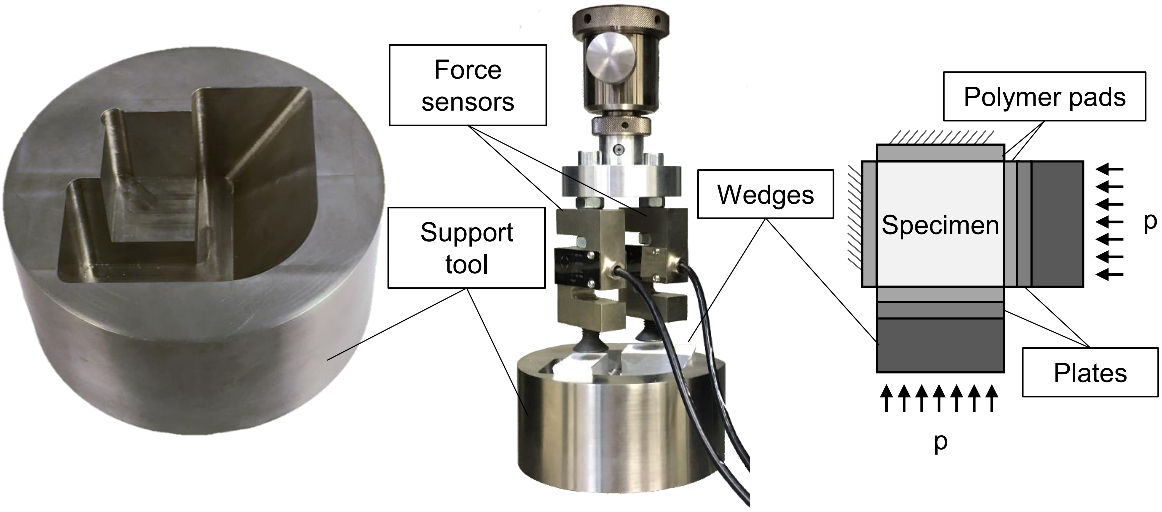

Figure 4.10: Test setup for bi-axial compression experiments on a universal testing machine. The force of the testing machine is redirected to two orthogonal sides of the cubic specimen by wedges. The opposite sides of the specimen are supported by the tool. (Lechner, Hartmann et al., 2021)

transmitted by two force sensors S20S (Bosche GmbH & Co. KG, Damme, Germany). The contacts between the force sensors and the wedges can be adjusted by screws, which allows to fine-tune how the force of the testing machine is divided between the wedges. With the angle of the wedges, the force F_p applied to one side of the specimen can be calculated to:

$$F_p = \tan(\pi/3)F(1 - \vartheta), \tag{4.2}$$

with F being the force of the testing machine on each wedge and ϑ the friction coefficient.

The test setup induces approximately a plane stress compression state into the specimen, if stresses resulting from transversal contraction and friction are neglected, since the last side of the cubic remains free. This assumption holds true, since the stresses from transversal contraction and friction are greatly reduced due to the polymer pads. Analogously to the uni-axial compression experiment, theory dictates that the bi-axial stress is constant over the whole volume. This assumption will be checked with FEM in the discussion. An advantage of this type of test setup is that a uni-axial compression stress state can be achieved as well by using only one wedge. This allows to compare the conventional uni-axial compression test with the new test setup and to empirically quantify the additional friction, which is introduced with the wedges. I quantified the friction coefficient ϑ to be 0.074 for each wedge by comparing the fracture strength for each uniaxial compression setup. This friction coefficient can be utilised as a scalar correction factor.

Shear Stress Experiment The state of the art offers classical double shear tests to evaluate the shear strength of core materials. However, this test setup has the disadvantage that for pure shear stress the clearance between the punch and the support would have to be approximately zero, which cannot be achieved in real experiments. Furthermore, the surface load on the edge of the tool is too high, which induces a local surface fracture influencing the accuracy of the results negatively, since it creates a defect which induces early fracture. Therefore, another test setup is necessary to determine the shear strength.

Transformed into principal stress space, pure shear stresses become a bi-axial stress state with a tension and a compression component (Mang and Hofstetter, 2013, p. 59). On the right-hand side, figure 4.11 shows one example of a Mohr's stress circle for a pure shear stress state τ_1 and the principal stresses σ_1 and σ_2 which can be calculated with a coordinate transformation. Therefore, a test setup has to be developed, which induces such a stress field into a specimen. The three-point-bending experiment described in section 4.2.3 induces a uni-axial tension in the lower half of the beam. To achieve an orthogonal compression component, I added two steel beams to the experiment (length: 173 mm, width: 22.8 mm, height: 8 mm).

The core material beam is positioned between these two steel beams in a sandwich-like setting. The three layers are not connected and can move relatively to each other. If the testing force of the three-point-bending experiment is applied to the sandwich, the three components are deformed together. The lower steel beam is deformed by the pressure on the contact surface to the core material. The same pressure acts on the core material as well, which adds a second compressive stress component to the specimen which is approximately orthogonal to the stresses resulting from pure bending. The test setup is depicted in figure 4.11. The bi-axial normalised stress field is shown in figure 4.12. In the experiment, the DIC algorithm described in section 4.2.2 is utilised to evaluate vertical, horizontal and shear strain components. Together with the Young's modulus, the stress state can be calculated with Hook's law, which was shown for uni-axial bending in a previous article (Lechner et al., 2020).

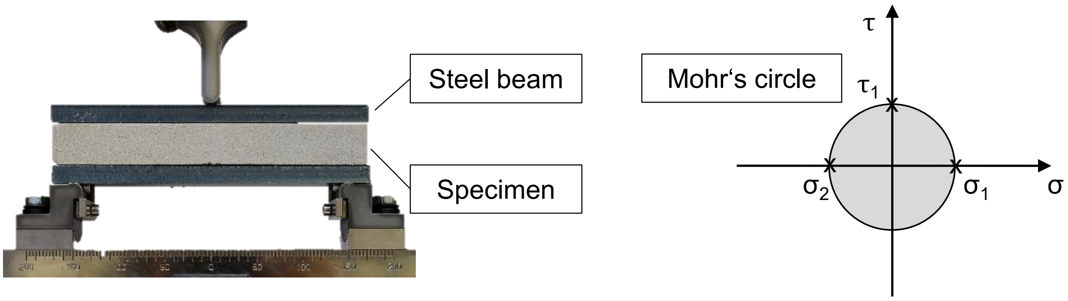

Figure 4.11: Test setup for a bi-axial tension-compression stress state. A three-point bending test setup was adapted to achieve a bi-axial tension-compression stress state. Additional steel plates induce compressional stresses into the specimen which are approximately orthogonal to the bending stresses resulting from the three-point-bending. The figure on the right-hand side shows a Mohr's stress circle for a pure shear stress state.

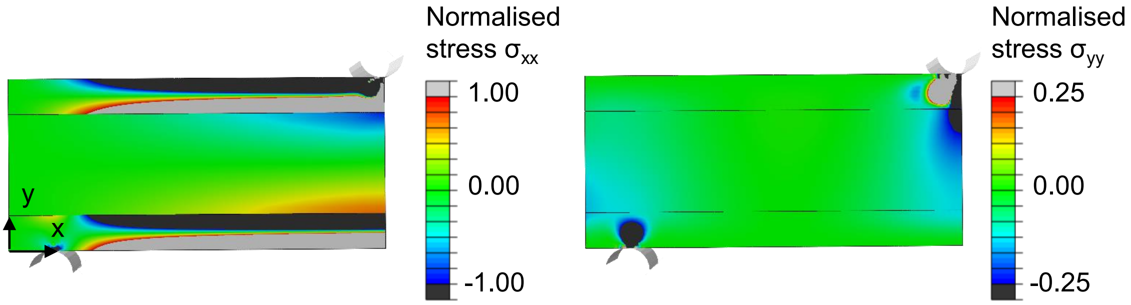

Figure 4.12: Normalised stress fields in the shear test setup. The steel beams induce pressure in the σ_{yy} component into the specimen.

Bi-axial Tension Experiment Bi-axial bending setups are quite common for brittle materials and especially ceramics and lead to the tensile strength of the specimen, since the fracture is induced on the tensile side. As shown in section 2.4.2 there are several manifestations of this test which can be differentiated by their boundary conditions (point-, line-, surface- contact). The usual ball-on-ring and ball-on-three balls experiments are difficult to evaluate accurately, since point contacts cause a high surface pressure and thus form grooves in the specimens surface. This is not a problem for hard materials like ceramics. However for core materials, it changes the stress state in the sample considerably compared to the theoretical constraints.

Therefore, I decided to utilise a pressure-on-ring concept, which has a line contact as support and a surface contact as load. This ensures that the surface of the specimen is not damaged and the theoretical boundary conditions are modelling the experimental reality more accurately. The test design is inspired by the Bulge experiment (Hill, 1950). A plate-shaped specimen is supported by a polymer ring with a diameter of 42 mm. The polymer of the ring is flexible enough to compensate the porous surface and small out-of-flatness deviations. A shaft bearing is placed on the top side of the specimen. The inner diameter of the bearing is equal to the diameter of the support ring. A water-filled polymer pad is placed inside the bearing. The load of the universal testing machine is applied to this water pad through a piece of shaft, whose diameter is chosen according to the inner diameter of the bearing. The water-filled pad distributes the hydrostatic pressure in the water evenly to the surface of the specimen. The test setup is shown in figure 4.13.

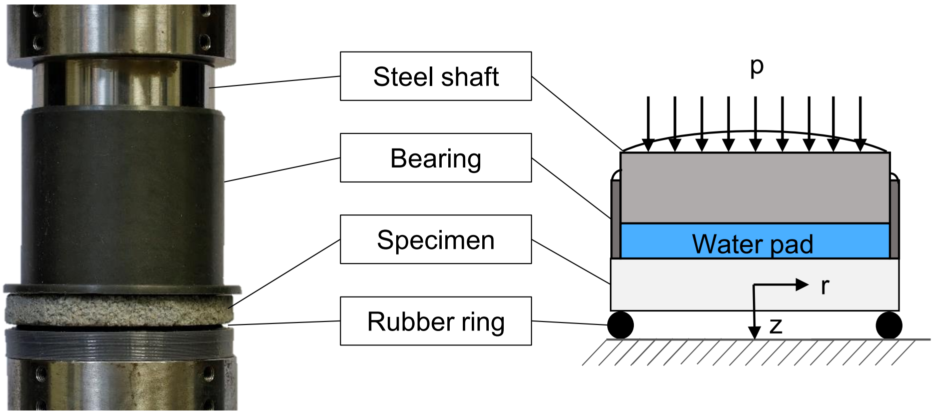

Figure 4.13: Bi-axial bending test setup. A circular disc specimen is placed on a rubber ring and loaded with a surface pressure through a water-filled pad. The resulting bi-axial stresses can be calculated with plate theory. (Lechner, Hartmann et al., 2021)

The bi-axial stress state in the disc can be described with (Hake and Meskouris, 2007, p.107):

$$\sigma_r(r,z) = \frac{3pR^2}{4}\,(3+\nu)\left(1-\frac{r^2}{R^2}\right)\frac{z}{h^3}, \tag{4.3}$$

$$\sigma_\phi(r,z) = \frac{3pR^2}{4}\left[2\,(1-\nu)+(1+3\nu)\left(1-\frac{r^2}{R^2}\right)\right]\frac{z}{h^3}, \tag{4.4}$$

where σ_r and σ_ϕ are the radial and the tangential stresses, respectively. p is the applied pressure, R and h are the radius and the height of the specimen. ν is the Poisson ratio. r and z are the two variables, which describe the location on the specimen (radius and distance from the neutral plane). Due to the small height of the specimen compared to its radius, I assume that shear stresses (in-plane and out-of-plane) are negligible. Thus σ_r and σ_ϕ are equal to the principal stresses σ_1 and σ_2. This assumption will be checked in the discussion. The bi-axial normalised stress field for this test setup is shown in figure 4.14. On the left-hand side, the normalised maximum principal stress field, which is calculated with an FEM simulation, is depicted, while the right hand side shows the stresses in polar coordinates, which are calculated with equations 4.3 and 4.4.

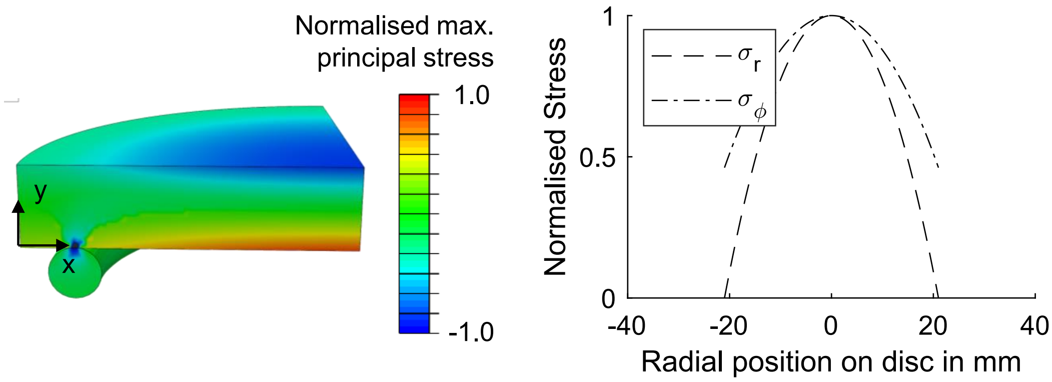

Figure 4.14: Stress field induced by the bi-axial bending test setup (left) and calculated stresses in polar coordinates (right).

4.2.5 Tri-axial Testing

Tri-axial testing methods allow to quantify the influence of the first invariant of the stress tensor on the failure surface. As shown in the state of the art, the strength of inorganically-bound core materials have not been evaluated under hydrostatic pressure before. Furthermore, no test setup is published, which is able to perform a bending experiment under hydrostatic pressure.

Figure 4.15 shows with the Mohr-Coulomb failure criterion as an example which parts of a failure surface can be determined by a hydrostatic compression and a hydrostatic bending experiment. The uni-axial bending and compression experiments are marked with a diamond and a square symbol. The corresponding experiments under hydrostatic pressure are depicted with a dashed and a dotted line, respectively. The Mohr-Coulomb criterion is defined by six intersecting faces. The six edges are defined by the friction angle of the model, which can be quantified with these experiments. Analogously, this test setup can be utilised to quantify the friction angle of other failure criteria which include an influence of the first stress invariant on the failure surface for compression and bending stress states. In contrast to bi-axial experiments the fraction angle can be determined directly with one type of experiment.

A testing machine developed in this dissertation aims to provide these results. In contrast to the test setups in previous sections, it is not an add-on to an existing universal testing machine, but is a stand-alone solution.

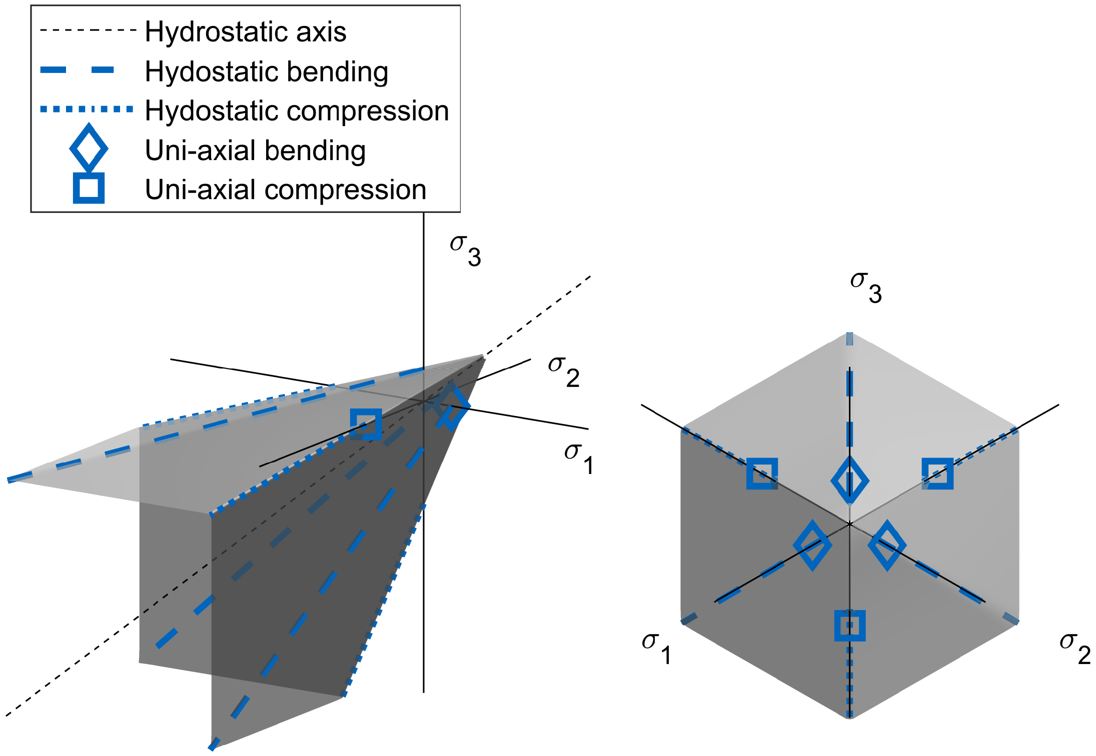

Figure 4.15: Possible stress states of the hydrostatic experiments. A Mohr-Coulomb criterion serves as an example. All intersecting faces of the criterion can be determined by hydrostatic compression and bending experiments.

A customised piston accumulator builds the basis of the testing machine. A piston accumulator consists of a tube which is divided by a movable piston. This piston divides the tube into two chambers with variable volume. In one chamber is a pressurised nitrogen atmosphere, in the other hydraulic oil. The nitrogen chamber can be filled to the intended pressure from a gas bottle. The hydraulic oil chamber is connected to a hydraulic unit, which can change the amount of oil in the chamber. This moves the piston and changes indirectly the pressure on the gas side. The pressure on both sides of the piston can be assumed approximately equal, if the friction of the piston sealing is neglected. A scheme of the test setup is shown in figure 4.16

Usually, the piston accumulator is utilised as a hydraulic shock absorber, which damps sudden changes of the pressure in the hydraulic system. With this intended purpose, it is not necessary to open the gas side of the accumulator except for maintenance of the sealing.

The concept for the test bench is to bring the specimen into the gas-side of the piston accumulator and to raise the nitrogen pressure by adding oil to the hydraulic side which moves the piston. The specimen has to be sealed by a polymer foil, since core materials are open-porous and the hydrostatic pressure of the nitrogen has to induce stresses into the surface of the specimen.

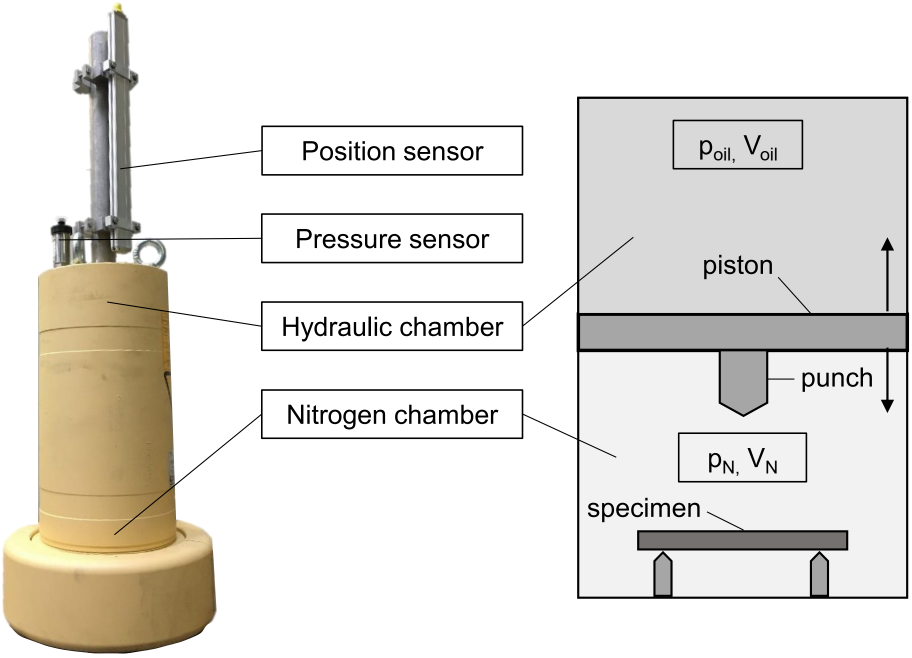

Figure 4.16: The hydrostatic pressure test bench. This test bench has two chambers, which are separated by a moving piston. In the upper chamber is hydraulic oil, while the lower chamber is filled with nitrogen. If the piston is pushed downwards by adding oil to the upper chamber, the pressure in the nitrogen atmosphere is increasing. In the nitrogen chamber, bending and compression tests can be performed.

Without the polymer foil the pressurised atmosphere would leak into the porous micro-structure of the core materials.

The specimen rests on a test specific support structure. For a uni-axial compression test, this is a plane horizontal surface. For a three-point-bending experiment, the specimen rests on two parallel supports with a distance of 138 mm, analogously to the three-point-bending test setup in section 2.4.1. The punch of both experiments is attached to the moving piston of the accumulator. It is equipped with a force sensor S20S from Bosche GmbH & Co. KG (Damme, Germany) with approximately 5 kN maximum force.

After placing the specimen on its support, the gas side is closed and the hydraulic unit starts adding oil, which moves the piston with the attached punch towards the specimen. The rising pressure is measured by a pressure sensor on the gas side of the moving piston. While the punch is in contact with the specimen, the force signal is analysed for the typical signs of the brittle fracture of the specimen, which concludes the tests. Additionally, the test bench is equipped with a position sensor which records the position of the piston. All signals are acquired with the same system to synchronise the force, the pressure and the position signals for evaluation.

After the test is concluded, the piston is moved back to its maximum height, the gas side of the accumulator is depressurised, it is opened and the specimen is removed.

The maximum pressure in the piston is 220 bar. This pressure is not achieved when the test starts with room pressure on the gas side. Therefore, a valve is integrated, which allows to pressurise the gas side of the accumulator from a gas bottle to the necessary pressure. The moving piston has two functions, it compresses the nitrogen on the gas side and it drives the punch onto the specimen. This leads to a rising pressure starting at the first contact to the specimen to material failure, since the specimen deforms and the piston moves slightly. However, the deflection of the specimens at the point of fracture is comparatively small (<0.3 mm), which allows to neglect this, since the change in volume and pressure is <0.5 %.

4.2.6 Validation Tests

In this work, a material model for core materials will be developed. To validate this material model, several experiments are necessary, which induce complex stress states into a specimen and can be simulated accurately. FEM calculations are utilised to predict the fracture forces, based on the material model, the core geometry and the load case. If the predicted fracture forces are close to the experimentally obtained ones, this indicates that the material model is valid for complex stress states, as well.

Brazilian Test The original Brazilian test loads the lateral cylindrical surface between two parallel plates. The contact between the two plates and the cylindrical lateral surface are line contacts, as shown in the state of the art in figure 2.10. I rejected the Brazilian test as a uni-axial characterisation experiment due to the complex stress state in the specimen. However, it offers the chance to test material models for these multi-axial stress states in a FEM simulation as a validation experiment. Preliminary experiments have shown, that the surface pressure is higher than the local material strength, because of the line contact, which distributes the testing force over a very small area (in theory just a line). This high pressure breaks individual grains from the specimen and flattens the curvature of the cylinder. Furthermore, the line contact is smaller than the RVE proposed by Schneider et al., which has 1.28 mm edge length. Therefore the assumptions of a mechanical continuum are no longer valid near the load points. This leads to the problem that the area of contact with the active elements of the testing machine cannot be precisely modelled over the course of the experiment, since it starts out as a line contact and ends with a bigger contact area. The contact area is a very important parameter, as it determines the fracture force to a high degree. Therefore, I adapted the test setup for the Brazilian test to control the area of contact better. The test setup is shown in figure 4.17.

Instead of the steel plates, a polymer element is in contact with the specimen. It has a width of 5 mm and a groove with the same radius as the cylindrical specimen. The polymer element

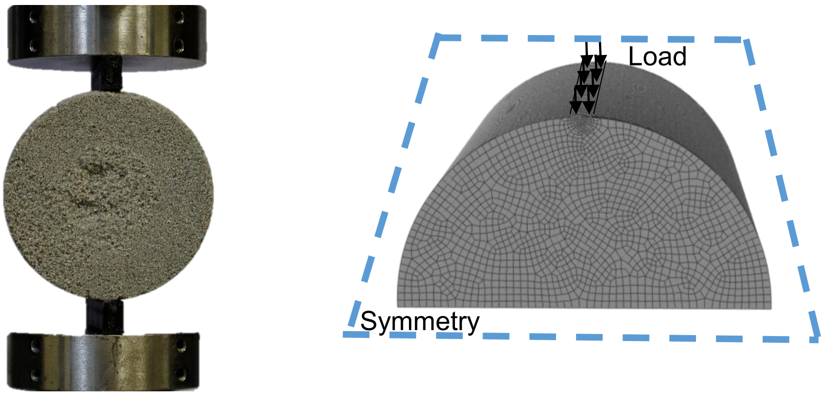

Figure 4.17: The Brazilian test setup. To accurately describe the contact surface the Brazilian test was adapted with polymer supports with a circular contact surface (left). This load was modelled with a surface pressure in a symmetrical FEM model (right).

limits the contact area. This way, the testing force is distributed over a constant area from the beginning until the end of the test, similar to one of the Brazilian test setups mentioned by Li and Wong (Li and Wong, 2013). The flexibility of the polymer material, ensures a constant and smooth stress field in the contact area. This test setup has been published in a previous article (Lechner, Hartmann et al., 2021).

Test of Water-jacket Core A second validation experiment has been performed on a water jacket core geometry (shown in figure 4.2). While the Brazilian test introduces complex stress states, the specimen's geometry itself is quite simplistic. The aim of the validation experiments with a water jacket core is to show that the prediction of fracture forces are possible even with complex core geometries.

The water jacket core is placed upon a steel plate as support. It is loaded in three individual points, which will be shown in detail in section 4.3.7. Again, a polymer pad is placed between the steel support and the core to ensure a smooth stress field in the contact area. The force on the specimen is raised until fracture occurs. The maximum in the force-deflection curve acquired by the testing machine is considered the fracture force. All three load cases will be simulated with FEM and the predicted fracture force can be compared to the experimentally obtained pendant to further validate the material model of the simulation and to show that such simulations are possible with real industrial core geometries. (Lechner, Stahl, Hartmann et al., 2021)

4.2.7 Creep Characterisation

Besides the classical failure criterion, I will study the creep behaviour of core materials, as well. These experiments are performed with the three-point-bending test setup, shown in figure 4.8. In contrast to the other experiments on the Zwick Z020 testing machine, the data will be acquired with a 500 N force sensor to achieve a better accuracy for load forces below 100 N. The test procedure is best explained with figure 4.18, which shows the punch displacement over the test time. The test includes a preconditioning phase, in which the force is increased to the specified level, held for 2 s and then reduced again to zero. Subsequently, the load force is raised to the target level and kept constant for the remaining test time. The line contacts between the specimen and the supports are smaller than the edge length of the RVE proposed by Schneider et al. (Schneider et al., 2018). Therefore, the specimen does not behave like an ideal continuum in the contact area. The preconditioning is utilised to flatten small sand particles which are located on the surface in the areas of contact to the support and the punch. While the load force is returned to zero after the first time the target load is reached, the displacement is not and about 0.05 mm displacement remain. Subsequently, the force is raised again and the creep data is acquired. In the following, I utilise only the displacement, which occurs in this time span. The elastic and inelastic displacement during the preconditioning are cut off and the displacement signal starts at zero. From the displacement signal, the strain signal is calculated with the following equation (Chuang, 1986):

$$\epsilon = \frac{2(n+2)h\Delta}{a^2}, \tag{4.5}$$

where n is the stress exponent in the Norton-Bailey creep law, Δ the displacement in the load point, a the support distance in the bending experiment and h the height of the beam. The strain rate is calculated by numerically differentiating the strain signal. In order to reduce the noise, which results from the numerical differentiation, I apply a Savitzky-Golay filter to the strain signal before it is processed further.

Please note, that I have utilised this test procedure on a steel beam with comparable loads. There was no creep behaviour detected, which ensures, that the creep, which is determined in this dissertation, is located in the specimens and not in the test setup itself.

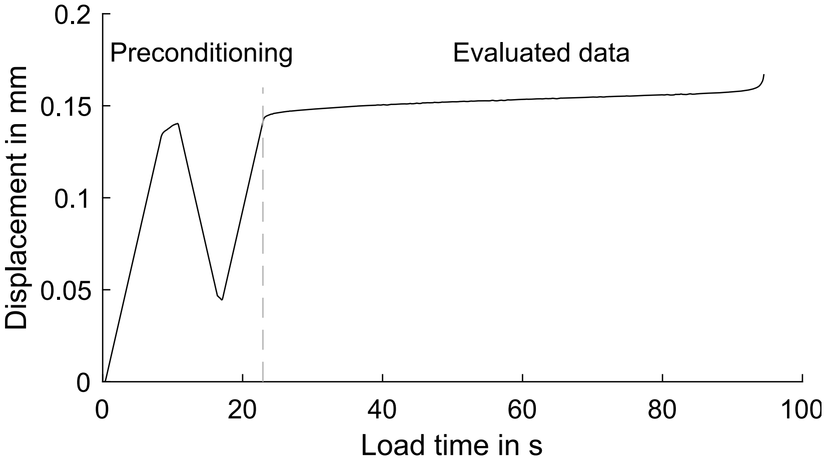

Figure 4.18: Test procedure of bending creep experiments. The test starts with a preconditioning. This includes raising the load force to the target load for 2 s and subsequently reducing the load to zero.

4.3 FEM Simulation Models

In this section, I will detail the simulation models, which are utilised to evaluate, refine and validate the experimental test results in chapters 5 and 6. Please note that the simulations in chapter 8 (Application in an Industrial Environment) are detailed in the chapter itself to build a complete showcase. All FEM simulations in this thesis are performed with the software Abaqus 2018. For all simulations, the core material is parameterised according to the following elastic experiments with a Young's modulus of 5.8 GPa and a Poisson ratio of 0.24, according to the results presented in chapter 5 for the sand-binder system IN-1-1.

4.3.1 Impulse Excitation

The impulse excitation test setup determines the frequency peaks, as detailed in section 4.2.1. In order to calculate the material parameters based on multiple peaks, the influence of the material parameters on the eigenfrequencies of the specimen have to be known.

The specimen was modelled as accurately as possible including minor production inaccuracies like the imprint of the shooting nozzle on the font side of the specimen. The dimensions and the density of the specimen are assumed constant. The model is shown in figure 4.19. It is meshed with tetrahedron elements of type C3D10 (Dassault Systems, 2020) with an approximate global size of 2 mm. The calculation of the eigenfrequencies was performed with a Lanczos solver. Please note that due to the imprint of the shooting nozzle on the front side, all flexural eigenmodes are divided in two very close neighbours. For reasons of simplicity, only the first eigenmode of each pair will be utilised in this evaluation, since the second peak does not carry significant additional information.

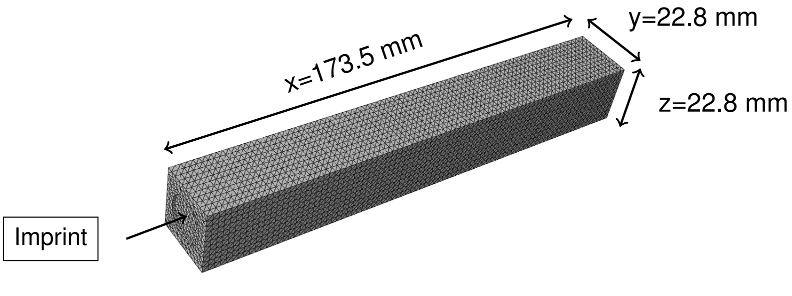

Figure 4.19: Mesh for the FEM calculation of the eigenfrequencies and eigenmodes of the beam specimen. The imprint is due to the core shooting nozzles.

4.3.2 Uni-axial Bending Experiment

FEM models of a three-point-bending and a four-point-bending test setup have been created for a precise elastic analysis of stress fields in the bending test setups in this thesis. These models will be utilised to investigate differences in the stress field compared to Bernoulli's beam theory. A quarter of the beam was modelled using both symmetries, as shown in Figure 4.20. The beam was modelled with cubic elements of type C3D8 (Dassault Systems, 2020) with the size 1.00 × 1.04 × 0.99 mm^3, while the support and load tools were modelled with analytic rigid bodies according to the dimensions of the real test setup.

4.3.3 Bi-axial Bending Experiment

The FEM model of the bi-axial bending test setup consists of a circular disc with a height of 6.3 mm and a radius of 45 mm. The disc is placed on a torus with a big diameter of 42 mm and a small diameter of 4 mm. Both parts are modelled with two symmetries, as shown in figure 4.20. The contact between the torus (dark grey) and the disk (light grey) is a hard contact in normal direction and frictionless in tangential direction. The load is applied as a pressure, while the lower half of the torus is fixed in all directions with a boundary condition. The geometry is meshed with C3D20R elements (Dassault Systems, 2020) with 0.5 mm seed distance for both parts. The rubber ring was parameterised with a Young's modulus of 10 GPa and a Poisson ratio of 0.5, which are typical material parameters for rubber (Koblar and Boltežar, 2013).

4.3.4 Compression Experiments

The simulation model for the uni-axial compression test is build with three symmetries, as shown in figure 4.20. The model consists of a cuboid (light grey) with one eighth of the specimens volume (three symmetries) and a rubber pad (dark grey) of 1 mm thickness. Again, the rubber is parameterised with a Young's modulus of 10 GPa and a Poisson's ratio of 0.5 (Koblar and Boltežar, 2013). The contact between the rubber pad and the core materials is considered hard in normal direction and frictionless in tangential direction. Both parts are meshed with C3D8R elements (Dassault Systems, 2020). The seed distance is 0.2 mm for the rubber pad and 0.3 mm for the core material. The load is applied as a surface pressure to the rubber pad. Due to the three symmetries, no further boundary conditions are necessary.

The bi-axial compression test simulation is build analogously to the uni-axial compression simulation. Additionally, a second rubber pad is added to induce another stress component.

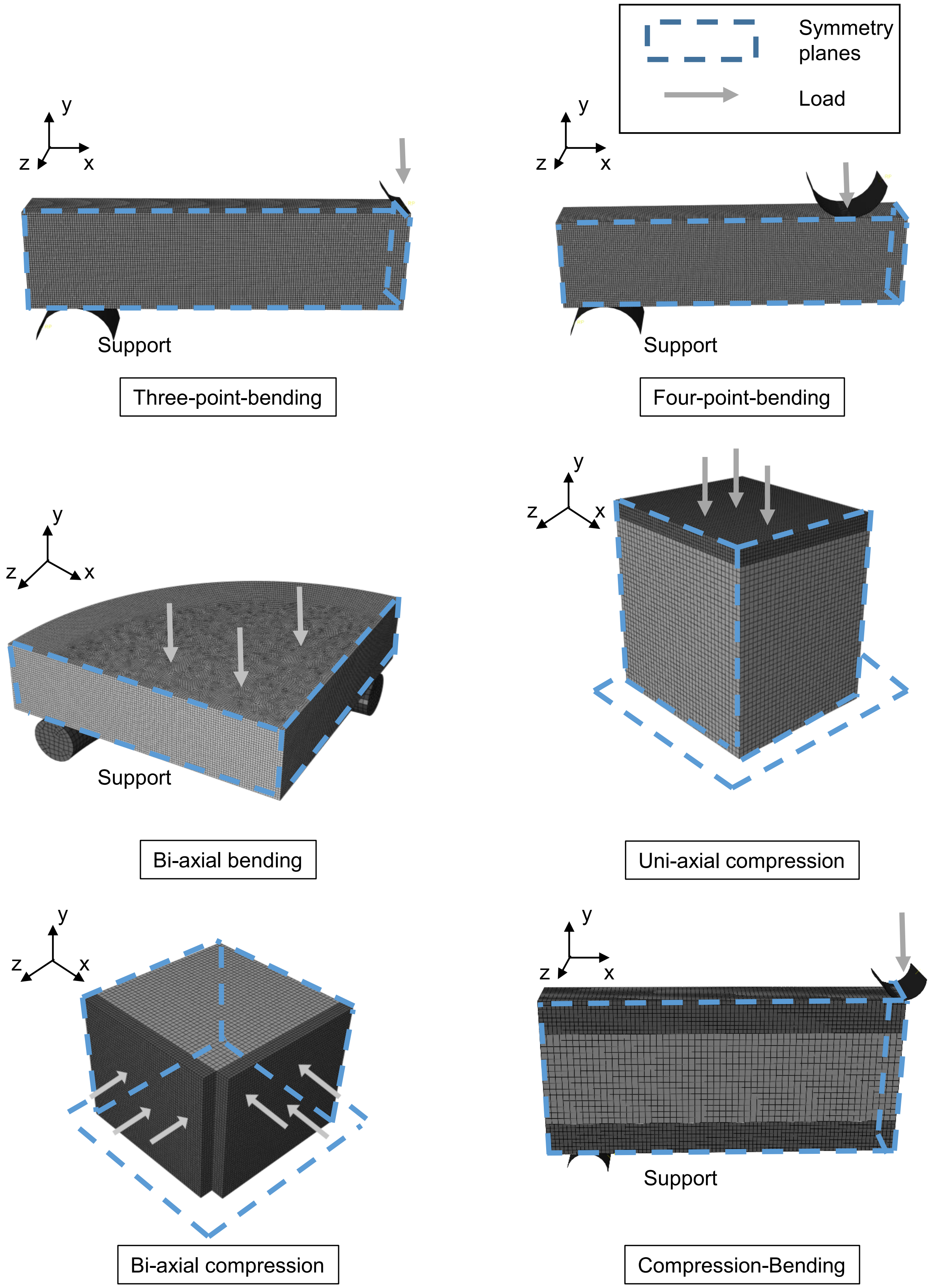

Figure 4.20: FEM models of the utilised testing setups. The grey arrows indicate load, while blue rectangles indicate a symmetry plane.

Furthermore, the contact between the rubber pads and the core material is no longer frictionless in tangential direction: A penalty friction concept with a friction coefficient of 0.5 is necessary, because of the bi-axial stress state. The tangential friction shows which influence the deformation of the specimen has on the stress state. Furthermore, it is necessary for numerical stability. The model is shown in figure 4.20, as well.

4.3.5 Shear Experiment

The compression-bending test setup, which induces shear stress into the specimen is simulated with two symmetries, analogously to the three-point-bending model. It consists of three beams, which build a sandwich structure as described in section 4.2.4. The contact between the steel beams and the core material is modelled as a hard contact in normal direction and with penalty friction (coefficient is 0.3) in tangential direction. The tangential friction coefficient was chosen for numerical stability. The support and the load are modelled as analytical rigid bodies analogously to the real test setup. The contacts of the analytical rigid bodies to the steel beams are hard and frictionless. The model is depicted in figure 4.20. The steel beams in dark grey are meshed with C3D20 elements (Dassault Systems, 2020) and 1 mm seed distance, while the core material in light grey is modelled with C3D8R elements (Dassault Systems, 2020) and 1.5 mm seed distance. The hard line contact between the steel beams and the rigid bodies make quadratic elements with full integration necessary.

4.3.6 Brazilian Experiment

The Brazilian test is utilised for a first validation of the material models developed in this thesis. To calculate the stress field in the cylindrical specimen (diameter: 50 mm, length: 50 mm) of the Brazilian test, a FEM simulation will be performed. Only half of the cylindrical specimen is modelled to utilise the symmetry of the test setup. The load is induced via a constant surface pressure. It is located where the polymer tools in the experiment touch the specimen on opposing sides of the specimen. The section, which is in contact with the specimen, has a chord length of 5 mm. The two symmetric loads are in an equilibrium which makes no further support necessary. The specimen was modelled with cubic elements of type C3D20R (Dassault Systems, 2020) with approximately 2 mm edge length, while the mesh in the vicinity of the load surfaces was refined to 0.5 mm edge length. The model is shown in figure 4.17. The simulation is purely elastic, the Young's modulus and the Poisson ratio will be chosen according to the experiments performed with the impulse excitation setup. The stress field is exported to Matlab, where it is evaluated according to the failure models, which are to be validated.

4.3.7 Water-Jacket Core Experiment

To further validate the developed material models, a FEM simulation of the water jacket core will be performed. The water jacket core is chosen, since it is a highly complex geometry with high industrial relevance and shows the applicability of this work to industrial practice. There are three different load cases, which are shown in figure 4.21. All of these load cases are simulated with FEM and performed as an experiment on a universal testing machine. The results are compared to validate the material model of the FEM calculation. The water jacket core is placed on a steel plate in the experimental test setup. At three different geometrical points it is loaded with a vertical force and the load is increased until a fracture occurs. The FEM simulation calculates the complex stresses in the geometry in an elastic simulation. The geometry is meshed with elements of type C3D10M (Dassault Systems, 2020) with a seed distance of 3.5 mm. In areas with increased stresses, the mesh is refined with a seed distance of 0.3 mm. A detailed view of the mesh in the vicinity of the load points is shown in figure 4.21 on the right side. The steel plate is modelled as an analytic rigid plate with a frictionless tangential contact to the water jacket core. In the normal direction the interface between the plate and the core is modelled as a hard contact. A dynamic explicit solver without time or mass scaling is utilised to solve the problem, due to the contact between the core and the plate. The force is increased linearly. The principal stress values and the volume of each element is exported after the simulation and evaluated for fracture according to the material models in Matlab.

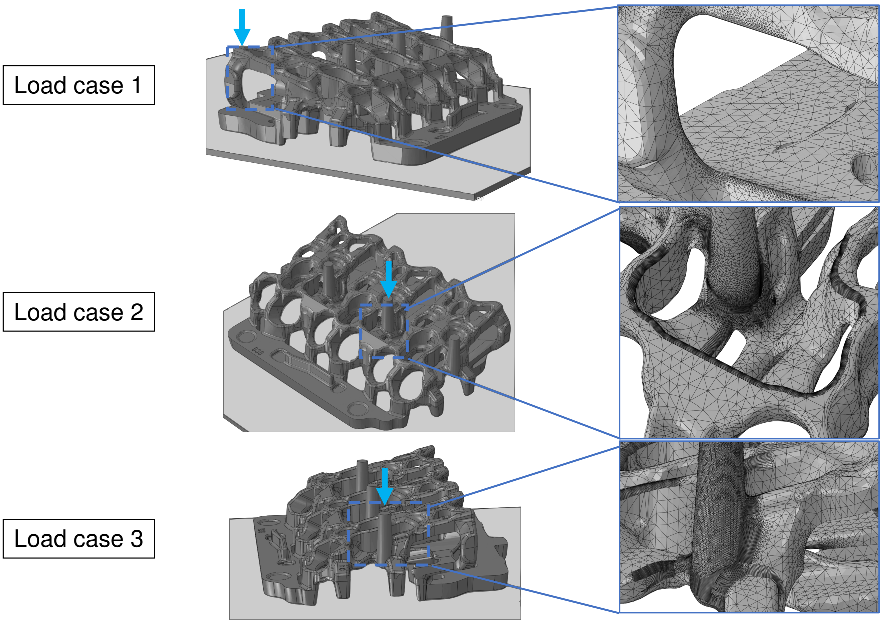

Figure 4.21: Load cases of the water jacket core. The core is standing on a plate and is subjected to a vertical force by the testing machine.

5 Elastic Behaviour

In this chapter, I will utilise the test bench and test procedure described in 4.2.1 to characterise the elastic behaviour of core materials. The focus for all successive experimental chapters will lie on inorganic sand-binder systems. However, I will compare important results to organic binder systems as well to show where similarities and differences have to be considered when modelling organic sand-binder systems. For inorganic sand-binder systems, there are several important factors, which influence the mechanical behaviour considerably. I will analyse the influence of the time span after the core shooting, the binder amount, the relative air humidity and the moisture in the core on the mechanical properties for the IN-1-1 binder system as an example how sand-binder systems can be characterised.

5.1 Influence of Binder Amount

I have determined the elastic parameters for three amounts of binder and for two points in time after the core shooting (10 s and 24 h). These two points in time can be considered as a lower and an upper boundary of the technically relevant hardening process of the cores. Immediately after the opening of the core box is the first time that the mechanical properties matter regarding handling operations. In the first seconds, the gradient of the mechanical properties is considered highest. Subsequently, this reaction is slowing down and is approximately complete after 24 h. Please note that in the following the index $24h$ stands for a time frame between 24 hours and 48 hours, in which the mechanical properties of inorganic core materials are very constant if the humidity is at 10 %. This assumption will be validated with the results in the chapters 5 and 6. The results are shown in figure 5.1, while the raw data can be found in tables D.1 and D.2. One standard deviation is added to each data point as an upper and lower boundary to quantify the scatter in the data. The number of specimens is given with N. As a general observation, it can be noted that the Young's modulus and the Poisson ratio are increasing with the amount of binder. Furthermore, the continuing condensation reaction leads to higher values after 24 hours (E_{24h}, ν_{24h}) than after 10 seconds (E_{10s}, ν_{10s}). E_{24h} is increasing approximately linear with the binder amount, while E_{10s} is saturating for 2.5 % liquid binder.

Discussion Schneider et al. modelled the elastic behaviour of inorganically-bound core materials with micro-structure simulations and one of the predictions was this near-linear increase of

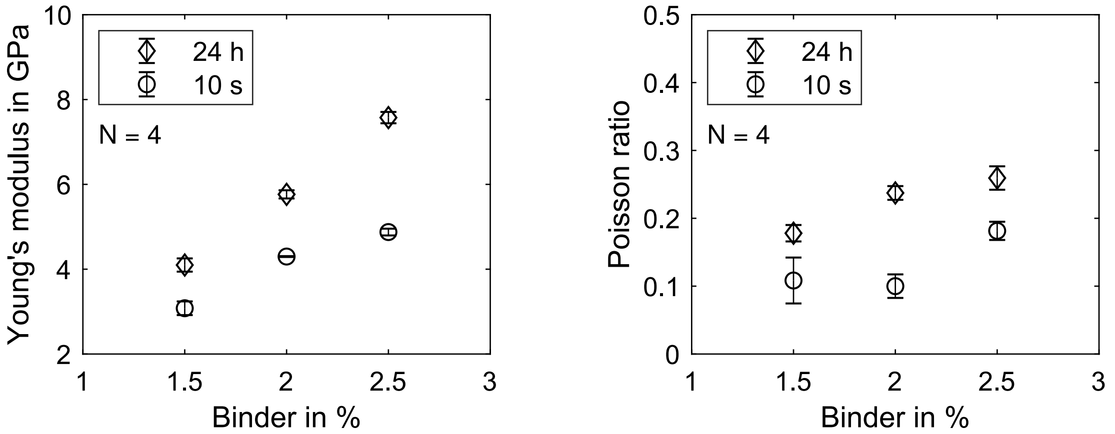

Figure 5.1: Young's Modulus and Poisson ratio for IOB core materials directly after the core shooting and after 24 h for varying amounts of binder. The error intervals show the standard deviation values in the data set. (Lechner, Stahl, Hartmann et al., 2021)

E_{24h} with micro-structure simulations, which could not be confirmed at the time (Schneider et al., 2018). In experimental literature, only the Young's modulus has been determined for core materials, while the shear modulus and the Poisson ratio have not been studied yet. Furthermore, it is difficult to compare the Young's modulus of different sand-binder systems, since it is highly influenced by production and environmental parameters. Griebel et al. determined the Young's modulus of a different type of inorganic core material to be approximately 7 GPa, which fits in the range of E_{24h} I obtained in these experiments. Furthermore, they found that the Young's modulus is dependent on the applied load. The Young's modulus determined at the fracture stress level is 20% lower than the one at the beginning of the load curve. (Griebel et al., 2016)

Therefore, the impulse excitation process was validated with a digital image correlation algorithm and high speed imaging in a previous publication (Lechner et al., 2020). The Young's modulus was determined at fracture to be approximately 20% lower than the one obtained acoustically without significant load, as well. Various materials including metals show this kind of behaviour, which has led to a tensile test procedure, which uses only the first part of the strain stress curve to determine the Young's modulus, where the load is comparatively low (Yoshida, 2018).

In this and other regards, acoustical determination of the elastic parameters has several advantages over tensile tests and other destructive experiments:

- The impulse necessary for the test procedure only applies a small load on the specimen.
- In contrast to tensile tests, one can obtain Young's and shear modulus with one specimen. In tensile tests, the Poisson ratio can be quantified for materials with high fracture strain

by measuring the transverse contraction. However, this is challenging for materials with low fracture strain.

- The experiment is non-destructive, which allows further experiments to be performed on the same specimen.

Considering the influence of the binder amount, it seems intuitive that the Young's modulus is increasing with more binder, since more binder bridges can be built. The rising Poisson ratio shows that the transversal contraction is increasing with the binder amount, as well. The Poisson ratio is calculated with equation 2.33, under assumption of isotropic material behaviour. Therefore, the rising Poisson ratio shows that the Young's modulus is increasing more than the shear modulus with the binder amount. The Young's modulus describes the material stiffness, which impedes extension and compression of the material (Hooke's law). The shear modulus describes the stiffness which impedes torsional strains or a change of the shear angle in general, according to:

$$\tau = G \tan \gamma, \tag{5.1}$$

where τ is the shear stress, G is the shear modulus and γ is the shear angle. I theorise that the extension and compression behaviour and therefore the Young's modulus is mainly determined by the number and size of the binder bridges between the sand grains. In contrast, angular strains change the orientation of the sand grains relative to each other. Such rotations are not only impeded by the binder bridges but also by the form of the sans grains themselves. Thus, the correlation of the Young's modulus to the amount of binder is stronger than the correlation to the shear modulus, since the form of the sand grains has a bigger influence, which does not change with the binder amount. This theory can be supported by the simple analogy of loose dry sand. Sand without binder or humidity has no tensile stiffness or strength, since no binder bridges impede the separation of the grains in that direction. However, loose dry sand does have a shear stiffness and a shear strength >0, which can be described by the angle of repose which is characteristic for bulk materials. Therefore, the grains are able to retain a certain shear stiffness without the influence of binder.

5.2 Influence of Storage Time

As a second step, the elastic parameters have been determined for two points in time, 10 s and 24 h after the tool opening. Figure 5.2 shows the results with a logarithmic time axis. The Young's modulus is increasing considerably in the time frame from 10 s to 24 h.

The Poisson ratio is increasing during the whole time as well, which shows that the shear modulus is less affected by the storage time than the Young's modulus.

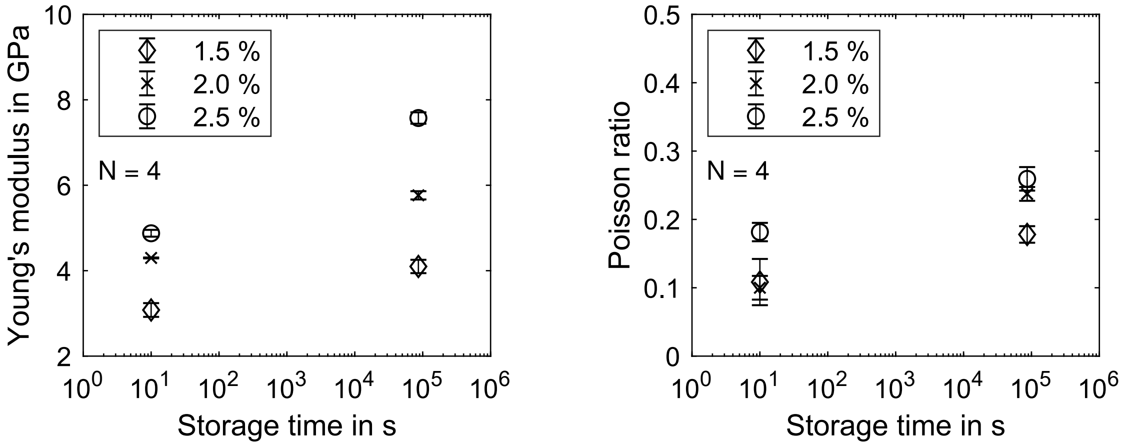

Figure 5.2: Young's Modulus E and Poisson ratio for core materials of sand-binder system IN-1-2 and varying storage times.

Discussion Analogous to the section before, I argue that the binder hardening is affecting the Young's modulus more than the shear modulus, since the binder bridges provide the only support for tensile strains, while shear strains can be supported by the contacts between the sand grains, as well.

5.3 Influence of Humidity

To test the influence of the ambient humidity, I stored a set of specimen in a climate chamber at varying humidity levels at 20 °C. The specimens were exposed to each humidity level for at least 24 h to allow the binder in the specimens to absorb the humidity and reach a constant humidity level. At the same time, cuboid shaped specimens were exposed to the same humidity levels. These specimens were used to determine the amount of water in the core materials themselves with a Moisture analyser DBS from Kern. The specimens are ground and heated to 250 °C for 15 min, while the weight is constantly determined. The evaporating water can be determined with the weight difference from the beginning to the end.

Figure 5.3 shows the results. The increase in relative humidity from 10 % to 40 % has little effect on the moisture in the core and on the elastic parameters. However, the step to 60 % increases the moisture considerably and decreases the Young's modulus E from 6.0 GPa to 3.1 GPa. Due to the high damping of the material at 60 % humidity, no Poisson ratio could be determined.

These results show that the moisture in the cores does not increase linearly with the ambient humidity. Furthermore, the Young's modulus can be considered constant below 40 % humidity, while there is a significant decrease over 40 % humidity.

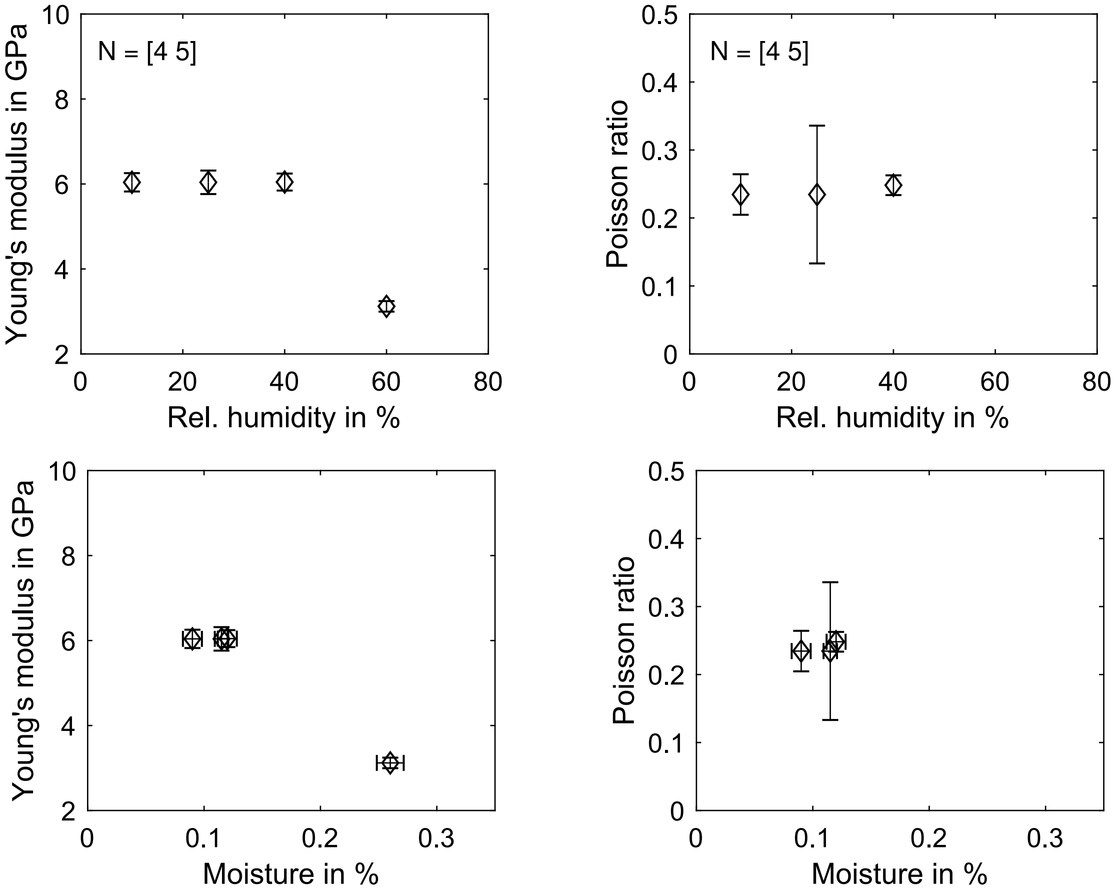

Figure 5.3: Young's Modulus and Poisson ratio for inorganically-bound core materials at varying relative ambient humidity (top). The moisture in the specimens, owing to the humidity, was measured, as well (bottom).

Discussion It is especially advantageous for these experiments that the elastic constants can be determined non-destructively, since the same specimens can be utilised at multiple humidity levels, which leads to a clear conclusion on the effect of humidity with a comparatively low number of specimens. The state of the art does not provide a study of the elastic parameters of inorganic core materials for varying humidity and moisture, yet. From an industrial point of view, it is advantageous that the moisture and the elastic parameters are fairly constant up to 40 %. With this information the climate in the storage facility of the cores can be monitored and therefore the mechanical properties of the cores estimated.

5.4 Comparison to Organic Binder Systems

I compared the Young's modulus of two inorganic sand-binder systems IN-1-1 and IN-2 with three organic systems in figure 5.4. On the left side, the absolute values of the Young's modulus are shown. The inorganic binder systems lead to a significantly higher Young's modulus than the three organic binder systems. The section before showed that the Young's modulus is influenced by the binder amount utilised in the sand-binder system. Usually, the binder amount is chosen with respect to the necessary material strength. Therefore, I compare the same sand-binder systems on the right side of figure 5.4 by normalising the Young's modulus with the three-point-bending strength of the materials. Again, the inorganic binder systems lead to a significantly higher Young's modulus per strength than the organic binder systems.

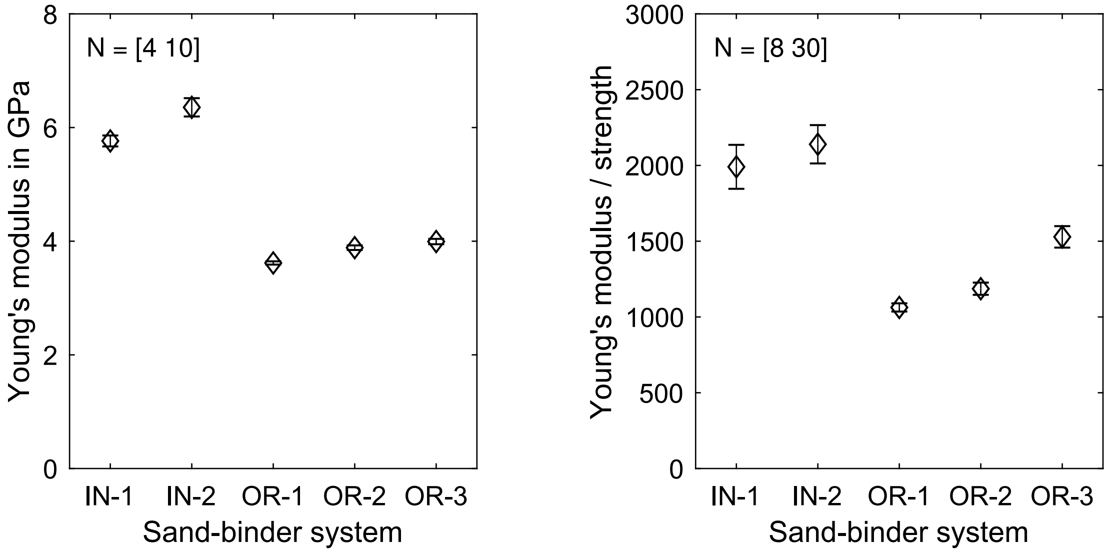

Figure 5.4: Young's modulus of inorganic and organic sand-binder systems. The influence of the binder system on the Young's modulus of the compound is shown on the left side. A comparison of the Young's modulus normalised with the strength is shown on the ride side.

Discussion It is interesting to note that all three organic sand-binder systems utilise a H32 sand and the same amount of binder. While the absolute Young's modulus is nearly identical, the normalised values on the right differ significantly. Thus, the different binder systems lead to different three-point-bending strength values, while the Young's modulus is very similar. Stauder et al. studied the Young's modulus of several organic sand-binder systems, which resulted in values between 1.7 GPa and 2.7 GPa (Stauder et al., 2016). However, he utilised the stress-strain data of a universal testing machine to determine the Young's modulus, which results in lower values, as Griebel et al. showed (Griebel et al., 2016).

6 Failure Characterisation

In this chapter, I will characterise the failure behaviour of core materials. It is structured in five sections. At first, I will study whether the failure of core materials is Gauss or Weibull distributed and asses the consequences which arise for inorganic and organic core materials from these fundamental fracture mechanical prerequisites. In the second section, I will characterise the failure surface with test setups with rising complexity. In the third section, I will parametrise the found failure surface with the necessary experiments and vary several important process and environmental parameters, which helps to understand their influence and shows how sand-binder systems can be characterised for industrial application in the future. The fourth section will study the creep behaviour of inorganically-bound core materials. The fifth section will discuss the results regarding industrial core production.

6.1 Fracture Statistics

In this section, I will analyse whether the failure of core materials follows a Gauss or a Weibull distribution. The following results have been published previously (Lechner et al., 2018). As shown in section 2.3, the mechanical behaviour of the sand-binder microstructure leads to a scatter in the macroscopic test data. This mechanical behaviour determines how the macroscopic strength data of specimens which are bigger than a RVE is distributed. In literature, the strength of core materials is typically determined with bending experiments. A mean value is given for a statistically significant number of specimens and if the scatter is quantified, the standard deviation is calculated for the data set at hand (Griebel et al., 2016; Stauder et al., 2016). Without further discussion, this implies that the data is Gauss-distributed. This assumption is plausible for organic core materials with their resin-based binder systems, since polymers usually have a ductile fracture behaviour. However, inorganic core materials are bound with silicates, which are closely related to quartz and glass, which are known to follow the weakest link theory and their fracture is therefore Weibull-distributed.

As a first step to classify the fracture of core materials, the sand-binder system IN-1 is analysed with SEM images. Figure 6.1 shows broken binder bridges of sand-binder system IN-1 with clear signs of a brittle fracture with sharp edges and smooth fracture surfaces in the area of the broken grains and binder bridges.

This kind of fracture indicates that the fracture of inorganic core material IN-1 is Weibull-distributed. To verify this assumption, data sets for several inorganic and organic core materials are analysed regarding their probabilistic distribution.

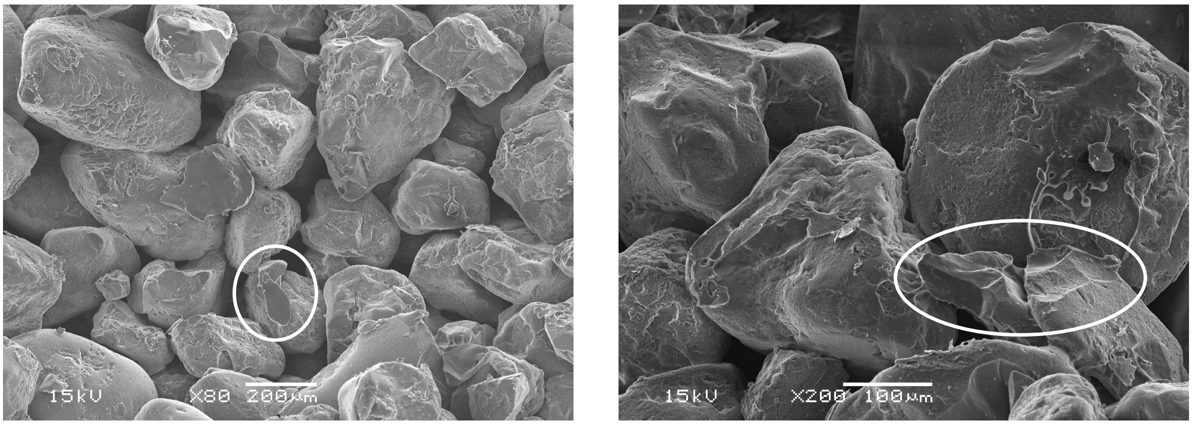

Figure 6.1: Overview of an inorganic sand-binder system with broken binder bridges (left) and grains (right) with signs of brittle failure.

6.1.1 Influence of the Sand-Binder System on the Probabilistic Distribution of Failure

In this section, I will analyse the statistical distribution of strength data sets of inorganic core materials (IN-1-2, IN-2) and organic core materials (OR-1, OR-2, OR-3).

To calculate the fracture probability corresponding with specific stress levels for a data set consisting of fracture stress results for n specimens, the results need to be sorted by stress value in ascending order. The probability P then can be calculated (Bennett, 1991):

$$P(\sigma_i) = \frac{i - 0.5}{n}, \tag{6.1}$$

where σ_i is the i-th value in the sorted data-set.

Figure 6.2 shows Weibull plots of inorganic sand-binder systems (IN-1-2 and IN-2) on the left and organic sand-binder systems (OR-1, OR-2, OR-3) on the right. The assumption is that inorganic sand-binder systems fracture based on the weakest link theory and therefore Weibull distributed, while organic binder systems fracture Gauss distributed, since the resin-based binder bridges are able to compensate small defects by plastic deformation. The data sets are plotted with logarithmic scales. Weibull distributed data sets are characterised by a straight line in this kind of plot, while Gauss distributed data sets build a curved line. I fitted a Weibull distribution to all data sets to test this hypothesis. The Weibull scale factor can be found in the plots at 63.2 % fracture probability. The scatter is represented by the slope of the line.

It appears as if the Weibull distribution fits for both systems. A Lilliefors can be utilised to discriminate between several probability distributions (MathWorks, 2016, p. 515). It was performed on the data sets to confirm this. For all binder systems, the hypothesis of a Gauss distribution was rejected before the hypothesis of a Weibull distribution was rejected. This is surprising, since the furan-based organic binder systems were expected to show a more ductile fracture. However, the scatter in the data is quite small, which makes it difficult to differentiate between Weibull and Gauss distribution. This will be revisited in the next section. In contrast to Gauss distributed fracture, Weibull distributed fracture is closely related to the weakest link theory. For materials which follow the weakest link theory, the material strength depends on the effective volume under load. This will be analysed in the next section.

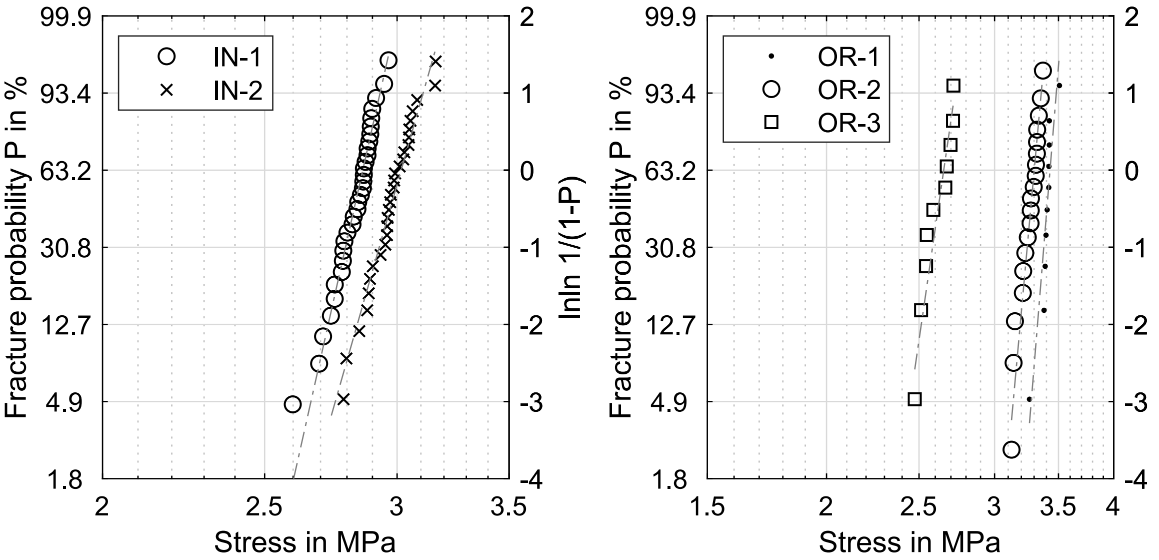

Figure 6.2: Analysis of the probabilistic distribution of fracture data for inorganic (left) and organic (right) binder systems. There are Weibull distributions fitted to the inorganic and a Gauss distribution to the organic binder systems. The scales are logarithmic.

6.1.2 Volume-Dependence of Core Materials

In this section, I study the volume dependence of the bending strength for the sand-binder systems IN-1-2 and OR-2. This is the final confirmation, if the weakest link theory applies.

Figure 6.3 shows the results of a three-point-bending and a four-point-bending experiment for each sand-binder system. I used the same support distance of 150 mm for both experiments.

The punch was varied from one contact in the middle (three-point-bending) to symmetrical contacts with a distance of 75.5 mm. This leads to a difference in the effective volume according to equation 2.5. The two inorganic data sets are clearly distinguishable, the fracture stresses σ (Weibull scale factor) are 2.68 MPa and 2.88 MPa. The scale factors for the specimens bound with the organic binder system are 2.90 MPa and 3.33 MPa. This is a significant difference for both binder types, considering that in industrial applications with complex cores the difference in effective volume will be higher than the difference between two bending experiments.

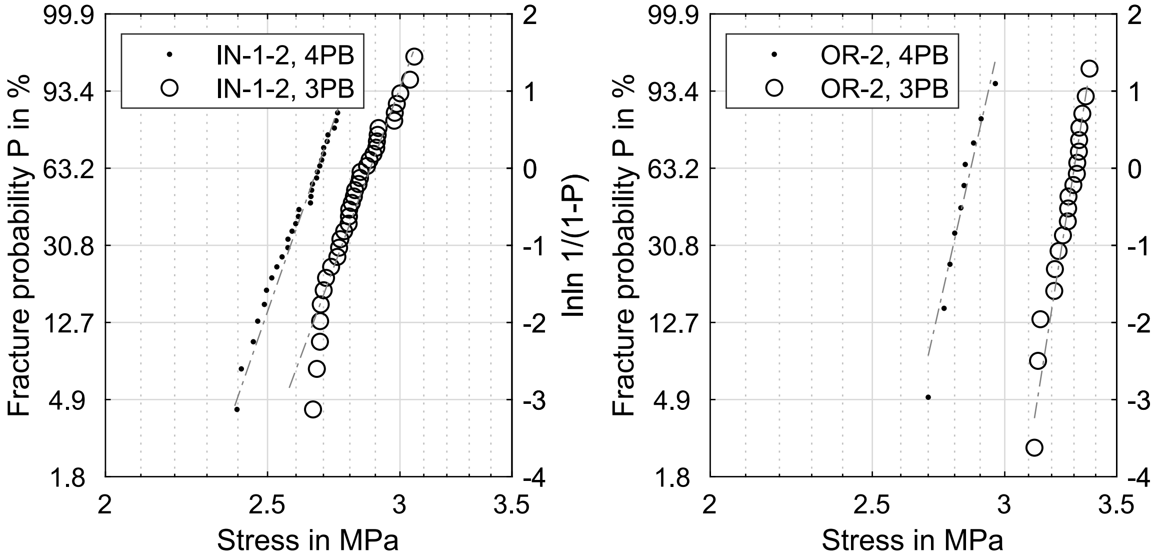

Figure 6.3: Comparison of the fracture probabilities of a three- and a four-point bending setup for an inorganic sand-binder system (left) and an organic sand-binder system (right). Both systems clearly differentiate the two load cases.

Discussion As shown in section 2.2, the different sizes, shapes and orientations of the grains and binder bridges lead to stress concentrations in the microstucture of core materials under load (Schneider et al., 2018). This suggests that this size effect results from the combination of the brittle fracture behaviour of the constituents (binder and grains) and these randomly distributed stress concentrations due to the complex microstructure. Therefore, a bigger volume is more likely to contain a critical stress concentration than a small volume. This is the final confirmation that the fracture of the tested organic and inorganic sand-binder systems follows the weakest link theory. In the following, I will show how this volume dependence can be handled for future application with the sand binder system IN-1-2.

6.1.3 Predicting Fracture Stresses for Arbitrary Bending Test Setups

The difference in effective volume can be calculated analytically with beam theory and equation 2.5, which integrates the stress field and normalises it with the maximum stress in the specimen. This way, each integrated volume cell is contributing an effective volume, weighted by its stress level. According to Weibull's theory, the fracture stress of arbitrary specimens and stress states can be calculated, if one experimental data set is known and both stress fields (input and target) can be calculated analytically. After integration of the effective volume V, the two volumes and fracture stresses σ_s follow (Danzer et al., 2007):

$$\frac{V_0}{V} = \left(\frac{\sigma}{\sigma_0}\right)^m, \tag{6.2}$$

with m being the Weibull shape parameter. Analogous to the effective volume in ceramics, I integrated only the volume cells with tensile stresses, since the compressive strength is significantly higher. Figures 6.4 a and b show the results of this prediction. The experimental data set, which is used as input for the prediction, which is based on equation 6.2, is depicted with dots, while the target data set is marked with circles.

The prediction of the target based on the input is shown with a black line. It is called analytic prediction, which will differentiate it from future numeric predictions based on a FEM simulation. The specimens are produced with sand-binder-system IN-1-2. Figure 6.4 a shows the results of a three-point-bending and a four-point-bending test with 75.5 mm distance between the load points. The experimentally obtained Weibull scale factor of the fracture stress is 2.88 MPa, while the analytic prediction is 2.96 MPa. Figure 6.4 b shows a prediction for the same three-point-bending data set based on a data set with 28.8 mm load distance. The prediction is 2.93 MPa, which fits significantly better to the target at hand. However, it is still overestimating the fracture stress by 0.05 MPa.

Discussion Both overestimating predictions have in common that they are based on the bigger effective volume (input) and are performed for the smaller effective volume (target). If the input and the target would switch, the predicted values would be underestimated. The effective volume of the four-point-bending test setup is increasing with its load distance. Theoretically, the smallest effective volume achievable is the one of the three-point-bending, if the two load points meet with a load distance of zero. In search for the reason for the overestimation of the fracture strength, two causes are possible: The modelling error results from the experimental results or from the post-processing of the data. Regarding the experimental data, it is possible that the stress fields of the two experiments are not perfectly consistent, since two different

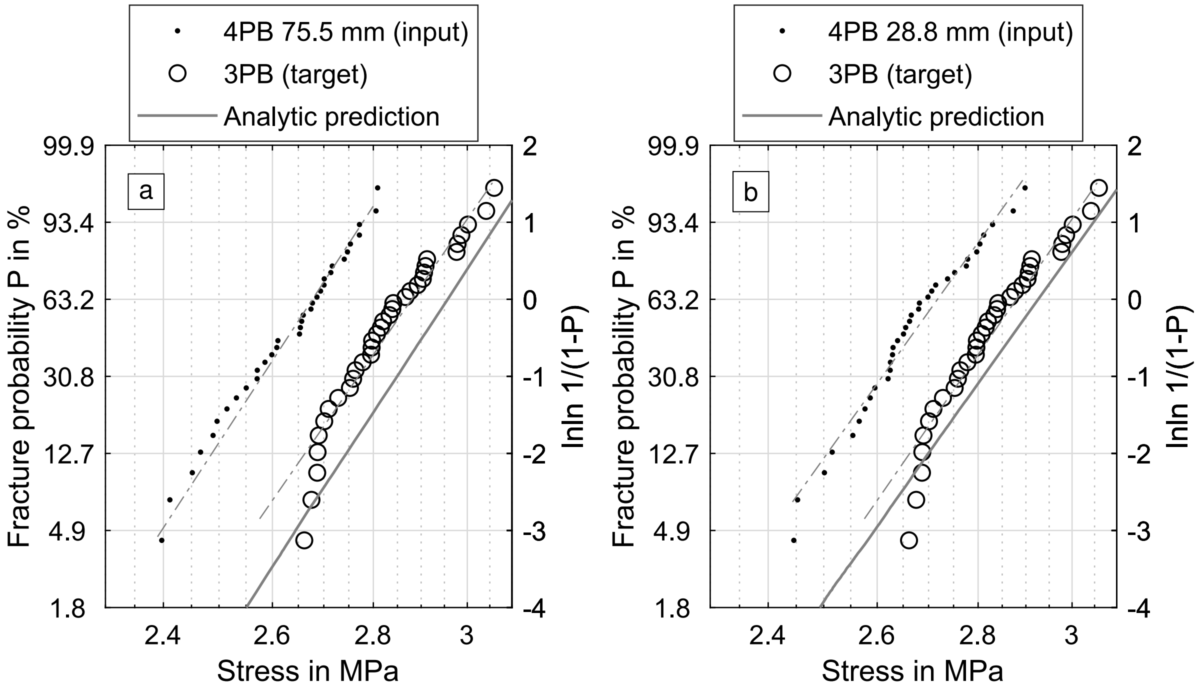

Figure 6.4: Prediction of fracture probabilities for arbitrary bending test setups, based on one data set. The plots show predictions and experimental results for a bending test setup with a specific effective volume (target) based on an input test setup and an analytic stress calculation.

test setups were used for the three-point and four-point experiments. Since the observed offset is smaller for the 28.8 mm than the 75.5 mm input, it is likely that the offset depends on the difference between effective volume of input and target data set. Intuitively, a smaller step in effective volume results in a smaller modelling error.

The post-processing of the data is the second option as the root cause for the modelling error. The stress field is calculated analytically with Bernoulli's beam theory with equations 2.25 and 2.26. Beam theory dictates that the stress curve along the beam is linear with sharp non-differentiable edges under the load points. However, literature shows that the real stress field is more complex than that - especially under the load points (Lamon, 1988). FEM simulations show that there are stress concentrations, which exceed the stress maxima calculated analytically with beam theory. The calculation of the effective volume is especially sensitive to changes in the stress maximum since it is utilised to normalise the stress state in all other volume cells. Therefore, a higher stress maximum leads to a smaller effective volume in the whole specimen.

Why is this effect not cancelling itself out, since it is included in both test setups? While these unmodelled stresses are indeed included in all experimental data, the effect on the prediction is not constant, since the proportion of unmodelled stresses is higher for smaller effective volumes (three-point-bending) than for bigger effective volumes (four-point-bending). In the following, the FEM models detailed in section 4.3 were utilised to compare the real stress field in the specimens to the analytically obtained stress field. This serves two purposes: The analytic prediction of the fracture stresses can be validated and maybe improved. Furthermore, it shows that the calculation of the effective volume of core materials can be performed numerically and is possible for complex geometries. Both test setups were simulated. The results for the three-point-bending and the four-point-bending (load distance 75.5 mm) are shown in figures 6.5 and 6.6.

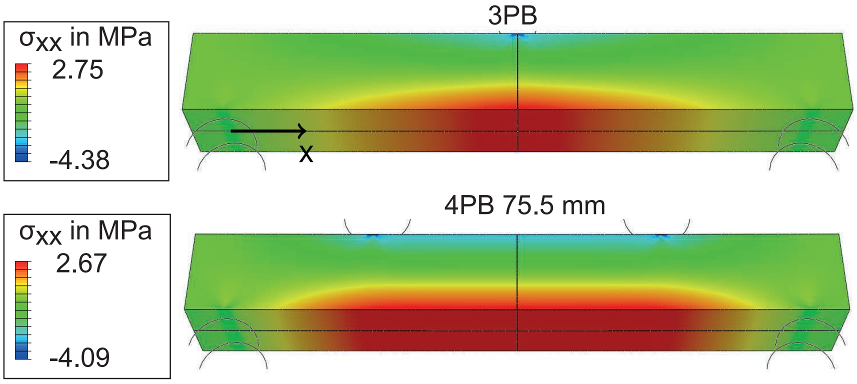

Figure 6.5: FEM results for the utilised bending setups: Three-point-bending and four-point-bending with 75.5 mm load distance. The effective volume of the test setups can be calculated with stress in x*-direction.*

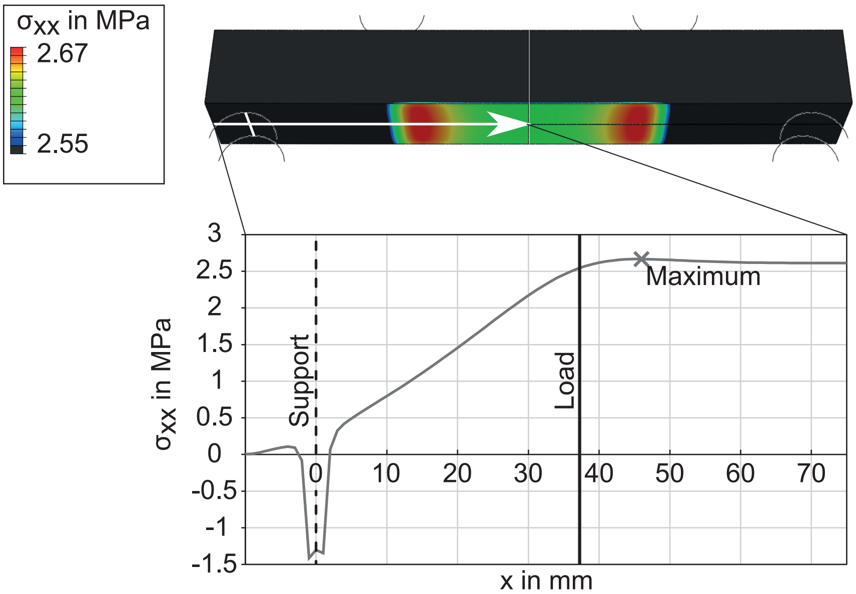

Figure 6.6: The FEM results of the four-point-bending setup with a refined scale to show the stress peaks in the vicinity of the load points, which can not be modelled with Bernoulli's beam theory.

Beam theory dictates a constant moment between the load points of the four-point-bending test setup, which translates to a constant stress in x-direction. In contrast to theory, the FEM results show that there are local stress concentrations in the vicinity of the load points which are the global stress maxima. These maxima are located 8.75 mm from the load points for the 75.5 mm test setup, as shown in figure 6.6. To validate these numerical results, the fracture location of ten specimens has been analysed.

The result is shown in figure 6.7. The position was determined on the tensile side of the specimens, where the fracture most likely originated. The fracture locations coincide well with the predicted stress maxima in the simulation, which validates the numerical results.

The fracture probabilities in figures 6.4 a and 6.4 b can now be calculated based on these FEM results. Instead of the analytically-obtained stress fields, I exported the numerically calculated stress fields from Abaqus for further post-processing to Matlab. An interpolation model is fitted to the exported data, which can now be integrated in three dimensions according to equation 2.5. The resulting effective volumes were used to calculate the predictions of the three-point-bending fracture probabilities again. As before, the two four-point-bending setups (75.5 mm and 28.8 mm load distance) served as input for the prediction.

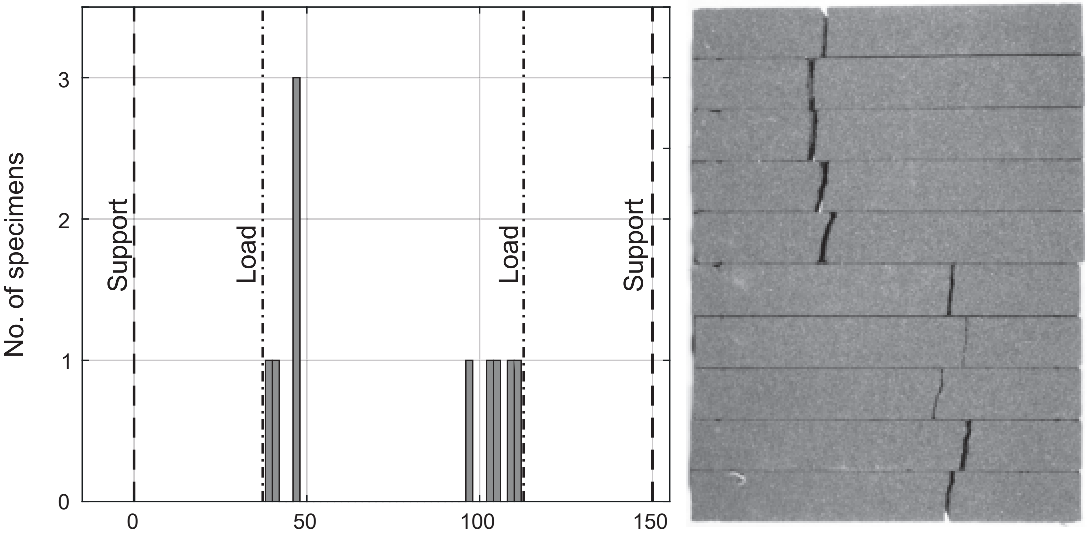

(a) (b)

Figure 6.7: The fracture locations of ten specimens in the four-point-bending experiment group around the stress peaks, which are predicted in FEM. On the left-hand side the number of specimens is plotted over the fracture location (a). On the right side the specimens are depicted (b).

Figure 6.8 shows the results. The scale parameter of the three-point-bending fracture force data is predicted to be 2.85 MPa based on the 75.5 mm data and 2.84 MPa based on the 28.8 mm data.

As the target is 2.88 MPa, the prediction has greatly improved and the difference between the two input data sets is not significant any more. The remaining model error is smaller than 2% of the original absolute measured values. The FEM calculation appears to be independent of the step in effective volume, at least for these bending setups.

These results show that FEM data can be utilised to integrate the effective volume of specimens and to predict the fracture stress of arbitrary bending experiments accurately. In a more abstract view, this enables to predict the fracture stress of complex core geometries with a principal stress criterion, which is highly relevant for industrial application. While in this case an analytical solution was possible, due to the simple geometry of the beams, a numerical solution is necessary for stress calculation of complex geometries and load cases.

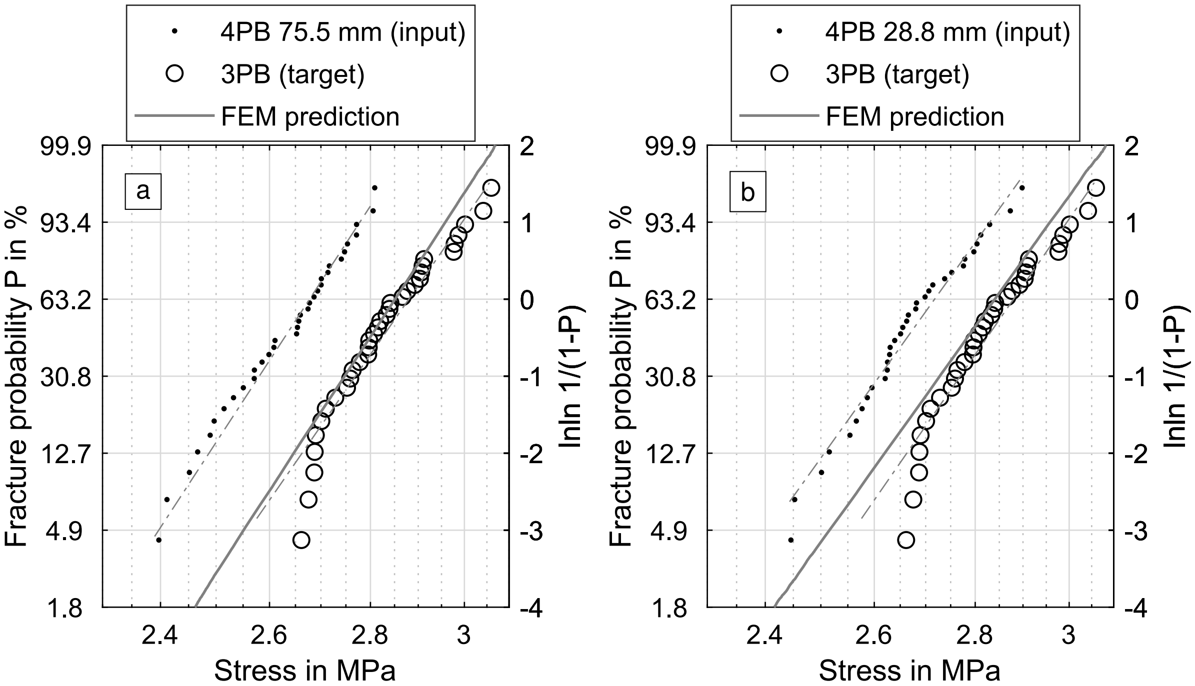

Figure 6.8: Experimentally obtained fracture probabilities for a four- and a three-point bending setup. Based on the FEM results of four-point bending setup (75.5 mm load distance in plot a and 28.8 mm in plot b) a prediction is calculated for the three-point bending setup. The quality of the prediction is improved compared to the purely analytic prediction.

6.2 Fracture Strength

In this section, I will analyse the fracture strength of inorganically-bound core materials under several stress states with increasing complexity. The experiments will be performed on specimens produced with the sand-binder system IN-1-1 as a specific example of inorganically-bound cores. Starting at uni-axial tension and compression, the stress states will evolve to plane stress load cases and finally to experiments under hydrostatic pressure. These experiments will determine support points in the principal stress space to fit a failure surface and validate it for future applications. Please note that in this section all experimental results are scaled to the effective volume of the three-point-bending experiment according to Weibull statistics and the approach outlined in the previous section. Only after the volume scaling, the strength values are directly comparable.

6.2.1 Uni-axial Experiments

For frictional materials, the compressive strength is typically higher than the tensile strength (Zhao et al., 2011). Therefore, I determined both to characterise the uni-axial failure behaviour. The uni-axial compressive strength was acquired with the newly developed test setup described in section 4.2.4. This test setup is able to induce uni-axial and bi-axial stress states into a cubic specimen. In this case, I used only one wedge to achieve a uni-axial stress field. The individual stress values are shown as a group of grey dot symbols in the vicinity of the σ_2-axis in figure 6.9. The scale factor of the data set is 8.0 MPa, depicted with a black diamond, with a shape parameter of 10.0 (ten specimens).

To determine the tensile strength, the three-point-bending test setup was utilised. The bending experiment induces a symmetrical stress field into the specimen with compressive stresses on one side of the neutral layer and tensile stress on the other. It can be assumed that the fracture is induced on the tensile side of the bending beam, since the tensile strength is lower than the compressive strength. This allows to utilise the bending experiment to determine the tensile strength of core materials. This hypothesis was confirmed in a previous publication (Lechner et al., 2020). The results are shown in figure 6.9. The individual stress values are depicted with grey dots (8 specimens), while the Weibull scale parameter of the data set is depicted with a black circle. The scale parameter is 3.3 MPa with a shape parameter of 36.

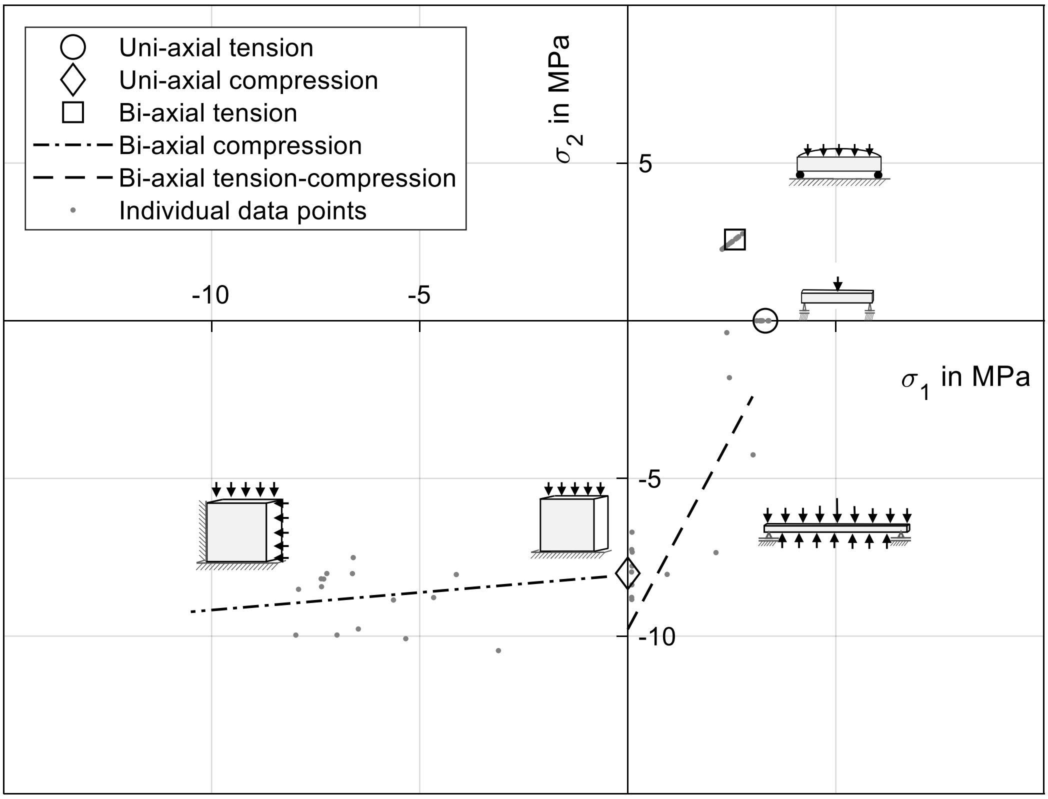

Figure 6.9: Test results of the plane stress experiments. The individual data points are shown in grey, while the Weibull scale parameters are marked in black. The lines are linear best fits to the test results in the respective quadrant. The dash-dot line is fitted to the bi- and uni-axial compression test results, while the dashed line is fitted to the results of the sandwich bending experiment. (Lechner, Hartmann et al., 2021)

Discussion The accuracy of the analytical solution for the three-point-bending problem in comparison to an FEM simulation was already discussed in section 6.1. Figure 6.10 (left) shows the uni-axial compression stress field in the FEM simulation for a total load of 100 N equally distributed over the area of the rubber pad. The calculation of the uni-axial compression stress with equation 4.1 leads to a constant stress of 0.88 MPa for a load of 100 N. The analytic solution fits well to the inner parts of the specimen. However, near the edges in direct vicinity of the rubber pad, the stress is higher than the analytic solution. This typically leads to broken edges of the specimen in the experiment (figure 6.10 on the right side). These small fractures do not stop the test procedure, since the drop in the testing force is negligible. It continues until the testing force drops by 20 %. Subsequently, the specimen is fractured in two or three parts, when the stress in the rest of the specimen reaches the material strength limit. The broken edges change the area of contact to a small degree, however this influence is negligible, as well. Therefore, I conclude that the analytical solution and the assumption of a constant stress is accurate enough to analytically evaluate this test in the future.

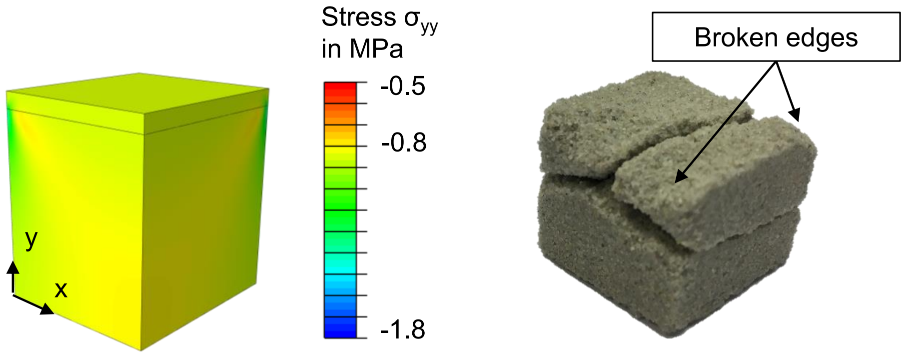

Figure 6.10: Stress fields in the uni-axial compression test setup (left) and a broken specimen (right).

6.2.2 Bi-axial Compression Experiment

For the bi-axial compressive strength, I utilised both wedges of the previous test setup to achieve a bi-axial stress state. The test setup was designed to induce adjustable stress levels into the specimens. The force of the testing machine is divided between the two wedges. The proportion for each wedge can be adjusted with screws. In this experiment, I started with an asymmetric stress field with $\sigma_1 < \sigma_2$ and increased σ_1 continuously to a near symmetrical stress state. This process leads to a point cloud, which describes the failure criterion in the compression-compression quadrant. Therefore, I did not calculate one single scale parameter. Instead, I fitted a linear function into the data set to account for the continuous character of the point cloud. The uni-axial test results are included in this fitting process, since they are acquired with the same test setup and represent one limit of the point cloud. The decision for a first order polynomial function is preliminary and will be reviewed in the next section, when failure models are fitted to the data. The fitted function is depicted in figure 6.9 as a dash-dot line. The slope of the line is almost horizontal, which will be an important criterion to distinguish between failure models in the next section. The individual data points are shown as grey dot symbols in the compression-compression quadrant.

Discussion The accuracy of the analytically calculated stress state has to be evaluated for future experiments. Analogous to the uni-axial compression experiment, I simulated the stress state for the bi-axial compression. Figure 6.11 shows the two relevant stress components in the specimen and the rubber pads. Each load is 100 N, distributed over the area of the rubber pads. The analytical evaluation for each of the stress components leads to 0.88 MPa stress in x and z-direction. As expected, both stress components are symmetrical and most of the specimen is close to the analytical solution. Similar to the uni-axial simulation, there is a stress peak near the edge between the two rubber pads. Analogously, this leads to a small fracture of the specimens' edges, which does not affect the test procedure and the results significantly. For each stress component one rubber pad has significantly lower stress values, which are induced by the friction in the contact. This leads to the conclusion that the analytic solution is suitable to evaluate the stress state in the specimen.

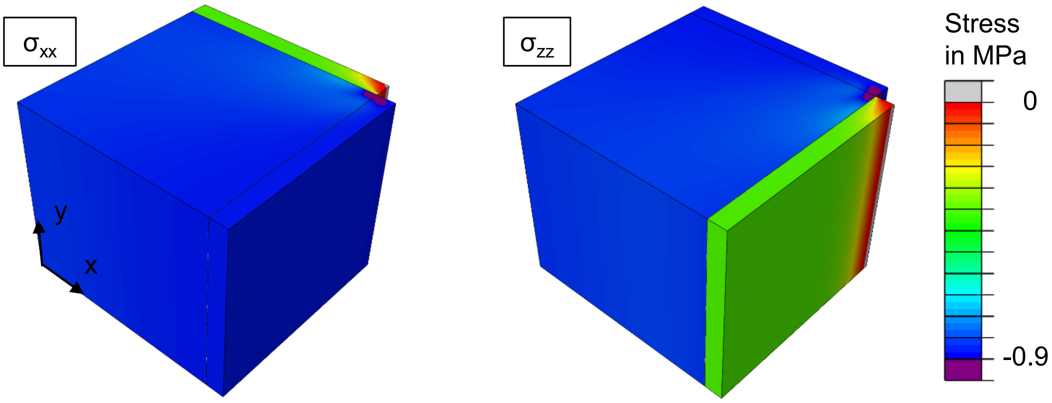

Figure 6.11: Stress fields in the bi-axial compression test setup. Most of the specimen shows a homogeneous stress field for both stress components. The edge between the rubber pads is the only significant stress peak.

6.2.3 Shear Stress Experiment

In order to study a bi-axial tensile-compression stress state, experiments have been performed with the sandwich-like test setup described in section 4.2.4. The experiments were recorded with a high-speed camera. The images were evaluated with digital image correlation and an algorithm proposed by Hartmann et al. (Hartmann et al., 2018). In a previous publication it was shown that this algorithm is able to evaluate the strains in bending experiments with inorganic core materials (Lechner et al., 2020). Here, the algorithm is utilised to not only determine the ϵ_{xx} strain in the beam, but also the ϵ_{yy} and the ϵ_{xy} component. The ϵ_{yy} component is induced by the steel beams. The ϵ_{xy} component represents shear stress, which is induced by the friction between the steel beams and the core material. With these components a symmetrical strain tensor can be build which is transformed to principle strain space (ϵ_1 and ϵ_2). One example of the evaluated high speed images is shown in figure 6.12. It depicts the original images as well as the ϵ_{xx}, ϵ_{yy}, ϵ_{xy}, ϵ_1 and ϵ_2 evaluation of the images for three selected points in time during the experiment. In t_1 the strain is not localising yet. In t_2 the strain starts to localise, while in t_3 the fracture is complete. This fracture is invisible to the human eye in the original images.

The fracture is induced on the tensile side, which validates the assumption, that bending specimens fracture on the tensile side.

I performed six experiments with this test setup. The resulting individual fracture stresses are depicted in figure 6.9 with grey dots in the tension-compression quadrant. For evaluation, I selected the last image before the strain localisation starts and evaluated the mean strain in the area marked with a black rectangle. The strains are multiplied with the Young's modulus obtained in chapter 5, according to Hook's law. The Young's modulus was corrected with a factor of 0.8, since the Young's modulus at fracture load is 20 % lower than without significant load during impulse excitation (Lechner et al., 2020).

Discussion The ϵ_{xx} principal strain resembles the strain expected in a bending beam, with negative strains in the upper half, which translates to compression and positive strains in the lower half. Since the coordinate system is rotated individually for each subset into principle strain space, the orientation of the ϵ_1 values are not directly comparable with the xx-direction. However, since the results of ϵ_{xy} are comparatively small, the results are similar. With local exceptions, ϵ_{yy} shows negative strain over the full height of the beam, which indicates that the steel beams are in fact inducing pressure. The positive strain peak in the lower right corner indicates a small surface failure, which happened early in the test and is not growing with the rising testing force.

Due to the in-homogeneous and porous surface of the specimens, the local pressure which is induced into the specimens varies from specimen to specimen. However, this is not a problem, since the strain tensor can be evaluated locally with digital image correlation. Therefore, the specimens build a point cloud similar to the bi-axial compression experiments. Analogously, I fitted a linear function to the data points, which will be checked in the next section for validity. Please note that the high-speed images cover only a section of the whole bending beam. Therefore, it is not possible to calculate the effective volume exactly. Furthermore, it is not possible to calculate the exact stress field for each specimen numerically or analytically. The stress state at the point of fracture is highly individual, which makes it difficult to calculate a reliable stress field: The local pressure in the contact interface between the steel beams and the core material cannot be modelled accurately. Thus, I will exclude these results from the calculation of the future model parameter. However, I will utilise these results as further validation for failure criteria which are fit to the failure surface.

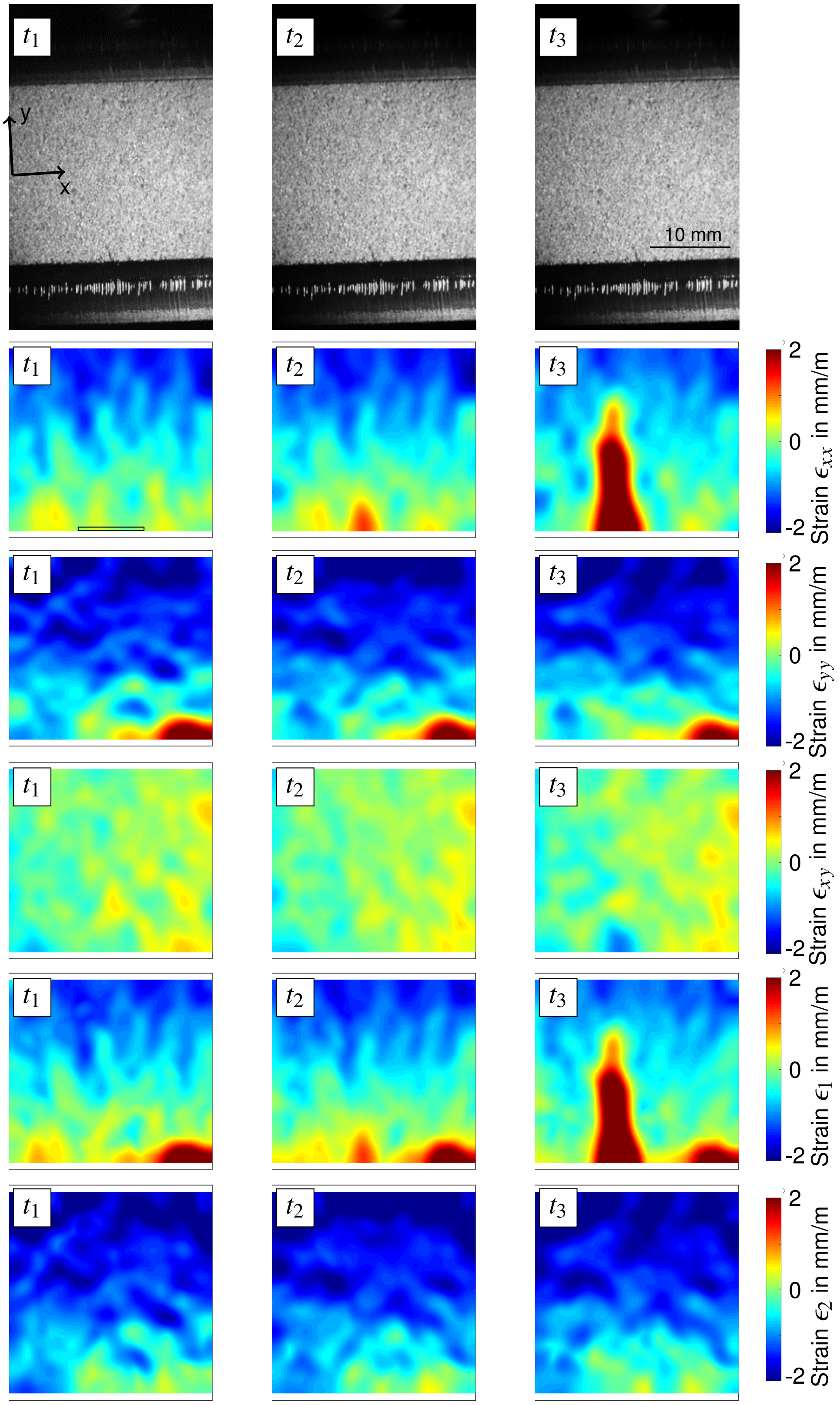

Figure 6.12: Strain on the specimens surface calculated via digital image correlation for the novel sandwich bending experiment and three points in time (t_1-t_3). The stress components ϵ_{xx},ϵ_{xy} and ϵ_{yy} are in the local coordinate system, while ϵ_1 and ϵ_2 are principle strains.

6.2.4 Bi-axial Tension Experiment

The bi-axial tensile strength was determined with an adaption of the bulge experiment, which realises a pressure on ring experimental test setup for core materials. The individual results of the experiments are shown in figure 6.9 in the tension-tension quadrant, while the Weibull scale parameter is depicted with a black square. After scaling the experimentally obtained stresses to the effective volume of the other experiments, the scale parameter is 2.6 MPa with a shape parameter of 19 (twelve specimens).

Discussion With the assumption that shear stresses are negligible, due to the small height of the specimen compared to the diameter, the principal stresses are equal to the radial and tangential stresses calculated with equations 4.3 and 4.4. Figure 6.13 (right) shows the relevant shear stress component in the specimen, which were calculated with a FEM model with 25 N load distributed over a quarter of the specimen's area (two symmetries in the model). The shear stress is negligible, which confirms that equations 4.3 and 4.4 can be utilised to evaluate the principal stresses. Furthermore, the equations lead to a maximum tensile stress of 1.0 MPa, while the simulation results in 0.90 MPa stress. While this difference between numerical and analytical solution is higher than the difference of the compression experiments, it is well within the scatter of the data: The standard deviation of the bi-axial bending experiments is 0.13 MPa. Due to the point symmetry in the test setup, the principal stresses are equal in the middle of the disc, where the maximum stresses are expected according to plate theory (Hake and Meskouris, 2007, p.107). The two relevant stress components in x and z-direction are shown in figure 6.13 (left). Typically, there is a neutral layer in bending experiments with compressive stresses on one side and tensile stresses on the other. Both principal stress components contribute to the effective volume of the test setup.

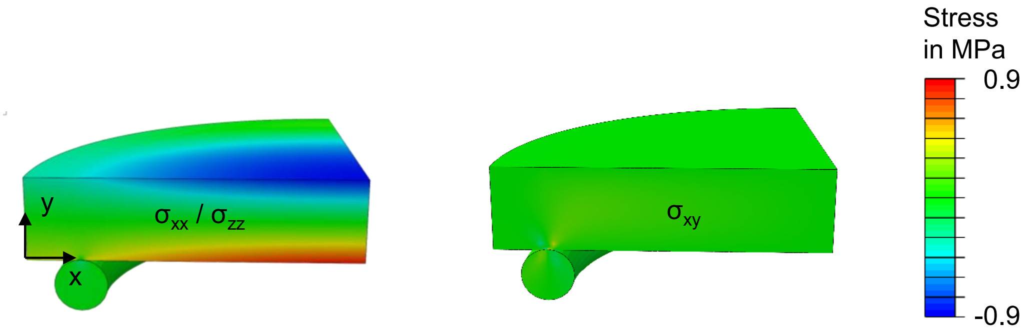

Figure 6.13: Stress fields in the bi-axial bending test setup. The shear stress on the right-hand side is negligible.

6.2.5 Hydrostatic Stress Experiment

In this section, the results of the compression and the bending experiments under hydrostatic pressure will be presented. The test bench is described in section 4.2.5. The tests have been performed up to approximately 14 MPa ambient pressure for bending experiments and 8.5 MPa for compression experiments. Figure 6.14 depicts the results of both experiments. On the left side, the plot shows the uni-axial yield stress over the ambient pressure. On the right side, the deviatoric radius is plotted over the first stress invariant. The deviatoric radius is defined by Ehlers as $\sqrt{2J_{II}}$ (Ehlers, 1993). Both forms are common to represent the friction angle of materials. Figure 6.14 shows a linear correlation between the ambient pressure and both yield stresses. The slope for the bending experiments is −1.28 Pa/Pa, while the slope for the compression experiments is 0.413 Pa/Pa.

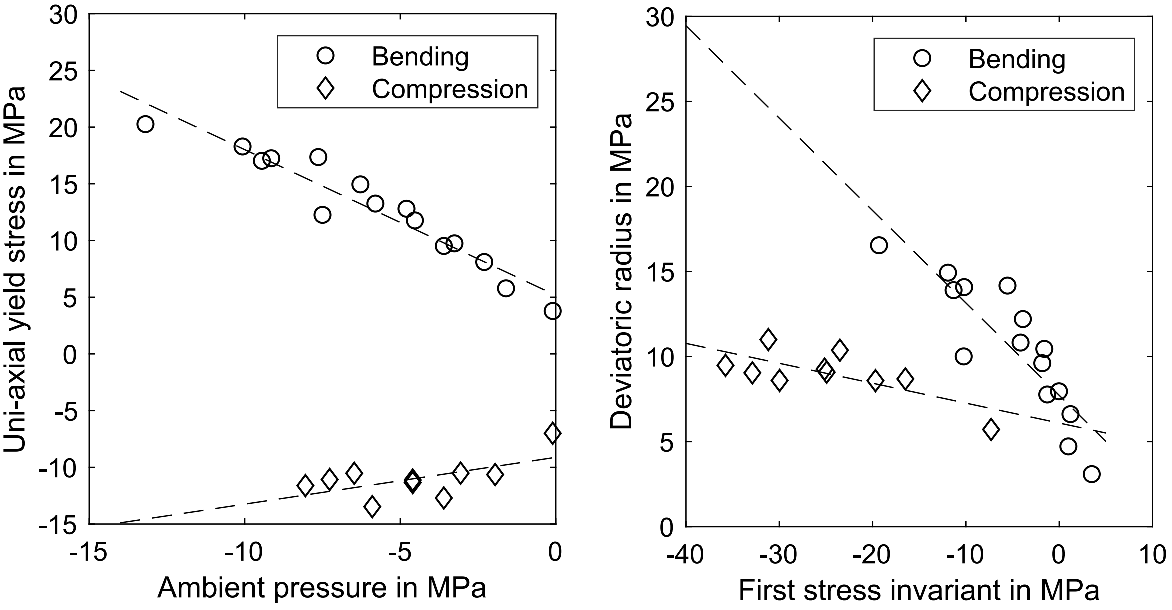

Figure 6.14: Results of hydrostatic bending and compression experiments. The yield stress is depicted over the ambient pressure, on the left side. On the right side, the deviatoric radius is plotted over the first stress invariant. The bending and the compression experiments show different slopes, which results in different friction angles.

Discussion How do the results achieved with this novel test bench compare to the uni-axial experiments? I performed bending and compression experiments without additional ambient pressure in the hydrostatic test bench and common experiments on the universal testing machine. The bending experiments resulted in 3.0 MPa for the common bending and 3.8 MPa for the hydrostatic test bench. The compression experiments lead to 5.2 MPa and 7.0 MPa compressive strength for the uni-axial test setup and the hydrostatic test bench, respectively. Both strength values are higher in the hydrostatic test bench, which is probably due to the mechanical influence of the sealing around the specimens. The additional layer around the cores lead to higher mechanical strength values. However, this influence is constant and independent of the ambient pressure. Thus, the friction angle should be unaffected. Nevertheless, it is useful to reduce the sealing to its minimum thickness and thus its influence on the measurement. Since Ettemeyer et al. showed that the hydrostatic pressure on a core in the sand casting process is approximately 14 MPa (Ettemeyer et al., 2021), I decided that this ambient pressure is sufficient, while the test bench is able to perform experiments up to 22 MPa.

In comparison, Caylak and Mahnken found a slope of approximately 2 Pa/Pa with a hydrostatic compression experiment of up to 1 MPa hydrostatic pressure for an organic cold box system (Caylak and Mahnken, 2010). They did not determine the friction angle for a bending or tensile experiment. Most studies, which discriminate between an extension and a compression friction angle are related to geo-sciences. Ehlers models soil with a higher friction angle for a compression state than for an extension state (Ehlers, 1993). Müllerschön studied unbound Berliner sand and found that friction angles for compression states are higher than for extension states. However, there was only a small difference (Müllerschön, 2000, p. 39). This is the pendant to the compression and bending experiments on a Mohr's circle. Dehler and Labuz tested sandstone in a triaxial experiment and found a higher friction angle for compression than for extension, as well (Dehler and Labuz, 2007).

Therefore, the mechanical behaviour is different from existing literature about soils and sandstone mechanics, since the friction angle of inorganic core materials is significantly higher for bending (extension) experiments than for compression experiments. One possible reason for this is the different microstructure of the porous media. While core materials have defined binder bridges between the grains, sandstone and soils do not and are hold together by compaction, water (soils) and cement (sandstone). This theory will be studied in future experiments.

6.2.6 Discussion of the Failure Surface

In the following section, I will discuss, which failure criterion is most suitable to model the mechanical behaviour of core materials. As the results of bending and compression experiments under hydro-static stress show, the deviatoric fracture stress is approximately proportional to the first invariant of the stress tensor, which describes the hydro-static stress state. Therefore, only three of the yield criteria detailed in section 2.3.2 are worth considering. These are: The Drucker-Prager, the Mohr-Coulomb and the Ehlers criterion. The Drucker-Prager and the

Mohr-Coulomb model are two parameter models. While this is an advantage, since only two well-chosen experiments are necessary to parametrise them, it may be necessary to adapt them to the mechanical behaviour at hand due to their simplicity. The criterion proposed by Ehlers models a non-linear relation between the hydro-static stress and the deviatoric fracture stress with seven parameters (Ehlers, 1993).

In a first step, I will compare the uni- and bi-axial test results with these three criteria in the plane stress state. In figure 6.15, I have fitted a Drucker-Prager (a), a Mohr-Coulomb model (a) and a Ehlers criterion (b) to the plane stress experimental data. Clearly, the Mohr-Coulomb model fits better to the data than the Drucker-Prager model. The difference is most evident in the compression-compression quadrant, where the Drucker-Prager model is not able to mimic the near horizontal failure curve of the experimental data. The Ehlers criterion can model the mechanical behaviour of the failure surface. However, the high number of parameters (seven) lead to the necessity of at least seven experimental data points in principal stress space to parameterise the model. Moreover, five of the seven parameters describe the shape of the failure criterion along the hydrostatic axis (Volk, 1999, p. 62). These parameters cannot be properly quantified with only plane stress data. However, with more data distributed in a three-dimensional stress space the criterion could describe the mechanical behaviour well.

I conclude from the plane stress data that only the Ehlers criterion and the Mohr-Coulomb criterion are suited to describe the shape of the failure surface. While the Mohr-Coulomb model has only two parameters and therefore a low model complexity, the Ehlers model is quite complex and able to model non-linear behaviour more accurately. In the next step, I will compare these two models with regard to the hydrostatic experiments. The results showed that the friction angle of bending and compression experiments differ significantly. The Mohr-Coulomb model is not able to model this behaviour due to its simplicity. Only one isotropic friction angle is possible. In contrast, the Ehlers criterion is able to model mechanical differences between compression and extension. Figure 6.16 compares the criteria with regard to their deviator plane, which is orthogonal to the hydrostatic axis. Ehlers defines the shape of the failure surface in the deviator plane with the Lode angle θ and the deviatoric radius (Ehlers, 1993, p. 370). The Lode angle determines if the specimen is compressed or elongated. While the Mohr-Coulomb model on the right side is not able to differentiate between a state of compression and extension, the Ehlers criterion is. Therefore, the Ehlers criterion has an advantage, if the mechanical behaviour has to be modelled accurately at higher hydrostatic stresses. However, there have to be sufficient data points in three-dimensional stress space to parameterise the model, due to the model complexity.

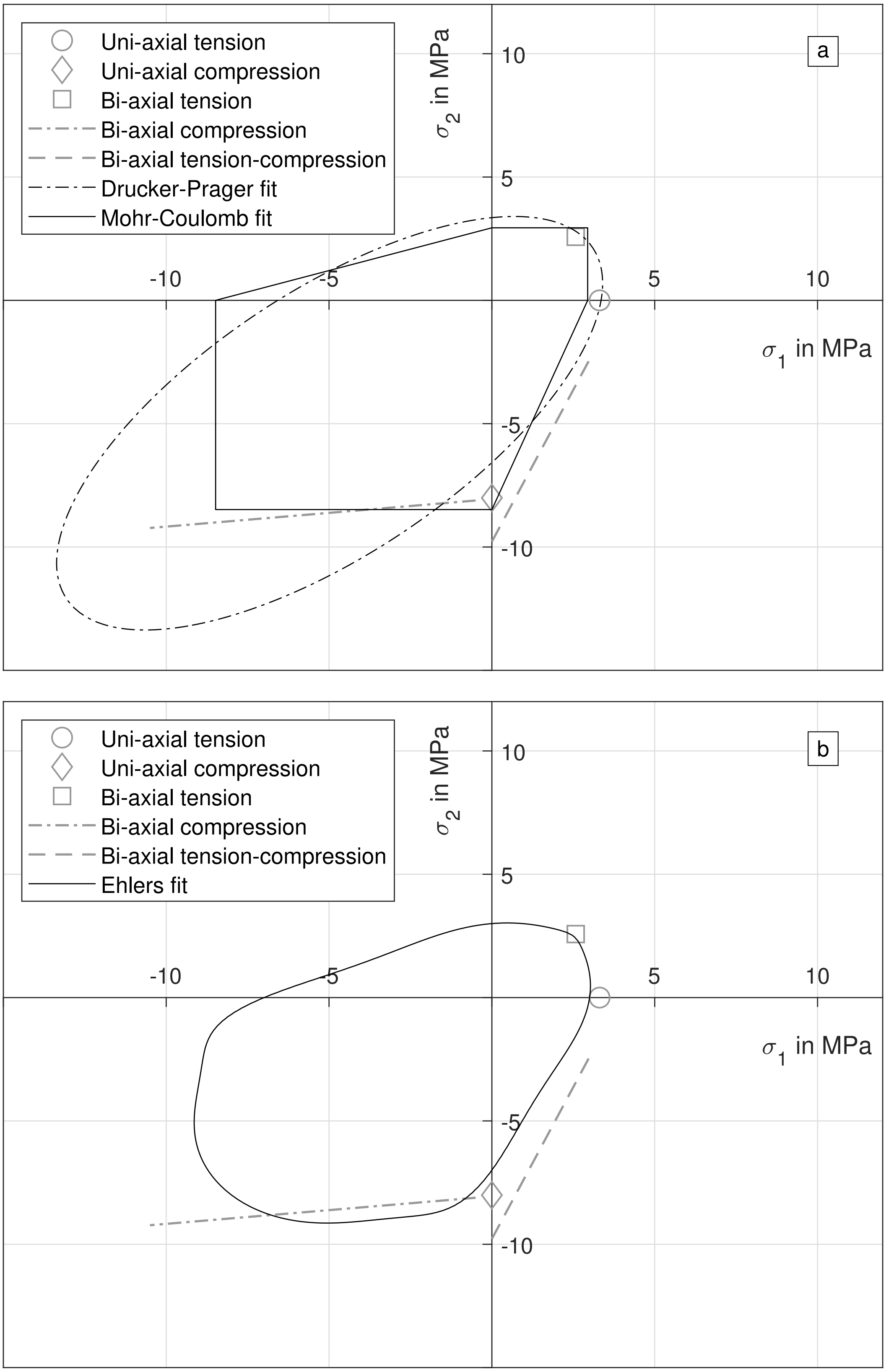

Figure 6.15: Experimental results for several uni- and bi-axial stress states. A Drucker-Prager (a), a Mohr-Coulomb (a) and a Ehlers criterion (b) are fitted to the test results.

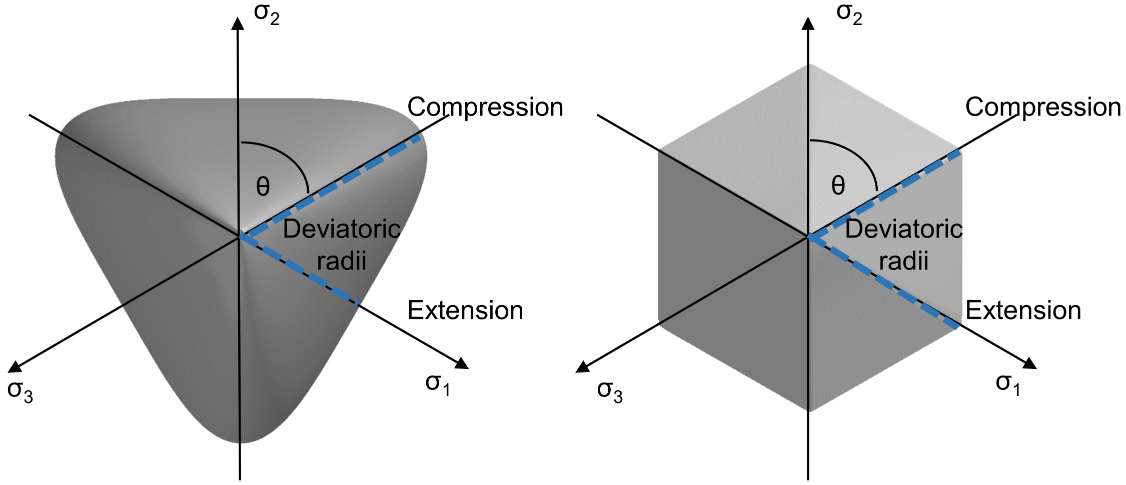

Figure 6.16: Comparison of the Ehlers criterion with the Mohr-Coulomb criterion in the deviator plane. The Ehlers criterion allows different deviatoric radii for compression and extension stress states, while the Mohr-Coulomb criterion does not. (after Ehlers, 1993, p. 370)

The necessary experimental equipment and the experimental effort are significant and will not be feasible for most research institutes and casting companies. Therefore, I propose to utilise the Mohr-Coulomb criterion with an average friction angle up to a threshold of 5 MPa hydrostatic pressure. This threshold limits the model error which results from the homogeneous friction angle to <10 % for the material at hand. The core handling operations, which are the aim of this material modelling will be well below this threshold. If the hydrostatic pressure is higher in future applications, a more complex material model should be utilised, which allows to differentiate the friction angles of compression and extension stress states.

Thus, I will further discuss the Mohr-Coulomb criterion and its application to core materials in the following. The Mohr-Coulomb parameters found with the data set in figure 6.15 are $c = 2.87$ and $\phi = 0.61$. The Mohr-Coulomb friction angles, which result from the hydrostatic experiments are $\phi_b = 0.23$ and $\phi_c = 0.82$. The angle which is calculated from the plane stress experiments is averaging the bending and compression friction angles. The average of the hydrostatic angles is $\phi = 0.53$, which is close to the friction angle of the plane stress experiments. Therefore, the bending and the compression experiments are suited to calculate an average friction angle.

The Mohr-Coulomb model describes shear induced failure as soon as one shear stress exceeds the failure stress calculated in equations 2.21-2.23. Only the highest shear stress is considered in this evaluation. The other two shear stresses are disregarded. In section 6.1 it was shown, that inorganic core materials follow the weakest link theory. Weibull's theory dictates, that in case of multi-axial stress states every principal stress component contributes to the fracture probability of the specimen, as stated with equation 2.6 for a bi-axial stress state. How can these results be consolidated into one consistent failure model?

The principle of independent action states that the fracture probabilities induced by every individual principal stress component can be treated independently, which is also called the Barnett-Freudenthal approximation (Barnett et al., 1967, p. 112):

$$P = 1 - \exp\left[-\int_V \left(\frac{\sigma_1}{\sigma_0}\right)^m + \left(\frac{\sigma_2}{\sigma_0}\right)^m + \left(\frac{\sigma_3}{\sigma_0}\right)^m dV\right]. \tag{6.3}$$

Essentially, the probabilities of survival for each stress component are multiplied to calculate one probability of survival, which in turn allows the probability of failure to be evaluated.

In order to adapt this principle to shear induced failure of the Mohr-Coulomb model, the probability of survival s has to be calculated for any given principal shear stress:

$$s_i = \exp\left(-\left(\frac{\tau_i}{\tau_{MC_i}}\right)^m\right), \tag{6.4}$$

where τ_i are the principal shear stresses and m the Weibull shape parameter of the data set. τ_{MC_i} are the shear stress limits described in Equations 2.21 to 2.23 (right sides of the equations). According to the principle of independent action, the probability of survival for each principal stress is handled independently. The failure surface in principal stress space can be determined analogously to the scale parameter in Weibull's theory: Failure is assumed if the fracture probability of the specimen exceeds $1 - \frac{1}{\exp 1}$. Therefore, the failure surface can be described with the following equation (Lechner, Hartmann et al., 2021):

$$1 - \prod_{i=1}^{3} s_i = 1 - \frac{1}{\exp 1} = 0.6321, \tag{6.5}$$

with equations 2.21 to 2.23 and 6.4 this leads to:

$$\begin{aligned} \exp\Bigg[&- \left(\frac{0.5|\sigma_1 - \sigma_2|}{0.5(\sigma_1 + \sigma_2) \cdot \sin(-\phi) + c \cdot \cos(-\phi)}\right)^m \\ &- \left(\frac{0.5|\sigma_2 - \sigma_3|}{0.5(\sigma_2 + \sigma_3) \cdot \sin(-\phi) + c \cdot \cos(-\phi)}\right)^m \\ &- \left(\frac{0.5|\sigma_3 - \sigma_1|}{0.5(\sigma_3 + \sigma_1) \cdot \sin(-\phi) + c \cdot \cos(-\phi)}\right)^m \Bigg] \\ &= \exp 1^{-1} \end{aligned} \tag{6.6}$$

This equation describes a three parameter failure surface for brittle materials based on the Mohr-Coulomb model and the weakest link theory. Figure 6.17 shows the failure surface for the shape parameter $m = 10$ and m = 22 for plane stress and in the deviatoric plane.

The difference between the original Mohr-Coulomb model and the new probabilistic adaption is only visible at the edges of the failure surface. Here, the second highest shear stress is contributing significantly to the fracture probability, which is neglected by the classical Mohr-Coulomb formulation. This effect is dependent on the scatter in the data, which is represented by the Weibull shape factor. For an infinite shape factor, which corresponds to zero scatter, the failure surface of the new model would be equal to the classical Mohr-Coulomb surface. Higher scatter increases the probability that the second highest shear stress leads to the fracture of the specimen. Generally, it can be stated that uni-axial and perfectly symmetrical stress states in principal stress space tend to fracture at lower maximum shear stresses, since they both lead to two equal shear stress components according to equations 2.21-2.23. This can be seen partly in the data of the compression experiments in figure 6.9. The uni-axial compression experiments lead to lower principal stress values than the bi-axial compression experiments, which are not near the symmetrical stress state. The rounding of the edge for symmetrical bi-axial compression can not be conclusively confirmed with the data at hand, since it is experimentally difficult to achieve enough data points with a symmetric stress state.

The average shape parameter of all test setups utilised to fit the Mohr-Coulomb model in figure 6.15 is $m = 21.8$. An error minimisation based on the data points at hand and this new Mohr-Coulomb equation leads to the parameters $c = 2.93$ and $\phi = 0.61$. While the friction angle ϕ stays constant, the cohesion c is slightly increased compared to the classical Mohr-Coulomb criterion ($c = 2.87$). Furthermore, the experiments show that it is possible to calculate the Mohr-Coulomb parameter with only the data of a uni-axial compression and a bending experiment. Compared to the typical scatter in the strength data of core materials, the difference is not significant and it is important to utilise simple and cost-efficient tests with regard to future industrial application. To keep the number of necessary specimens as low as possible, the broken parts of the bending specimens can be used again for the compression test.

Figure 6.17 shows that the difference between the new and the classical formulation is only significant for the compression tests, since they show higher scatter (m=10). In any case, a consistent mechanical theory is important, which consolidates all aspects of the material characterisation in this thesis. Moreover, equation 6.5 offers advantages compared to the classical Mohr-Coulomb formulation in equations 2.21-2.23.

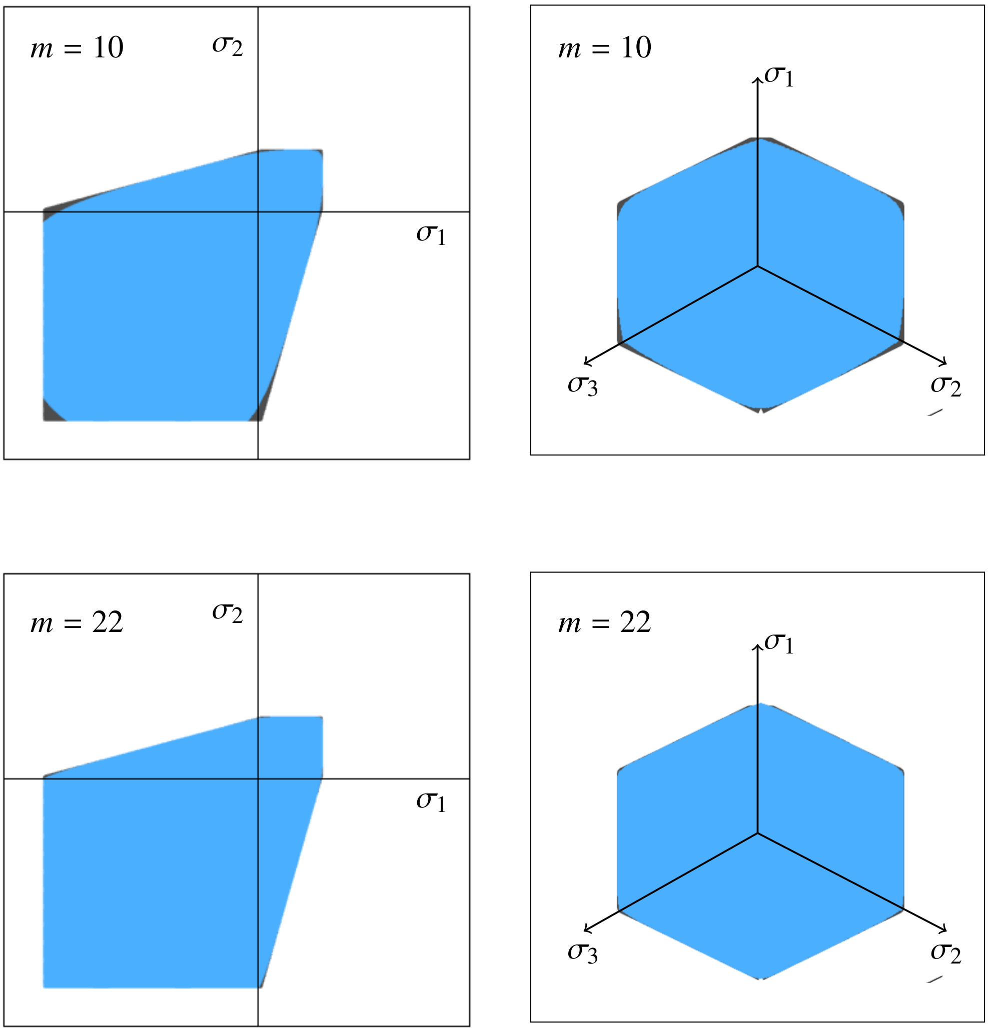

Figure 6.17: Comparison of the failure surfaces in the plane stress and the deviatoric plane for the theoretical Mohr-Coulomb criterion without scatter (black) and a Mohr-Coulomb criterion adapted with weakest link theory (blue). Weibull shape parameters are $m = 10$ and $m = 22$. (Lechner, Hartmann et al., 2021)

In contrast to the three equations of the classic formulation, the originally sharp edges are rounded, which is advantageous for numerical differentiation and it can be expressed and evaluated with one implicit equation. At last, the third parameter is not increasing the experimental effort needed to parameterise the model, since the scatter can be evaluated from the experiments already needed for the other two parameters.

Finally, I propose to calculate the effective volume based on the three shear stresses instead of the principal stresses, since the failure is assumed to be shear-induced with a Mohr-Coulomb failure criterion. The calculation of the effective volume in the state of the art is based on the assumption of a principal stress criterion, which is typically utilised for ceramics. However, the effective volume should be calculated in accordance with the material failure, which is shear-induced for core materials. In order to evaluate the effective volume, the shear stresses of each volume element are compared to the maximum shear stress in the specimen. This leads to the following equation to calculate the effective volume (Lechner, Stahl, Hartmann et al., 2021):

$$V_{eff} = \int_V \left(\frac{\tau_1}{\tau_{max}}\right)^m dV + \int_V \left(\frac{\tau_2}{\tau_{max}}\right)^m dV + \int_V \left(\frac{\tau_3}{\tau_{max}}\right)^m dV, \tag{6.7}$$

where τ_x are the principal shear stresses and τ_{max} is the maximum shear stress in the specimen.

Now, all necessary methods are in place to quantify the parameters of a Mohr-Coulomb failure surface for inorganically-bound core materials. This section showed that it is possible to estimate the cohesion and the friction angle based on a uni-axial bending and a uni-axial compression experiment. The next section will analyse, how these model parameters are influenced by the parameters of the core production.

6.3 Influence of Production Parameters on the Failure Surface

In the following, I will utilise compression and bending experiments with IN-1-2 specimens to parametrise the isotropic failure surface for varying production influences. Analogous to the study in chapter 5, the influence of the binder amount, the humidity and the storage time will be analysed. There is a considerable amount of influences to the strength of inorganic core materials. This study serves as an example how the sand-binder system at hand can be characterised for any selection of specific production influences. I believe that the chosen three parameters are the most significant, but not the only influences to the core strength. Please note that the raw data for the figures in the following studies can be found in tables D.4 and D.5.

6.3.1 Influence of Storage Time

In a first step, I will analyse strength data for different binder amounts in plots with a logarithmic x-axis, which shows the storage time. This way, the hardening process can be analysed in detail, which is done with figure 6.18. The most important result is that for the tensile strength the hardening process from 10 s to 24 h follows a logarithmic function, which is represented by the near linear hardening on the logarithmic scale of figure 6.18 a.

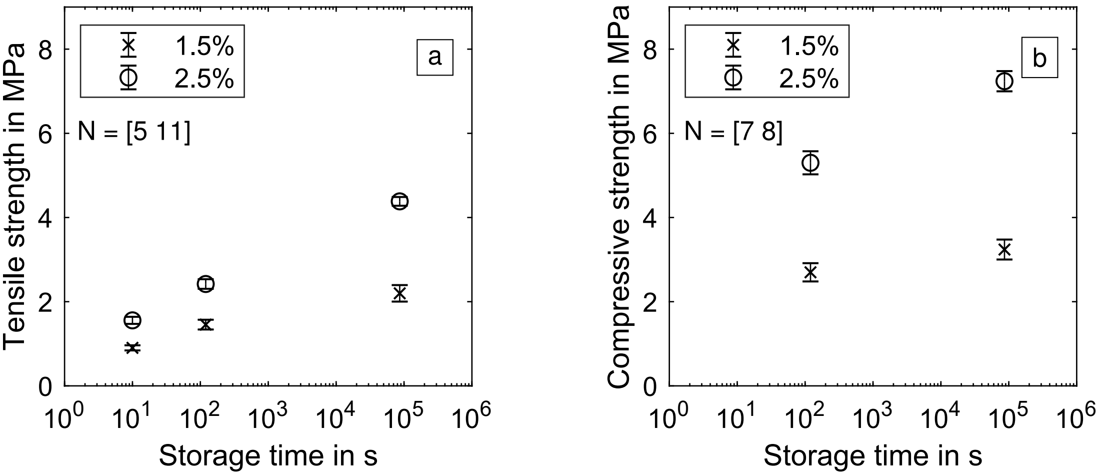

Figure 6.18: Tensile and compressive strength data for various storage conditions and binder amounts (a, b). The error intervals show the standard deviation values. The data has been published in a previous article (Lechner, Stahl, Hartmann et al., 2021).

In this case, I use the standard deviation instead of the Weibull shape parameter, since the scatter will be utilised to calculate the scatter of further properties like the fracture strain. This notation will be valid for all the following figures in this section. After scaling the compressive strength data sets to the effective volume of the bending experiment, the Mohr-Coulomb cohesion and friction angle can be calculated as shown in the section before.

Discussion I assume in the following that the hardening process is affecting the compressive strength in the same logarithmic manner as the tensile strength. Here, the knowledge of the logarithmic hardening is advantageous, since the compressive strength 10 s after the tool opening could not be determined experimentally. The cubic specimen could not be manufactured from the beam-like specimen in that short time span. Therefore, the compressive strength 10 s after tool opening is estimated based on the values after 120 s and 24 h. This estimation is shown in figure 6.19. It is depicted in grey and without a scatter indication, while the experimental values are depicted in black with their standard deviation. The logarithmic increasing tensile and compressive strength values lead to a logarithmic increasing cohesion. The friction angle is decreasing near-logarithmically over time.

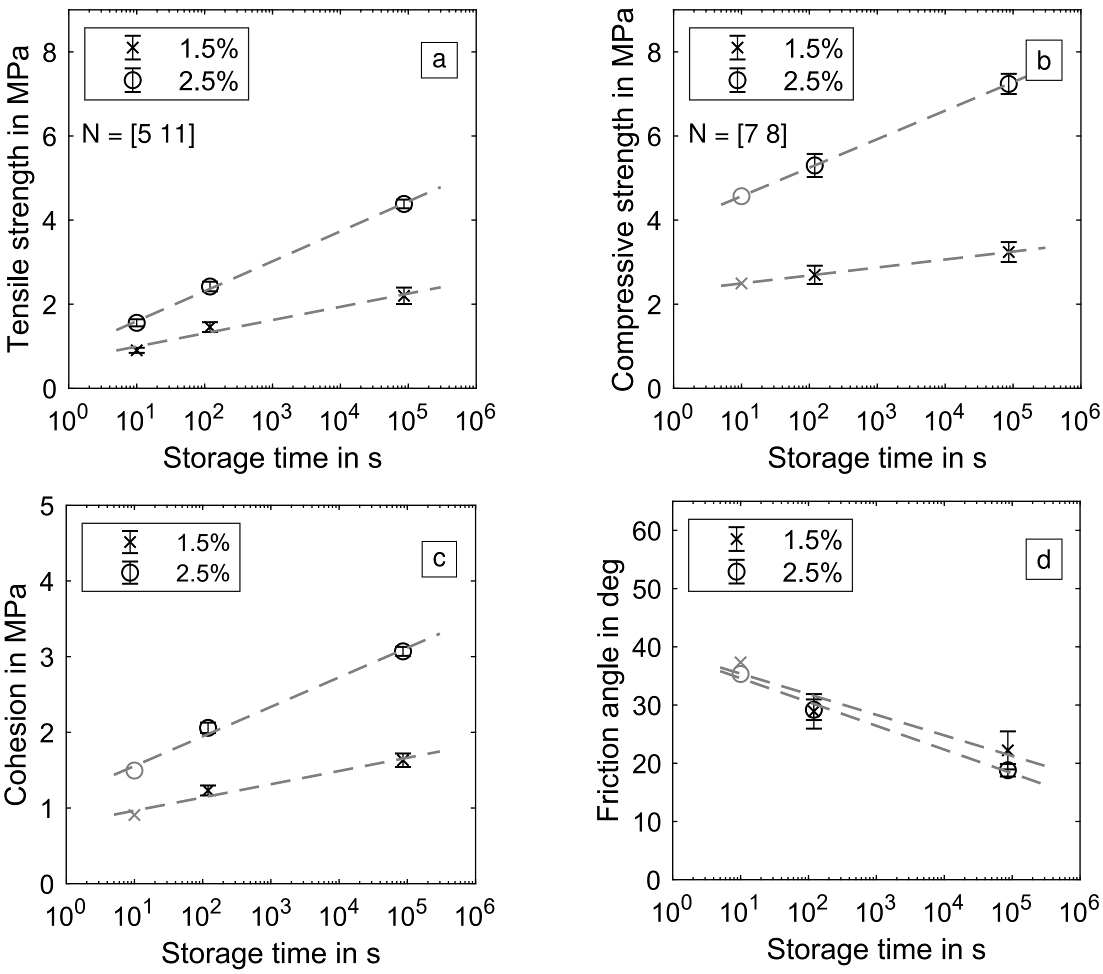

Figure 6.19: Tensile and compressive strength data for various storage conditions and binder amounts (a, b). Furthermore, the material cohesion c and the friction angle Φ *are determined from the strength data sets (c, d). Predictions are made for a storage time of 10 s based on the linear regression.*

Fan et al. found a similar hardening pattern in bending and compression strength values for another sodium silicate sand-binder system (Fan et al., 2004). Furthermore, Stauder et al. analysed the strength data of several organic sand-binder systems over a similar storage time frame and found near logarithmic hardening, as well (Stauder et al., 2016). The logarithmic hardening is very advantageous for future material characterisation efforts, since two experimental data points with different hardening times are enough to estimate the strength values for the whole life cycle of the core, if the rest of the influences on the core's properties remain constant.

6.3.2 Influence of Binder Amount

In a second step, I will analyse the influence of different amounts of fluid binder on the tensile and compression strength of the sand-binder systems. Powder additives of the binder system are scaled accordingly with the fluid binder. The experiments are performed at specific points in time after the core shooting (10 s, 120 s and 24 h), to evaluate possible cross correlations with the binder amount. There is a near linear correlation of the tensile and compressive strength to the binder amount for all storage times (10 s, 120 s, 24 h), as shown in figure 6.20 a and b.

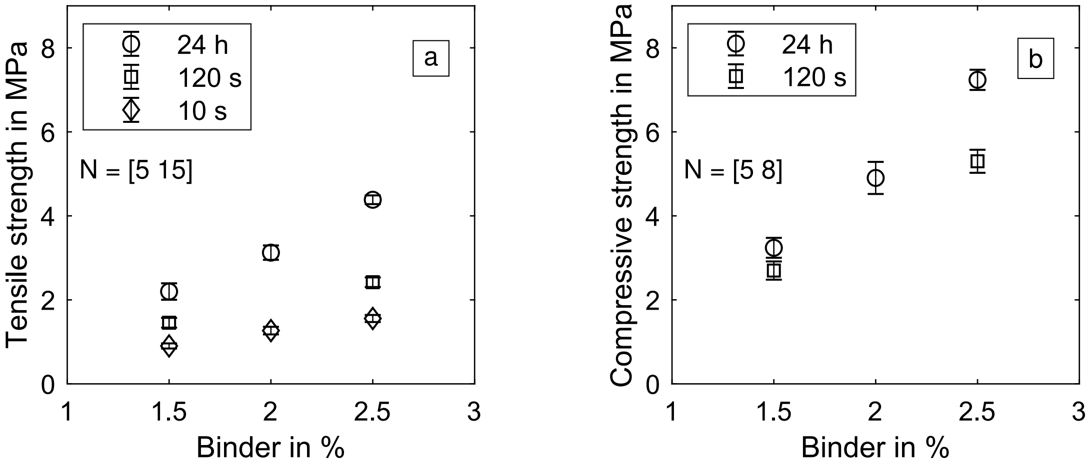

Figure 6.20: Tensile and compressive strength data for various storage conditions and binder amounts. (Lechner, Stahl, Hartmann et al., 2021)

Discussion The compressive strength 10 s after tool opening is calculated based on the logarithmic hardening. This offers the chance to compare the logarithmic extrapolation with the linear interpolation in figure 6.21. Furthermore, both strength values (tensile and compressive) at 120 s for 2 % binder are interpolated as an example how material parameters can be estimated in the future based on support points. The theoretically calculated fracture strain is shown in figure 6.21 c and d. It is calculated with Hook's law from the Young's modulus determined in chapter 5 and the tensile and compressive strength. In a next step, the compressive strength is scaled to the same effective volume as the bending experiment to make both values comparable with equation 6.7 and 6.2. Afterwards, the tensile and the compressive strength values are utilised to calculate the cohesion c and the friction angle ϕ of the Mohr-Coulomb criterion with equation 6.6 via least-square error minimisation. The third parameter m of equation 6.6 is calculated as an average of the Weibull shape parameters of both strength data sets. Please note that the Mohr-Coulomb parameters for 10 s after the tool opening are calculated with an experimentally obtained tensile strength, while the compressive strength is calculated based on the logarithmic hardening.

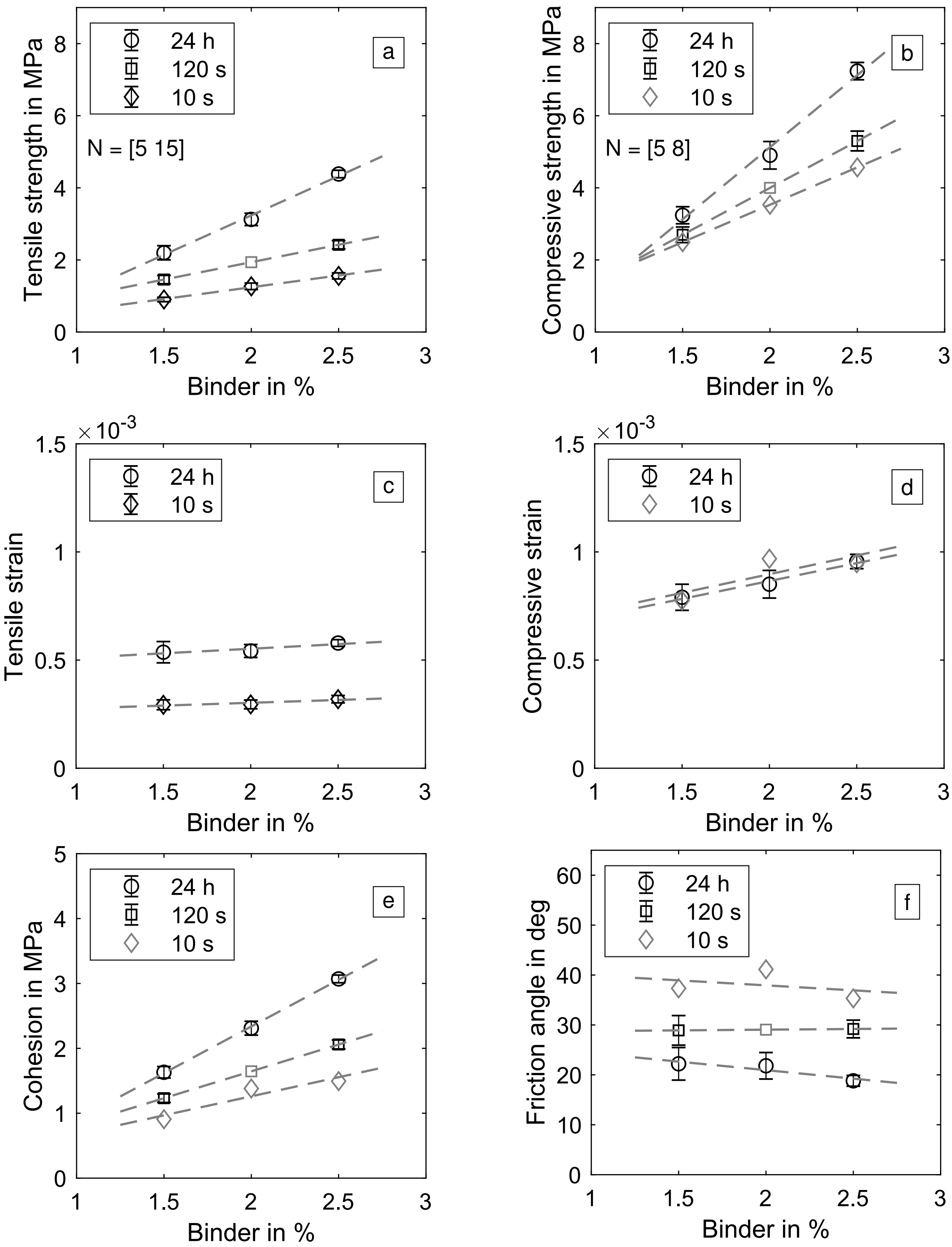

Figure 6.21: Tensile and compressive strength data for various storage conditions and binder amounts. The fracture strain is calculated with Hook's law. The cohesion c and the friction angle Φ are calculated. (Lechner, Stahl, Hartmann et al., 2021)

The tensile strain remains nearly constant for changes of the binder amount, while the compressive strain increases. The cohesion increases linearly with the binder amount, while the friction angles remain constant. The linear correlation between binder amount and material strength are in line with similar studies from Stachowicz et al., which have been performed on microwave hardened water-glass systems (Stachowicz et al., 2011). Furthermore, Granat et al. found an approximately linear correlation for bending and compression strength between 1.5 % and 2.5 %, as well (Granat et al., 2008). For a variation between 0.5 % and 5.0 % binder amount, they found a saturation effect, which leads to a diminishing slope for binder amounts >2.5 %. The constant tensile strain shows that Young's modulus and fracture strength are increasing equally with the binder amount, which results in a constant ratio of both. Furthermore, the tensile strain after 24 h is considerable higher than after 10 s. In contrast, the compressive strain after 10 s is nearly equal to the compressive strain after 24 h. This shows that during the hardening process after the tool opening the tensile strength is growing more than the Young's modulus, while the compressive strength is growing equally to the Young's modulus. The compressive strain after 24 h is significantly higher than the tensile strain, because of the higher compressive strength. The parameter c of the Mohr-Coulomb model is mainly determined by the absolute values of the tensile and compressive strength σ_t and σ_c. Consequently, it is rising linearly with the binder amount for all storage times in figure 6.21 e. The friction angle ϕ describes the relative comparison of tensile and compressive strength. The extreme value would be $\phi = 0$ for $\sigma_t = \sigma_c$.

6.3.3 Influence of Humidity

In a third step, I will study the influence of humidity on the material strength, the fracture strain and the Mohr-Coulomb parameters. Analogous to the humidity study for the elastic parameters, I stored the specimens at 10 %, 25 %, 40 % and 60 % relative humidity. The specimens were taken from the same production batch as the specimens utilised for the elastic study. Therefore, the moisture values, which result from the humidity are the same as before. 10 % humidity correlates to 0.09 % moisture, 25 % humidity to 0.12 % moisture, 40 % humidity to 0.12 % moisture and 60 % to 0.26 %. Figures 6.22 and 6.23 show the mechanical results with regard to the humidity and the moisture, respectively. The increasing moisture in the sand-binder-system is decreasing the material strength, which applies for tensile and compressive loads. Since the cohesion is calculated from those values, it decreases analogously. However, the friction angle is mainly influenced by the ratio of those two strength values and is independent of the absolute strength. It rises from 20.7 ° at 0.09 % moisture to 27.4 ° at 0.26 % moisture.

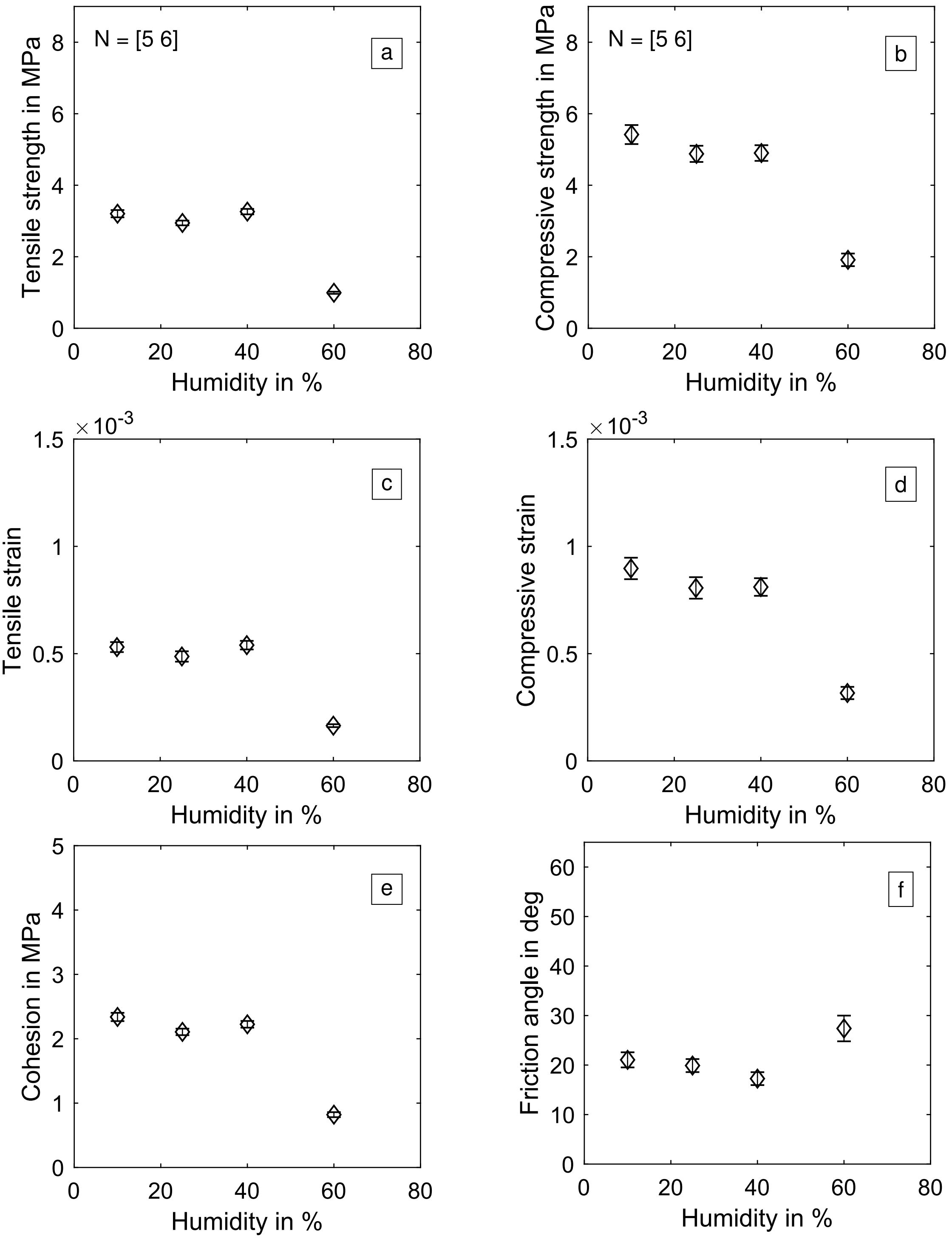

Figure 6.22: Tensile and compressive strength data for different storage humidity values. The fracture strain is calculated with Hook's law. Furthermore, the material cohesion c and the friction angle Φ are calculated.

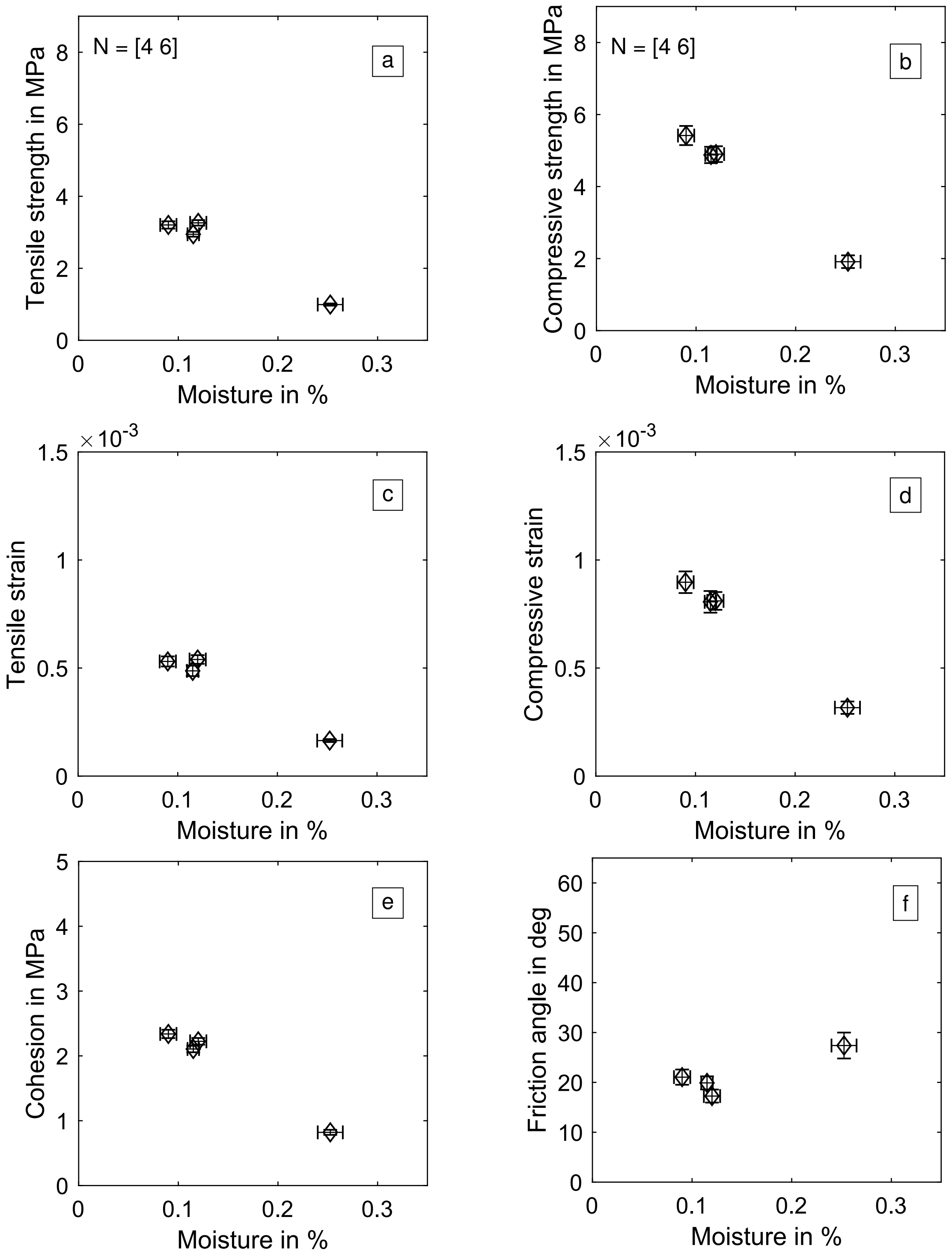

Figure 6.23: Tensile and compressive strength data for different moisture humidity values. The fracture strain is calculated with Hook's law. Furthermore, the material cohesion c and the friction angle Φ are calculated.

Discussion This means that the tensile stress is decreasing more than the compressive strength. As before, I theorise that the influence of the binder system on the compressive strength is smaller, since the compressive strength is influenced by the grain interactions, as well. The extreme case would be loose sand without binder. In the tensile direction, the strength is zero, while depending on the grain form and other parameters there can be considerable compressive strength.

The decreasing strength for sand-cores bound with sodium silicate is well supported by literature. However, most studies analyse the core strength over time at a constant humidity level. Griebel showed that the core strength of a similar sand-binder system decreases linearly with the storage time at 60 % humidity (Griebel, 2016). This is the humidity level which starts the increase of moisture in this section, as well. Therefore, the combined information of both data sets leads to the conclusion that the moisture is increasing linearly over time at a constant humidity level, which subsequently decreases linearly the core strength.

6.3.4 Comparison to an Organic Binder System

In this section, I will compare the most important characteristics of the failure surface of inorganic sand-binder systems with the organic system OR-2. In section 6.1 the results showed that both binder classes, organic and inorganic, followed the weakest link theory and have a Weibull distributed fracture behaviour. This builds the foundation for the development of the novel weakest-link-based Mohr-Coulomb criterion. Here, I will validate that organic sand-binder systems follow a Mohr-Coulomb criterion as well. As before, the goal is to differentiate between a possible Drucker-Prager and a Mohr-Coulomb failure criterion. Therefore, I performed the most important plane stress experiments with the system OR-2. The uni-axial and bi-axial compression experiments are suited best to differentiate between the Drucker-Prager and the Mohr-Coulomb criterion. Furthermore, I performed three-point-bending tests, which are necessary to calculate the model's parameters. The results are shown in figure 6.24. The individual experiments are depicted in grey dots, while the Weibull scale parameters are depicted in black. The pattern in the plane stress plot is very similar to the inorganic sand-binder system IN-1. As before, the bi-axial compression strength has an insignificantly higher absolute σ_2 component than the uni-axial compression.

Discussion Clearly, these results can be modelled with the weakest-link-based Mohr-Coulomb criterion, as well. The friction angle ϕ is 27.7° and the material cohesion c is 2.82 MPa. Of course, this is only one representative of the organic binder class. However, based on these results, I propose to model organic sand-binder systems in general with this failure criterion, due to the similarities which they have shown so far.

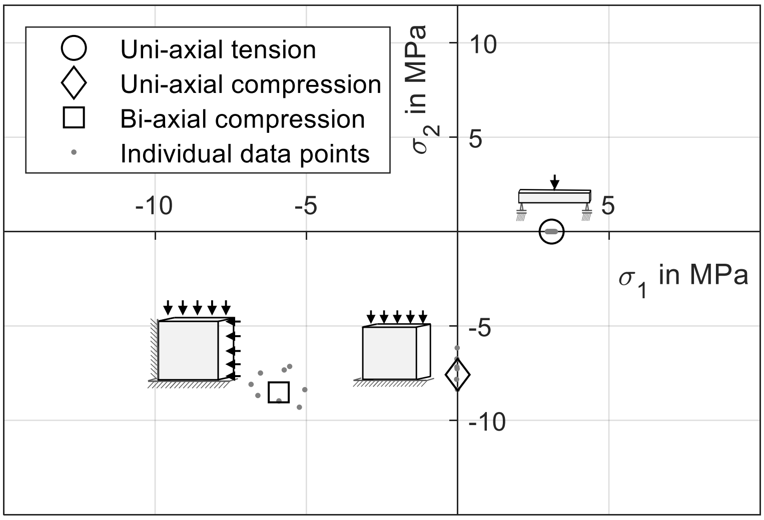

Figure 6.24: Plane stress experiments for an organic sand-binder system. The compression experiments with the sand-binder system OR-2 show a very similar pattern to the ones with an inorganic binder system.

6.4 Creep Characterisation

Up to this point, only brittle failure of core materials was considered in this thesis. For ideal brittle materials, all deformation is elastic until material failure occurs. No classical plastic deformation is possible, which results in a Weibull distributed fracture. However, I will show in the following section that core materials have a distinct creep behaviour under constant load below the fracture stress level, which results in inelastic deformation. Figure 6.25 shows an exemplary bending creep experiment with a specimen made with the sand-binder-system IN-1-2. The test setup and data evaluation for this experiment is described in section 4.2.7. The data starts as soon as the testing machine reaches the target load and holds it constant. Elastic deformations are disregarded. On the left side the strain is depicted over time, on the right side, the strain rate is shown. The three typical creep phases can be clearly distinguished. Phase one is characterised with a high strain rate, which is decreasing until it is nearly constant and phase two begins. The strain rate remains constant in phase two until the failure of the material begins, which marks the beginning of the third phase. Phase one and two can be described with the power creep law in equation 2.31. In the following, I will only consider the creep phases one and two, since the modelling of phase three is of little technical interest. The variables in the power creep law in equation 2.31 are the load time and the load level. The increasing time leads to the transition from phase one to phase two, while a higher load level increases the strain rate in both phases. Figure 6.26 shows a creep experiment at different load levels.

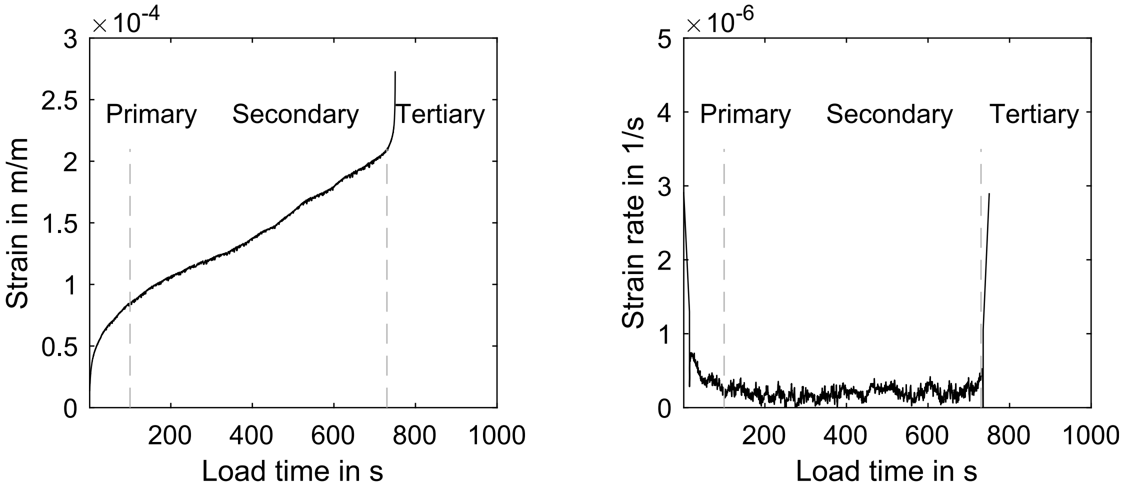

Figure 6.25: Creep experiment with constant load. The strain development for a bending experiment with constant load is depicted. The plot starts as soon as the target load is reached. The curve shows the typical three phases of creeping. On the right side the strain rate is presented.

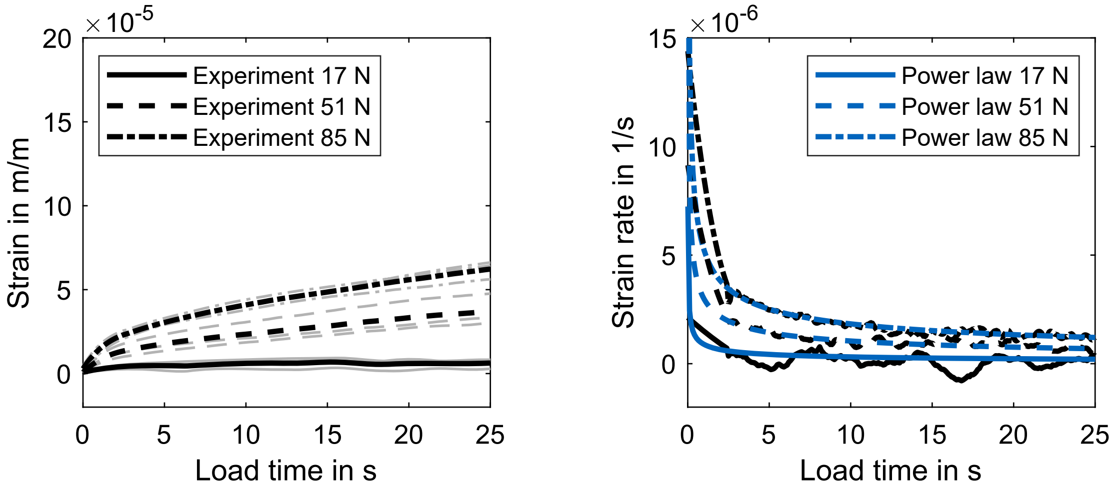

Figure 6.26: Creep behaviour for different load levels. The creep strain (left) and strain rate (right) development depend on the load level. On the left side, the individual experiments are depicted in grey, while the average curve is black. On the right side, the corresponding time derivative of this average strain curve is shown in black, while the creep power law fit is shown in blue.

Please note that the specimens were stored at 40 % humidity and 20 °C to imitate typical storage conditions. The specimens were constantly loaded with 17 N, 51 N, and 85 N. The fracture force of the specimens was determined to 170 N before the creep experiments. The individual experiments are depicted in grey on the left side, while the average for each load level is shown in black. The time derivative of this average strain curve is shown on the right side. Additionally, I fitted the power creep law to these data sets. The phase two strain rates are modelled well for all three load levels, while for the higher loads the strain rates are underestimated in phase one.

6.4.1 Influence of Storage Time

To study the influence of storage time, I determined the creep behaviour 20 s after tool opening. The results are shown in figure 6.27. On the left side, the calculated maximum strain in the specimens is depicted. Again, the individual experiments are shown in grey, while the average strain curve for each data point is shown in black. I determined the strain curve 20 s after tool opening with 32 N and 45 N load. The fracture force was determined to 122 N before the creep experiments. For comparison, the figure also shows measurements after 24 h of storage. The specimens with 24 h storage show a classical strain curve with a short phase one and a phase two with a near-constant increase of strain. In contrast, the strain curve has an entirely different characteristic 20 s after tool opening. The absolute strains are significantly higher and in the recorded 50 s time frame no constant strain rate is reached, which would be typical for the beginning of phase two. On the right side of figure 6.27 the strain rate of the two 20 s data sets is shown in black. Additionally, I fitted the classical power law to the data sets (dark blue).

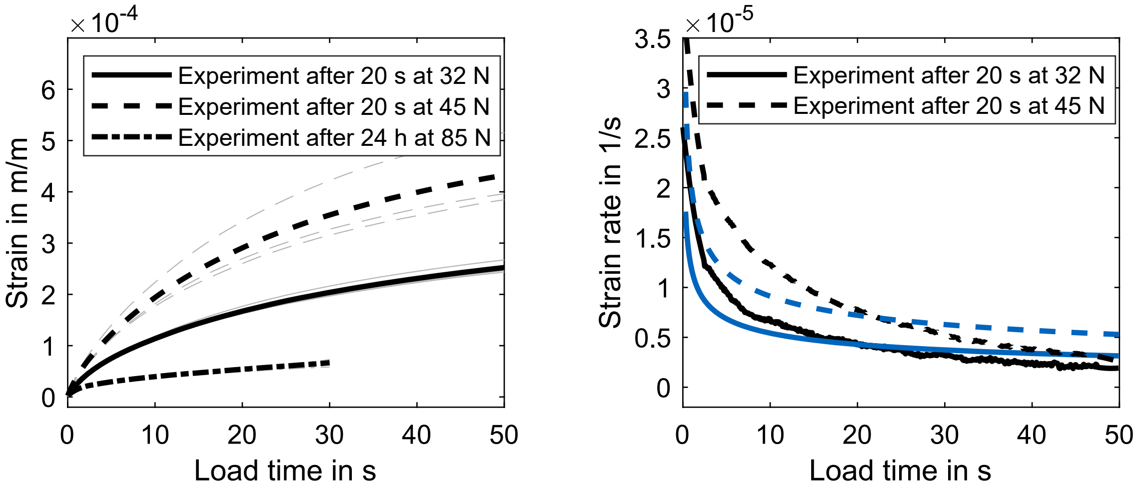

Figure 6.27: Creep behaviour 20 s after tool opening at 32 N and 45 N load. Immediately after the core shooting, the creep behaviour is more pronounced than after 24 h of storage.

The power law cannot model the creep behaviour properly in this situation. For both data sets, the power law underestimates the experimental strain rate during the first seconds. After approximately 25 s, the power law overestimates the strain rate. This is because of to the error minimisation of the fit. The power law is not able to mimic the curvature of the strain rate, thus the parameter are chosen such, that the model underestimates the strain rate in the first seconds, while it overestimates the strain rate after approximately 25 s.

Discussion In my opinion the reason for this discrepancy between the model and the experimental reality is the hardening process of the cores, which is still ongoing in the time span of the measurement. The core is still hardening and cooling down dynamically in the time span 20 s to 75 s after the tool opening, which results in changing creep behaviour during the measurement. The increasing material strength constantly changes the load level during the experiment, which cannot be modelled by the classic power law. Therefore, I analysed the model error by subtracting the experimental strain rate from the predicted strain rate. The result is shown in figure 6.28 on the left-hand side. For both experiments, the error function is similar to a logarithmic function. This is plausible, since the previous results showed that the hardening is a logarithmic process. Thus, I adapted the Norton-Bailey creep law by a logarithmic function:

$$\dot{\epsilon} = K \left(\frac{\sigma}{\sigma_0}\right)^n \left(\frac{t}{t_0}\right)^o + \beta_I + \beta_{II} \ln t, \tag{6.8}$$

where β_I and β_I are parameters of the logarithmic function. This adapted creep law leads to a significantly improved prediction of the strain rate, as shown by 6.28 on the right-hand side.

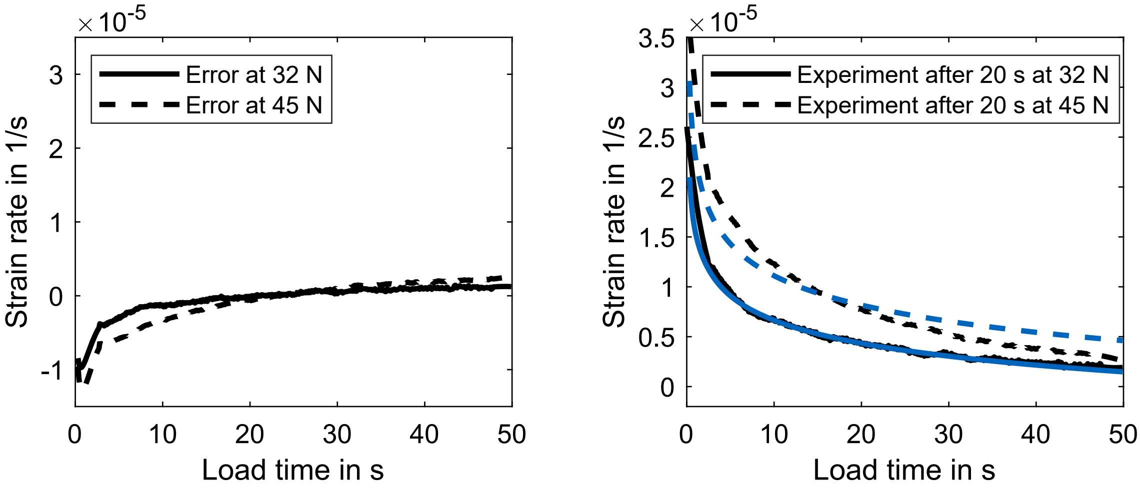

Figure 6.28: Model error of the classic Norton-Bailey creep law (left). On the right-hand side the experimental results of the strain rate (black) are shown in comparison to the adapted creep law (blue).

However, if the classical power law has to be utilised to calculate the creep deformation for a load case within a known time span in the first minutes after the tool opening, it is possible to estimate the creep deformation at the end of this interval, if the parameters are fitted to the same time frame in the parameterisation experiments.

6.4.2 Influence of Binder Amount

The influence of the binder amount on the creep behaviour is of paramount interest, since this knowledge allows to calculate the necessary amount based on the load cases the core is subjected to. The working hypothesis is that according to equation 2.31 the creep behaviour should remain constant if the ratio of stress and material strength (stress level) remains constant. To test this hypothesis, I produced specimens with the sand-binder-mixture IN-1-2 with 1.5 %, 2.0 % and 2.5 % fluid binder. The varying binder amount leads to varying material strength values. In section 6.3.2 the bending strength for these binder amounts have already been determined. Thus, the load forces at 40 % load level are 44 N (1.5 % binder), 87 N (2.0 % binder) and 92 N (2.5 % binder). Figure 6.29 shows the results of the creep characterisation. On the left side the creep curve is shown, while on the right side the respective strain rates are depicted. There is a small offset between the creep curves, because of differences in phase one.

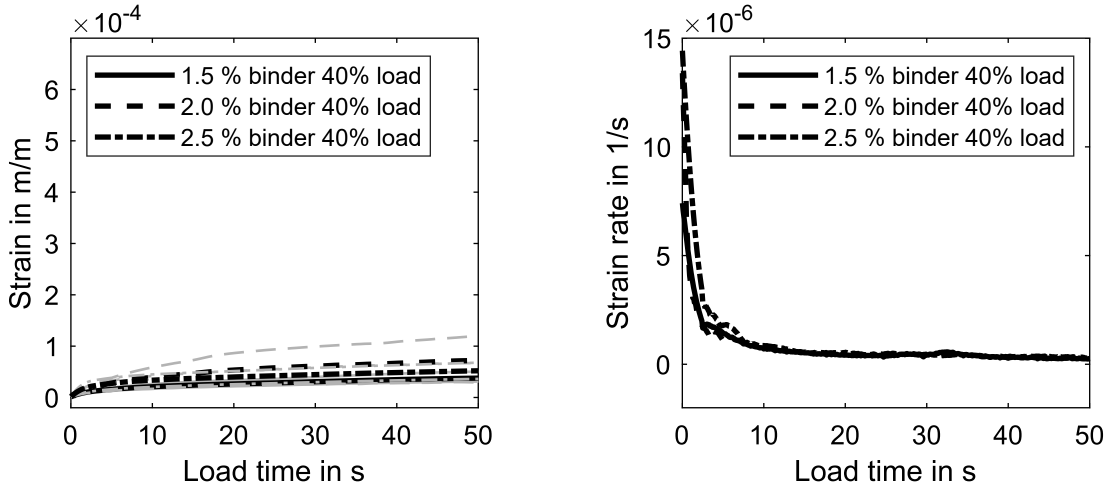

Figure 6.29: Creep behaviour for different binder amounts. If the load level is constant relative to the material strength, the strain and strain rate curves are very similar.

Discussion The scatter in phase one leads to an outlier for 2.0 % binder in the strain plot on the left-hand side, since small sand grains on the surface are flattened by the support. Subsequently, the phase two strain rates are approximately equal. Considering the scatter of the data, this difference in phase one is not significant and it can be confirmed that the creep behaviour depends on the load level and is independent of the binder amount. This is a valuable information, since the parameterisation effort in the future is significantly reduced, if it is sufficient to determine the material strength without additional creep tests for different binder amounts. Furthermore, this leads to the conclusion that the effective loaded volume is relevant for the creep behaviour as well, since the effective volume determines the fracture stress of a core as shown in section 6.1. Thus, the relative load level depends on the effective volume, as well.

6.4.3 Influence of Humidity

Analogously to the binder amount, I varied storage humidity to study the influence on the creep behaviour. Specimens produced with the sand-binder-system IN-1-2 were stored at 10 %, 40 % and 80 % humidity. The specimens were subjected to a 50 % load level in the three-point-bending experiment. Figure 6.30 shows the results. The individual strain curves are depicted in grey on the left side, while the average curves are featured in black. As before, the curves are very closely grouped and the difference is insignificant compared to the relatively high scatter. The corresponding strain rates on the right side of the figure are also approximately equal, considering the scatter of the data and the noise from the numerical differentiation.

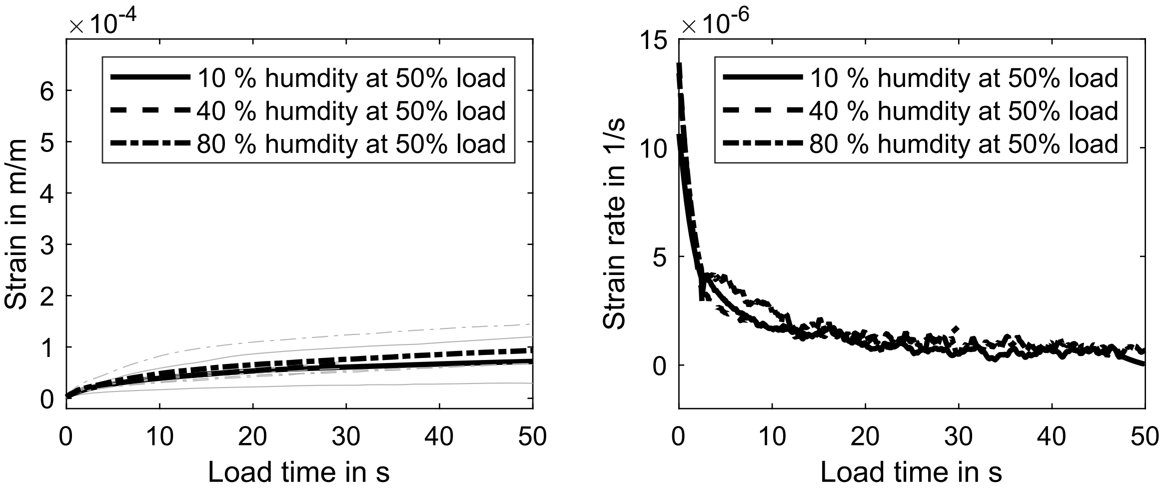

Figure 6.30: Creep behaviour for different humidity levels. The strain and strain rate curves show that the creep behaviour is independent from the humidity level, if the load is normalised with the fracture strength.

Discussion Evidently, the increased humidity is not influencing the creep behaviour besides reducing the material strength of the specimens. Again, this confirms the validity of the load level hypothesis and reduces the parameterisation effort considerably.

6.5 Discussion of Consequences for Industrial Core Production

In the following, I will discuss the application of the results regarding the failure behaviour for the life cycle of foundry cores. Figure 6.31 shows the life cycle of the foundry cores and the processes, which are relevant for the proposed methods and results. The results of this thesis are directly applicable to the transport processes and the storage of the cores (dark grey), while the proposed methods can be applied up to the decoring for material characterisation (light grey). However, new parameter sets will be necessary after the casting, since the high temperature of the melt is changing the material behaviour considerably, which was not studied in this work.

In the following, I will focus on three topics: The effort necessary to parameterise a failure model, the creep behaviour and the boundary conditions of typical technical processes during the life cycle of a foundry core. These three topics are the most essential for future FEM calculations with core materials.

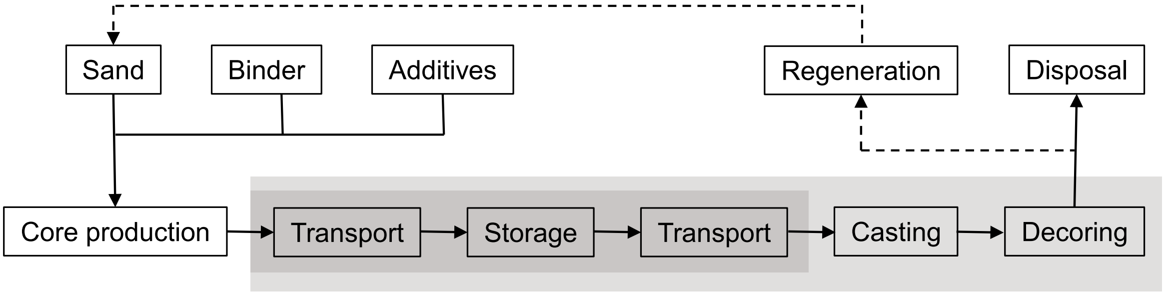

Figure 6.31: Overview of the foundry core life cycle. The processes which can be modelled with the results of this thesis are marked grey. (after Ettemeyer et al., 2021

Material modelling and parameterisation effort Assuming that other commercial binder systems have the same failure characteristic as the ones tested in this thesis, I propose to characterise the failure of such core materials with the weakest-link-based Mohr-Coulomb criterion described with equation 6.6 in the future. Only two experiments are necessary to parametrise a Mohr-Coulomb model. A bending and a uni-axial compression experiment suffice. The other experiments I performed in this chapter were necessary to systematically validate the failure surface. Now only the minimal data amount is necessary to safely calculate the parameters of the model. The bending experiment is the standard experiment for quality control in industrial core production and is routinely performed anyway. The additional compression experiment can be performed on the fractured parts of the bending beam.

Furthermore, the elastic parameters can be determined non-destructively with the same set of specimens before they are used for the three-point-bending test. This test methodology is not increasing the number of specimens, since there usually is a quality inspection with three-point-bending experiments in core production anyway. However, the number of tests per specimen is considerably increased and the gained knowledge with it. The tests I proposed yield the Young's modulus, the shear modulus and a prediction of the complete failure surface, instead of the bending strength as the only material parameter. This knowledge allows to parametrise a complete material model for a FEM simulation to predict core fracture without creep influence.

For characterising the failure surface it is valuable information that the material's cohesion parameter is increasing linearly with the binder amount and the friction angle remains constant. This allows a true dimensioning process, which determines the minimum amount of binder which is necessary to sustain the load case at hand. Furthermore, the logarithmic hardening allows to calculate the material strength for any time in the life cycle of the core, if the failure surface is determined at two points in time (e.g. immediately after production and after 24 h).

Boundary conditions There are two types of load boundary conditions, which can be mechanically imposed on cores. There are force or pressure loads, which are constant and approximately independent of the resulting deformation. These belong to the category of Neumann boundary conditions. A pneumatic gripper system would be an example for that kind of boundary condition. The pressure to the core is constant as long as the actuator is not in one of its limits. The second type of boundary condition is an imposed deformation. This applies to processes, which do not induce a controlled force into the core but a fix deformation. These boundary conditions can be categorised as Dirichlet conditions. One example is the contact between the steel mould and the cores. Typically, steel moulds consist of multiple parts which are closed for casting. The cores are placed inside the mould in designated supports, which are called core prints, which hold the core in place. If there is a tolerance problem with the core, the mould is deforming the core through its supports. The fracture strain of the material in the current ambient conditions is determining whether the core fractures. With the methods I introduced in this dissertation, it is possible to determine the fracture strain for worst case ambient conditions. I showed that the fracture strain is decreasing significantly with increasing humidity. If the geometrical tolerances of the produced cores are known, it is possible to determine for which ambient conditions there will be increased core fracture.

Depending on the boundary condition it is valuable to monitor the ambient conditions and process parameters to consider their influence on solely the fracture stress (Neumann condition) or the fracture strain (Dirichlet condition).

Creep Modelling For constant loads, it is essential to determine the creep parameters. In industrial production, any considerable deformation leads to a rejection of the core and has to be prevented. Therefore, it is important to analyse the sand-binder system in question in a parameter study for it's most important influences and define worst-case limits for the constantly applied stresses. In this work, I have shown that the creep behaviour is dependent on the relative load level, which is the ratio of load and material strength. The fundamental creep parameters do not change, if the humidity or the binder amount changes and the relative load remains constant. It is beneficial to normalise the creep loads with the absolute bending strength, since it allows to calculate the creep behaviour with a known material strength without further experimental effort.

Based on the failure surface and the influence of process parameters on the material strength, it is possible to optimise handling and storage processes to minimise the creep deformation. For example, a water jacket core which is stored for a given time is deforming due to its own weight. This load case can be simulated and adapted such that the component will have no significant creep deformation, due to the near exponential decline of creep with decreasing stress levels. It is possible to either increase the material strength with a higher binder amount or to optimise the storage support to reduce the load level. Thus, a true dimensioning process in a FEM simulation becomes possible for creep problems.

7 Validation

In this chapter, I will validate the weakest-link-based Mohr-Coulomb failure surface described with equation 6.6. There will be two validation geometries with complex stress states. The first validation geometry is an adaption of the Brazilian test, which induces complex stress states into a cylinder. The second validation test is a complex water jacket core. The general idea is to predict the fracture force of the specimens with complex stress states based on the material characterisation with uni-axial bending and compression experiments. This prediction will be performed with an FEM analysis, since an analytic solution is not possible. Additionally, the experiments will be performed in reality and the results will be compared. The specimens for the Brazilian test were produced with the organic sand-binder system OR-2 and the inorganic system IN-1-2. The water jacket cores were produced with the IN-1-2 system.

7.1 Brazilian Test

A Brazilian test is utilised as the first validation experiment for both inorganic and organic binder systems. The test is performed with specimens of type IN-1-2 and of type OR-2. The Mohr-Coulomb model is fitted to data sets consisting of three-point-bending and compression experiments as proposed in the previous chapter. The test setup described in section 4.2.6 is used and the stress field is calculated with the FEM simulation detailed in section 4.3.6. I compare the fracture force of the experiment with the predicted fracture force according to several material models. The following models will be utilised:

- A classic Mohr-Coulomb model without volume scaling as proposed by Stauder (Stauder et al., 2019).
- A classic Drucker-Prager model without volume scaling as proposed by Thorborg (Thorborg et al., 2020).
- The weakest-link-based Mohr-Coulomb model with volume scaling as proposed in chapter 6.

The results of the FEM analysis are shown in figure 7.1. The three major components of the Cauchy stress tensor are compared to an image of the upper half of a fractured specimen for a load of 2 kN.

The effective volume is calculated from the exported principal stresses and volumes of the individual elements with equation 6.7 for the calculation of the fracture force with the novel weakest-link-based Mohr-Coulomb criterion. Figure 7.2 shows the test results for the experiment and the three failure criteria on the left side. For both sand-binder systems, the classical Mohr-Coulomb criterion is significantly underestimating the material strength. The classic Drucker-Prager criterion is underestimating the fracture force, as well. In contrast, the weakest-link-based Mohr-Coulomb criterion predicts the fracture force considerably better.

Discussion The effective volume of this load case is smaller than the effective volume of the three-point-bending experiment. Therefore, the material strength is scaled up for the Brazilian test in case of the weakest-link-based Mohr-Coulomb criterion. Evidently, this scaling is necessary to accurately predict the fracture force for both binder systems. The complex stress state in figure 7.1 confirms that it is not possible to analytically calculate a tensile fracture force as typically done in the state of the art literature. The compression stresses in component σ_{yy} are significantly higher than the tension stresses in component σ_{xx}. Both stress components are symmetrical. Furthermore, there is a considerable shear stress component σ_{xy}. The course of

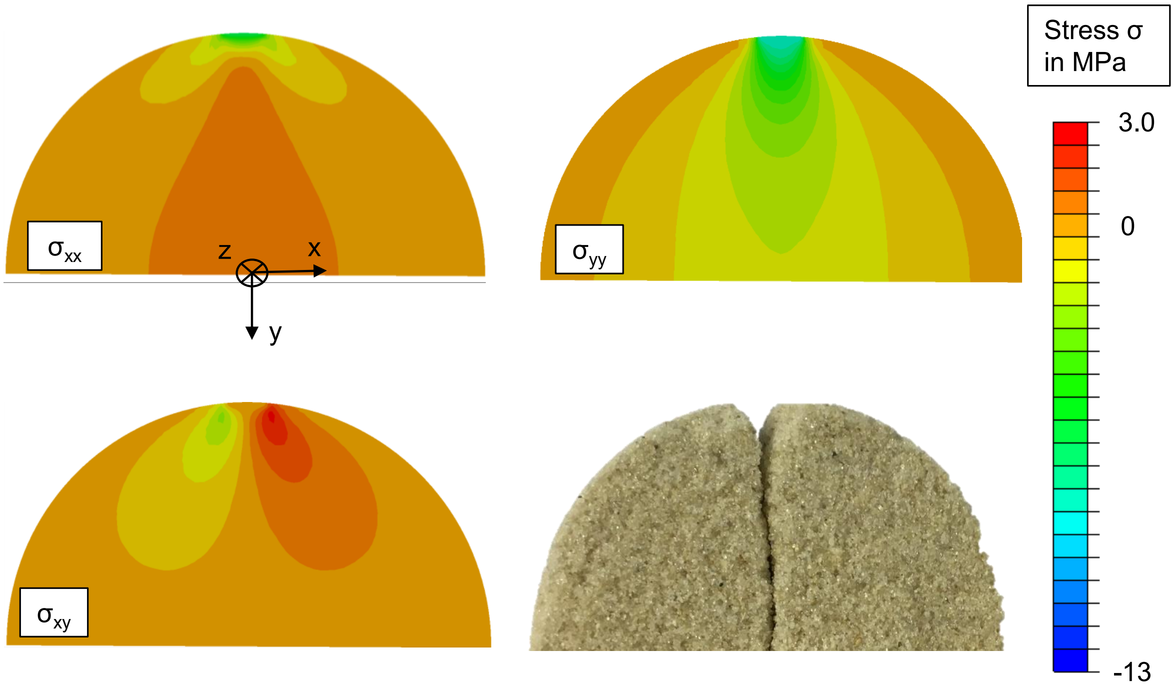

Figure 7.1: FEM results for the brazilian test for a load of 2000 N in comparison with a fractured specimen. Half of the cylinder is shown for comparability to the simulation. The stress peaks in all three components are reflected in the course of the fracture. The shear component σ_{xy} builds the triangle shaped gap, while the rest of the fracture follows the symmetric stress fields of σ_{xx} and σ_{yy}. (Lechner, Hartmann et al., 2021)

the fracture of the specimen reflects these stress fields. The triangular gap in the σ_{xy} stress field near the load leads to an analogous gap in the fractured specimen. Four separate parts remain of the specimen after the experiment. The two bigger halves in the image and two triangular parts, which fit in this gap. This indicates that the fracture is induced in these symmetrical shear stress peaks. The fracture then follows the maximum of absolute stress in the axis of symmetry. For a more in-depth analysis, the three failure criteria for a plane stress load case are depicted in figure 7.2 on the right side. The parameters of the OR-2 specimens are utilised in this figure. Additionally, I plotted the σ_2 and σ_3 principal stresses of every element in the model for two load levels. I chose the principal stresses σ_2 and σ_3, since they reflect the two main compression components, while σ_1 has a much smaller absolute value and is therefore neglected in this figure, which is limited to two dimensions.

The Drucker-Prager model predicts the fracture of the OR-2 specimens at 1650 N. The stress states of every element at this load force is depicted in dark grey. The specimens actually fractured at a Weibull scale parameter of 2610 N, which is depicted in light grey. At 1650 N the classic Drucker-Prager model predicts the fracture and it exactly touches the dark grey elements

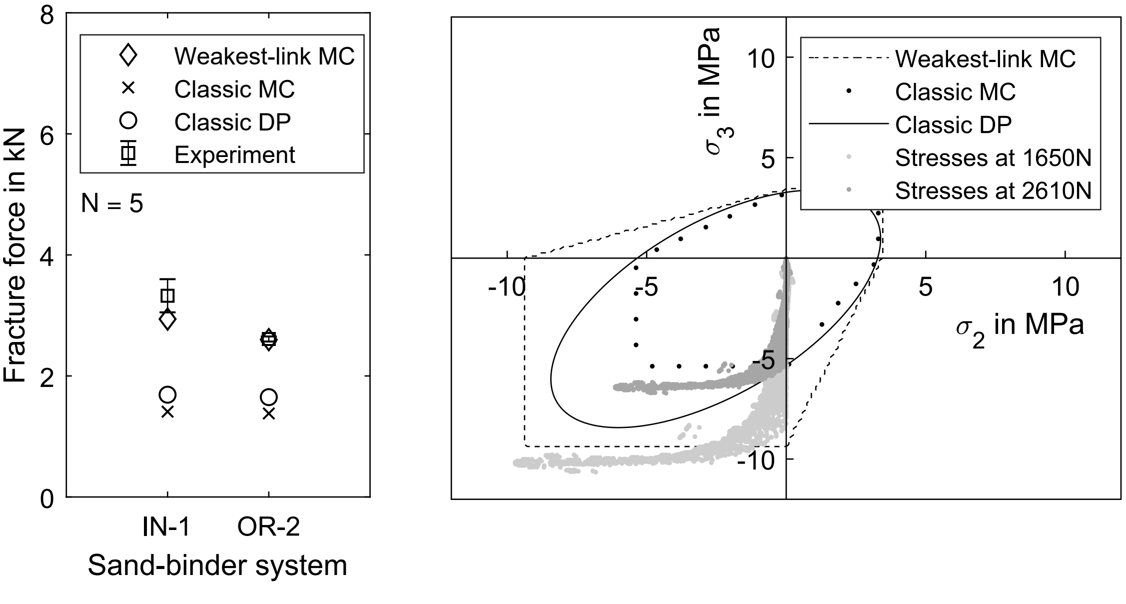

Figure 7.2: Brazilian test as validation for the new weakest-link-based failure criterion. The validation was performed with one inorganic and one organic sand-binder-system. On the right side, the two major principal stresses for every element in the FEM model is shown for the OR-2 system. The load 1650 N (dark grey) represents the predicted fracture force of the Drucker-Prager criterion, while the load 2610 N (light grey) is the experimentally obtained fracture force. (Lechner, Hartmann et al., 2021)

near the uni-axial stress states. The classic Mohr-Coulomb model predicts the fracture earlier and the fracture is likely induced by a bi-axial stress state. However, both classic criteria predict the fracture force significantly lower than the actual force determined in the experiments. This load level is represented in light grey and can be compared to the weakest-link-based Mohr-Coulomb model, which considers volume scaling. It underestimates the fracture force as well, but fits significantly better to the results than the other two models. This analysis shows that the fracture in these Brazilian tests is induced by a bi-axial compressive stress state. In my opinion, the remaining underestimation of the fracture force is due to the failure surface shown in chapter 6. For both binder classes the bi-axial stress states have a slightly higher compression strength than purely uni-axial compression experiments. This can not be modelled properly by a Mohr-Coulomb model which assumes that the maximum compressive strength remains constant if a second compressive component is added. This leads to the observed underestimation of the fracture strength for bi-axial compression states. Figure 7.2 shows that this model error has a similar absolute value as the scatter in the data. Therefore, the prediction is accurate enough, in my opinion. If the model prediction has to be more accurate, the bi-axial compression strength can be utilised to parameterise the yield criterion.

7.2 Water Jacket Core Test

As a second and more complex validation experiment, I utilise a three-cylinder water jacket core geometry. The cores were produced with the sand-binder system IN-1-2 with 2 % fluid binder. Due to the dimensions and the number of water jacket cores, they could not be stored for 24 h in a climate chamber, but remained in room conditions. To ensure, that the material parameters are consistent, specimens for material characterisation were stored with the water jacket cores and tested shortly before the water jacket cores. The cores were subjected to three different load-cases, as described in figure 4.21. The simulation of the load-cases is performed analogously to the experiments, as detailed in section 4.3.7. The simulation in Abaqus is purely elastic with increasing load steps of 5 N. Subsequently, the principal stresses and volumes of every element are exported to Matlab, where the data is analysed for fracture according to the failure surface detailed with equation 6.6. The effective volume is calculated at the same time with equation 6.7. The results of the bending and the compression experiment, which are utilised to parametrise the material model are scaled to this effective volume. The predictions and experimental results for all three load-cases are shown in figure 7.3. Figure 7.4 shows the results of the elastic simulation at 10 N load. Since the Mohr-Coulomb model can not be depicted in one coloured scale, I showed the maximum shear stress on the left side and the hydrostatic stress on the right side. For all three load cases, the hydrostatic stress is not significant with the exception of load case three, where one peak has close to 1 MPa hydrostatic stress. The absolute maximum shear stress level differs from load case to load case, which will be reflected by different fracture forces in the following. The results of the data post-processing in Matlab and the fracture forces are predicted with the weakest-link-based Mohr-Coulomb failure criterion.

Discussion There is good agreement between the simulation and the experiment, which shows that the material model is suitable to predict fracture forces for complex core geometries. Figure 7.5 shows a comparison of the fractured specimen for load case one and three to the FEM results. The fracture locations coincide with the stress peaks in the FEM results. The specimens of load case two fail in a manner which makes it difficult to find the fracture origin.

In my opinion, it is now validated that the failure model developed in this dissertation can be applied to real core geometries and predict their fracture. For example, this simulation can be utilised for a handling simulation of the water jacket core, where it is subjected to forces from the gripper and from the acceleration of a handling system. Furthermore, it shows that the previous methods can be applied not only to simple test specimens, but also to complex foundry cores.

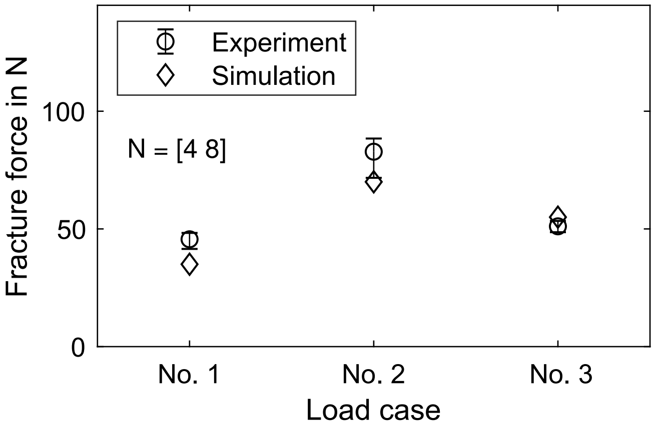

Figure 7.3: Fracture forces of the water jacket core for various load cases. The experimental results are marked with circles, while the simulation results are indicated by diamond symbols. The scatter in the experimental data is indicated with minimum and maximum values. (Lechner, Stahl, Hartmann et al., 2021)

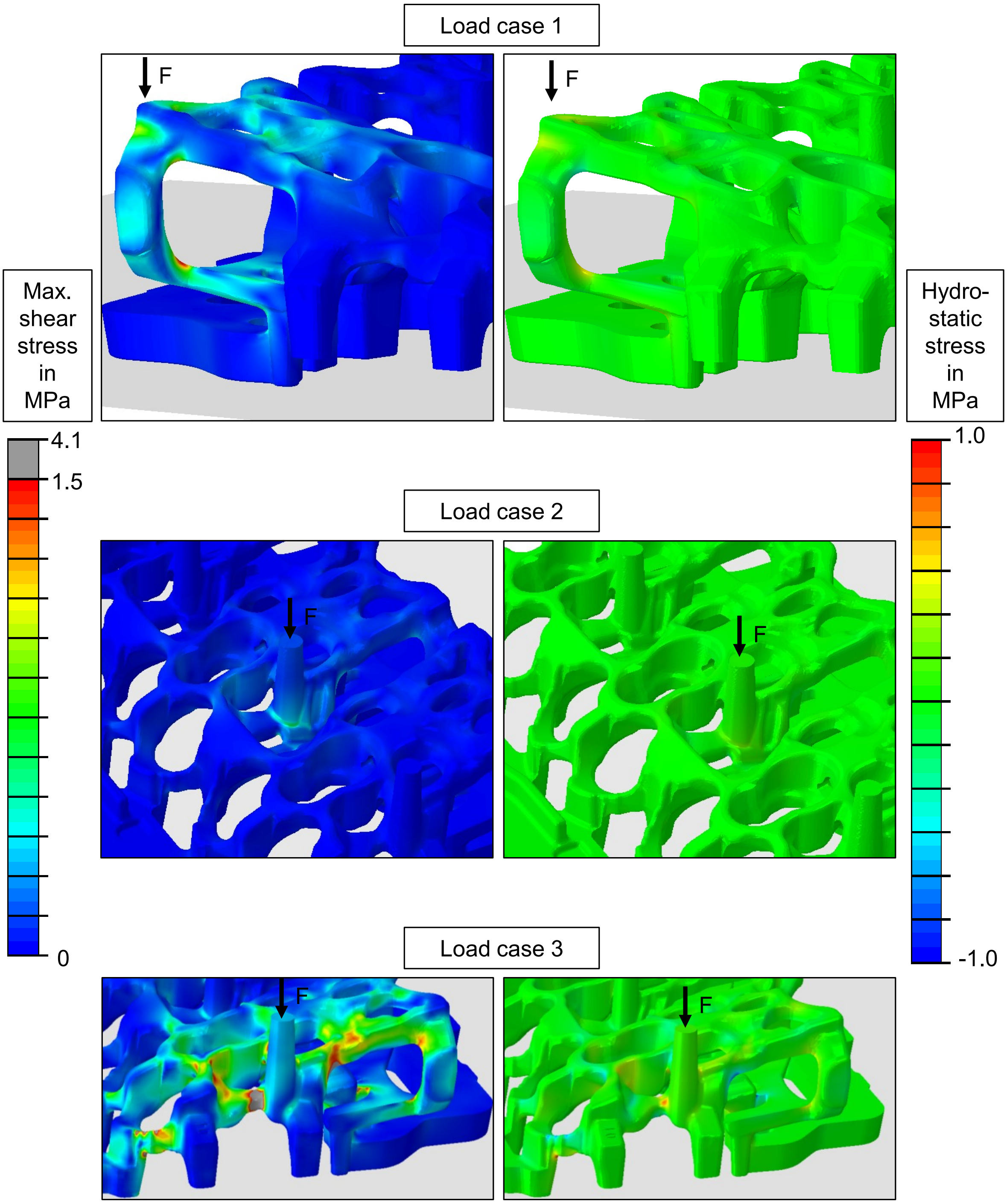

Figure 7.4: FEM results of the water jacket core for all load cases at 10 N load. On the left side the maximum shear stress is depicted, on the right side the hydrostatic stress. Both are important influences on the Mohr-Coulomb failure criterion, which determine the material strength. (Lechner, Stahl, Hartmann et al., 2021)

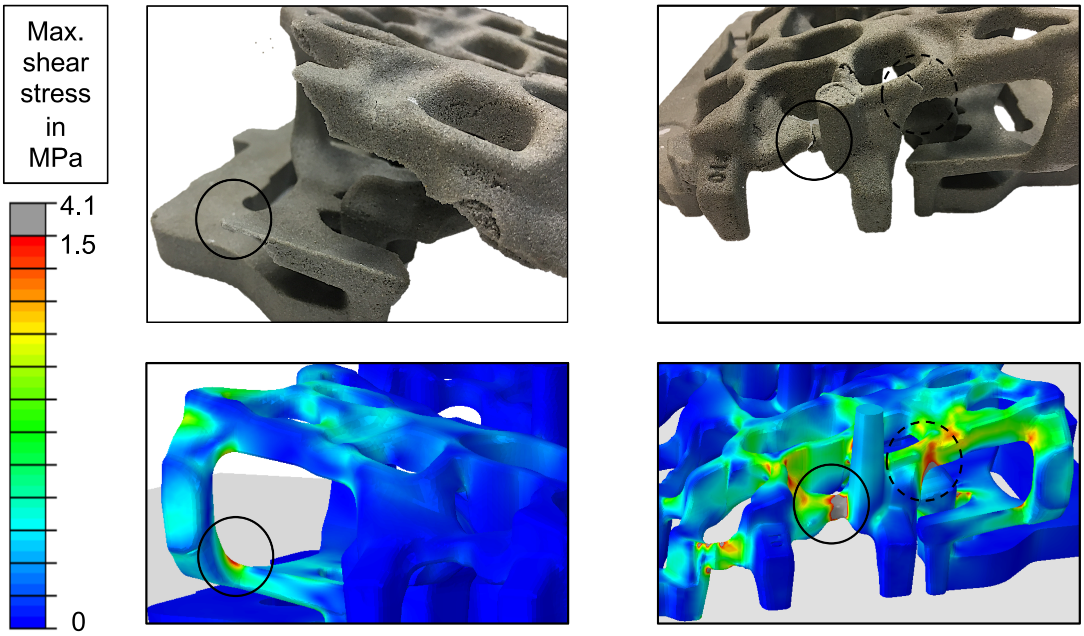

Figure 7.5: Comparison of fracture locations and stress peaks. Two examples of fractured specimens are depicted in the top row for load cases one and three. The fracture locations are marked with black circles and correspond well to the stress peaks in the FEM calculations. (Lechner, Stahl, Hartmann et al., 2021)

8 Application in an Industrial Environment

In this chapter, I will show how the results of this dissertation can be applied to solve engineering problems in industrial core production with an example from the core manufacturing at the BMW AG foundry in Landshut. It is structured as a case study, which describes the problem, the utilised simulation model and discusses the results.

8.1 Motivation and Problem Description

Today's core development is based strongly on the experience of the involved developers and previous successful core developments. The amount of binder, which is utilised in the core is estimated and finally quantified by a trial and error process. Two factors mainly influence the decision for the binder type and amount: the hot strength during the casting and the necessary handling strength from the core shooting machine to the mould. The necessary handling strength defines the absolute minimum of binder in the core, while the hot distortion during the casting may add additional requirements.

Handling systems for the cores are developed analogously. New gripper systems are devised based on successful components, which have not damaged its respective core. In contrast to other engineering materials and components, it is not state of the art to simulate the handling stresses with FEM. The results in this dissertation enable a true dimensioning process. A digital twin of the handling processes can be developed and utilised for process optimisation. After the simulations, the minimal necessary core strength is known and the binder amount can be calculated with a simple regression and reduced if enough hot strength during the casting remains. Additionally, it is possible to optimise gripper systems to reduce stresses in the cores. Both calculations have the potential to save binder, which has a direct economical and ecological benefit.

One of the most challenging processes of the casting with inorganic cores is the decoring (Izdebska-Szanda et al., 2012, Stauder et al., 2018b). The optimisation of the binder amount also reduces process time and energy during the decoring process, since a lower binder amount lead to a lower remaining core strength after casting.

As an example for an industrial application, I chose the automatic handling of a six cylinder top core at the BMW AG foundry in Landshut. The core is picked up by a robot directly after the core shooting. The first gripper, which was utilised by BMW AG for this application is shown in figure 8.1 with the core in its intended position. The gripper consists of a frame with two pneumatic linear actuators on one side and a support on the other side. The force is applied on the sides of the core. Please note that they are not orthogonal to the direction of the pneumatic elements, since there are mould drafts on each side. Therefore, the pneumatic elements tend to push the core out of the gripper (in z-direction). This is prohibited by elements marked with black circles in figure 8.1, which act as support for this force.

According to the local foundry core specialist at BMW AG the gripper had to be changed, since the cores were deformed due to the high gripping force necessary. This deformation was determined externally at BMW AG in Landshut with a GOM ATOS system. In the following, I will perform a simulation of the gripping process as an example, how the results of this dissertation can be applied to core handling problems in the industry. The goal of the following simulation is to replace the trail and error process, which can save development time and resources in the future.

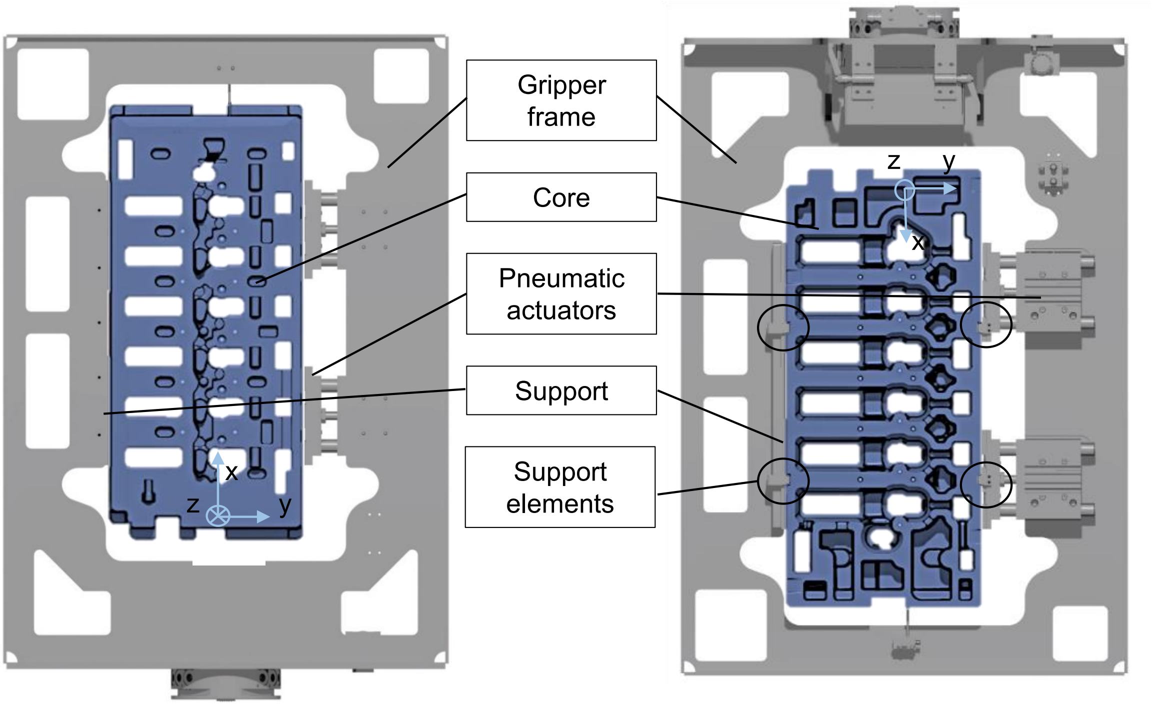

Figure 8.1: Front and back side of a gripper with a BMW AG top core. The gripper has two pneumatic actuators, which fixate the core. This gripper system leads to deformed cores, which violate the specified tolerances.

8.2 Boundary Conditions

First, the boundary conditions and process parameters have to be investigated. The force on the core is defined by the pressure on the pneumatic elements. The pressure in the system was quantified by BMW AG to be 0.2 - 0.3 MPa (2-3 bar). Therefore, the force applied by each pneumatic element was estimated to be 1 kN, based on the dimensions of the pneumatic elements and a pressure of 0.3 MPa. I simplified the problem by replacing the physical gripper system by boundary conditions on the core. All boundary conditions are depicted in figure 8.2. I modelled the six contact interfaces of the pneumatic elements with boundary conditions which support the core in x and y-direction and allow movement in z-direction. The force is applied on the two opposing surfaces on the other side of the core as surface pressure. This is the side of the core, which is supported in the gripper, not the side which is in contact with the actuators.

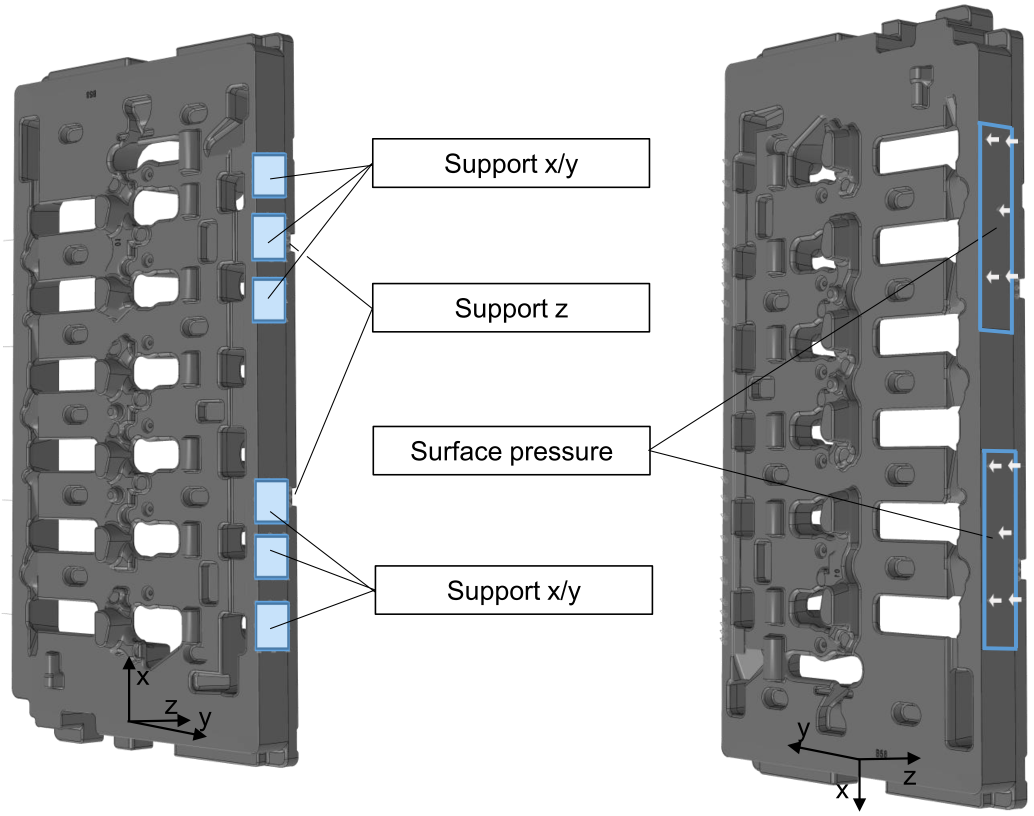

Figure 8.2: Boundary conditions of the mechanical simulation of the BMW AG top core load case. The supports in x and y-direction are fixed surface elements, where the contact to the gripper system is located. The support in z-direction is provided by fixed surfaces, where the support elements are placed. The load is induced by a Neumann (surface pressure) boundary condition.

I chose to invert the application of pressure, since it offers more insight into the gripper system later. Finally, the elements, which prohibit the sliding of the core in z-direction are replaced by supporting boundary conditions in z-direction.

After core shooting, the load is applied to the cores two times. They are picked up after the core shooting tool opens and placed into a system, which removes burrs. Afterwards it is transported to storage. I estimated the time of the first pick to be 2 s after tool opening. The gripper applies its force for 13 s. It remains in the deburring station and 89 s after tool opening, it is picked up for another 17 s. In the following, this analysis will focus on these two load cycles.

8.3 Material Model

As a second step, the core material has to be characterised. The BMW AG uses an Inotec binder-system which is very similar to the inorganic system used in this dissertation (Weissenbek et al., 2011). However, the cores are produced with different shooting parameters. Due to limitations in the utilised tool heating, it is only possible to produce specimens with a tool temperature which is 40 °C lower with the core shooting machine at utg. The hardening time was chosen according to the production parameters of BMW AG. In my opinion, the material parameters will be sufficiently close to reality at BMW AG to enable an estimation of the observed deformations. This assumption is supported by experiments performed by Izdebska-Szanda et al. They hardened a sand-binder system with sodium silicate at 100, 240 and 300 °C and found only insignificant differences in mechanical strength between the samples hardened at 240 and 300 °C (Izdebska-Szanda et al., 2008). The original tool temperature is within this temperature interval. To obtain material parameters similar to the real load case, I measured the strength and creep parameters as close to the tool opening as possible. The tests on the universal testing machine started about 15 s after tool opening. To be as close to the original load case as possible, I utilised a compression experiment to quantify the material parameters including the creep characterisation. Furthermore, I did not shorten the original specimens, but used it as a whole for the compression experiment. This has two advantages: The test can start closer to the tool opening, since no further processing of specimen is necessary and it resembles the original load case of the gripper. Therefore, the compression test setup is loading a defined area of the specimen, while the rest of the specimen remains without load. This test setup was utilised for compression strength and compression creep tests. I determined the creep behaviour for 0.44 MPa and 0.70 MPa compressive stress to quantify all three parameters for the Norton-Bailey creep law in equation 2.32, analogous to section 6.4. Furthermore, I determined the compression strength at two points in time. At 15 s after the opening of the tool and at 150 s. These results were utilised to fit a two parameter logarithmic regression:

$$\sigma = \beta_I + \beta_{II} \ln t, \tag{8.1}$$

where σ is the fracture stress and t the time after tool opening. β_I and β_{II} are constants. This regression was utilised to calculate the material strength at different points in time. Namely, the two points in time when each of the gripping processes start (2 s and 89 s relative to the tool opening). According to equation 2.31 the proportional creep parameter K can be scaled for different material strength values. Furthermore, the estimated material strength of the top core needs to be scaled according to its effective volume due to its Weibull fracture statistics. Therefore, I calculated the material strength values and creep parameters of the specimen at 2 s and 89 s after tool opening and scaled them to the effective volume of the top core. Additionally, I utilised the elastic parameters of section 5 and calculated the estimated Young's modulus at the two points in time with a regression as proposed in section 5. With all creep parameters, the material strength and the elastic parameters, the material model is complete and the core's behaviour under load can be calculated. The geometrical model is meshed with approximately 350000 elements of type C3D10 (Dassault Systems, 2020) for this calculation.

8.4 Results and Discussion

I simulated the core with two objectives. In a first step, I calculated the stresses and evaluated them with the Mohr-Coulomb model proposed in chapter 6 2 s after the tool opening. The results show that no core fracture will occur according to the Mohr-Coulomb model. The fracture probability, which can be calculated with equation 6.6, is close to zero. However, this is not surprising, since BMW AG described the problem as deformed cores, not fractured cores. The false colour images of two deformed cores, which were acquired by BMW AG with a GOM Atos system, are shown in figure 8.3 top and middle (specimen A and B). False colour images describe deviation relative to an orthogonal axis on each surface point of the CAD model. If the measured point is exactly on the surface, the deviation is zero. For positive deviations the measured point is outside of the CAD part, for negative deviations the measured point is inside of the CAD part. This type of deviation measurement is very sensitive to the registration of the measured point cloud relative to the CAD part. Therefore, the registration has to be exactly the same in order to compare two parts. Another possibility is to calculate relative deviations between two points, which compensates for constant offsets.

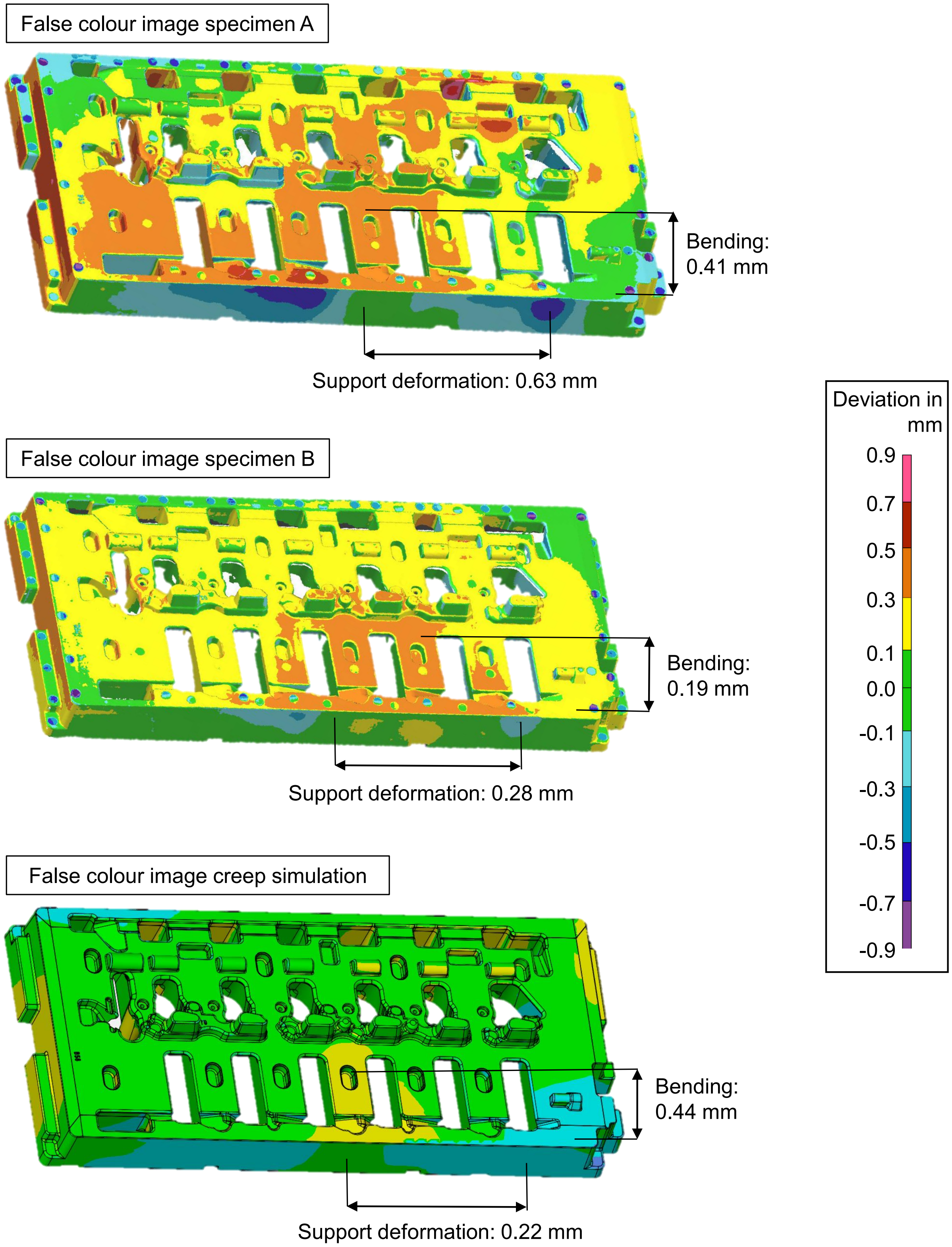

Figure 8.3: Comparison of optical measurement and simulation of the top core deformation. The simulation predicts both deformation patterns correctly.

I will focus in the following on two main deformation patterns. The first one is the deformation of the core's sides due to the contact to the grippers support. This deformation is up to 0.63 mm for specimen A and up to 0.28 mm for specimen B. This deformation is determined as a relative difference of the absolute deviations between the two black lines to compensate for small differences in the registration algorithm of BMW AG and the one I performed for the simulation results. The second deformation pattern is a bending of the cores. The middle of the cores are deformed such that positive deviations occur. I quantified this bending in a relative manner as well and specimen A has a deviation of up to 0.41 mm and specimen B of up to 0.19 mm.

The fact that the cores show inelastic deformation is a strong indicator for creep during the process, since creep is the only known mechanism, which results in inelastic deformation. Thus, I performed creep simulations in the next step. Since there are two gripping cycles at different points in time, I performed two simulations. One starts at 2 s after tool opening with the material parameters calculated for that point in time. This gripping cycle lasts for 13 s. The second starts at 89 s after tool opening and lasts for 17 s, which is simulated with the respective parameter set, as well.

The results of a FEM simulation in an absolute coordinate system are very difficult to compare to the results of an optical measurement represented by a false colour image, since the coordinate systems differ. Therefore, I exported the calculated deformations for each node and transformed the deviations into a false colour image. Since the deviations of the two gripping cycles are added by the optical measurements, I added the deformations calculated by FEM to one false colour image, as well. The deformations are small compared to the whole core, which allows to neglect the effect of the first gripping cycle on the second.

The resulting false colour image is shown in figure 8.3 as well (bottom) to directly compare it to the measurements. Both main deformation patterns are predicted by simulation. The relative bending is 0.44 mm and the maximum support deformation is 0.22 mm. Comparing the values of the simulated deformation to both specimens individually, it becomes apparent that the deformations are similar but not exactly as predicted. There are several possible reasons for this, which I will discuss in the following:

- The simulated results are based on mean material parameters, while two measured specimens do not offer a valid sample size. The two specimens differ from each other in a similar amplitude as the simulation differs from the measured parts. For a real quantitative comparison, a bigger sample size would be necessary.

- The material parameters are a result of interpolation and extrapolation utilising regression models. The parameters cannot be determined more accurately due to the dynamic process. Furthermore, it is too much effort in an industrial working environment to parameterise a material model for each process simulation. In contrast, the regression models offers a fast and affordable solution and a flexible material model.
- The deviations in the simulation are smoother in general. In particular, the support deformations are more constant over the affected area than the ones in the real cores. This indicates that in reality the gripper support is not distributing its pressure equally over the whole contact area. There is no mechanical reason for the deep grooves, if the pressure is equally distributed. Therefore, the pressure in the boundary conditions of the simulation is too smooth.

However, the results are accurate enough optimise the gripping process. This example shows that it is possible to predict problems in handling processes of cores and moulds with the material models and simulation methods developed in this dissertation. Both main deformation patterns of the top core at hand are predicted by the simulation and the deformations are in a similar range as the real cores. Therefore, this simulation can be utilised to optimise the gripping process. With this methodology, the developing process engineer at BMW AG could have foreseen the problem of the deformed cores before the gripper was built and could have improved the gripper design or the gripping force in simulation until the resulting deformations are in an acceptable range. A numerical optimisation would have saved time, money and energy compared to the state of the art trial and error process.

9 Conclusion and Future Work

Chemically-bound sand is utilised in foundries as moulds and cores in high volume for mass production. Typically, high-volume production processes and the involved materials are characterised in detail and optimised with simulation tools. The casting process itself is a good example. It can be optimised for mould filling, solidification, hot distortion, residual stresses and several more target properties. To achieve accurate results, a detailed knowledge of the mechanical behaviour and the involved boundary conditions is necessary for these simulations. This leads to a production process, which yields higher quality products at lower costs.

In contrast, production processes for chemically-bound cores are designed based on experience. This work contributes to the fundamental understanding of the mechanical behaviour of core materials with a focus on foundry sand, bound with silicates. I proposed testing methods, which systematically characterise the material properties necessary for FEM simulation of core materials. An impulse excitation test setup and a data processing algorithm has been developed to non-destructively acquire the elastic parameters for core materials. Furthermore, several novel bi- and triaxial testing methods have been devised to determine the failure surface of core materials with support points which are systematically distributed in the principal stress space.

Based on these support points a new probabilistic formulation of the Mohr-Coulomb criterion was proposed and implemented in an algorithm which evaluates FEM results for core fracture. With this algorithm the material model was experimentally validated by predicting the fracture force of cores with complex geometries and stress states.

I utilised these test setups to characterise the impact of key influences on the parameters of the material model and thus to extend the understanding of the mechanical behaviour of core materials. I determined the influence of the binder amount, the storage time and the humidity on the elastic properties, the failure surface and the creep behaviour.

In a last step, I showed with a technical case study from the BMW AG how the new simulative abilities can be utilised to improve and optimise production processes, which involve core production and handling.

The most important results of the experiments are summarised in the following.

Fracture statistics Core materials display brittle characteristics, even with organic binders. The binder bridges show smooth fracture surfaces, which is typical for brittle fracture. Furthermore, the fracture strength follows a Weibull distribution, which indicates that the weakest link theory applies which is a further characteristic of brittle fracture.

Therefore, the fracture strength is influenced by the loaded effective volume of the specimen. A higher effective volume leads to a lower fracture strength than a smaller effective volume. This effect has to be considered for any fracture stress calculations whether analytic or numerical. Based on FEM calculations, the effective volume of complex core geometries can be calculated by integrating the effective volume of the individual elements of the mesh. These findings apply to inorganic and organic binder systems.

Elastic parameters The elastic constants were determined with a test bench for impulse excitation, specifically designed for foundry cores. The Young's modulus and the Poisson ratio are increasing with the storage period after the core shooting. Furthermore, the binder amount has a near linear influence on the Young's modulus and Poisson ratio in the tested range. Increasing moisture is decreasing the Young's modulus, while the Poisson ratio remains approximately constant.

Failure surface I showed that the failure of core materials is described best with a Mohr-Coulomb criterion. A new failure criterion was proposed, which combines the weakest link theory and the Mohr-Coulomb criterion in one implicit equation. This equation combines the results of the statistical analysis and the Mohr-Coulomb failure criterion. For the first time, a validated material model can be implemented in FEM calculations to predict the fracture of foundry cores under complex stress states. A Mohr-Coulomb model has two parameters, the cohesion of the material and the friction angle. I studied the influence of the binder amount, the humidity and the storage time on these parameters and found that the cohesion of the material is a linear function of binder amount, while the friction angle remains constant. Furthermore, the cohesion of the material is rising in a logarithmic manner with the storage time, while the friction angle decreases with increasing storage time. Increasing moisture is decreasing the cohesion of the core, while the friction angle increases with the humidity.

Creep behaviour Core materials show a significant creep behaviour. In contrast to the brittle fracture behaviour without plasticity, inelastic deformations occur if cores are subjected to a constant load below the fracture strength. I showed that the creep behaviour is mainly influenced by the ratio of the load to the fracture strength. The creep of the material follows this ratio. If the fracture strength of a core is changed (e.g. due to rising humidity), the creep behaviour changes accordingly. Therefore, creep in foundry cores appears to be highly relevant for core storage and handling.

Future work The material characterisation in this dissertation provides a basic understanding of the mechanical behaviour of core material. All parameters for the basic material model proposed here can be determined experimentally. However, this can only be the beginning of a further in-depth analysis of the material properties. The research in this dissertation provides a set of tools to further characterise core materials. The basic model in this work assumed static material properties, independent of time. However, from other materials, like steel, we know that the strain rate has an effect on the material behaviour. This is especially interesting for core materials, since the decoring process after the casting is highly dynamic and could be simulated in the future. Additionally, the influence of the temperature during casting and its influence on the model parameters should be studied. This provides valuable information for a future decoring simulation. Furthermore, it is possible to adapt the novel weakest-link-based Mohr-Coulomb criterion to anisotropic materials, which will allow to model cores produced with additive manufacturing techniques, which are typically anisotropic.

In this dissertation, the influence of the sand and the grain shape on the model parameters has been kept constant. Schneider et al. show that the grain-size distribution and the shape of the individual grains have an impact on the macroscopic mechanical properties (Schneider et al., 2018). Studies on the macroscopic influence of the sand similar to the parameter studies with binder amount and storage conditions in this dissertation would be useful to choose the right sand for the whole life-cycle of the core.

The study of creep parameters in this dissertation shows a time-dependent behaviour, as well. Future work should focus more on the creep behaviour, due to its relevance for the industry. What parameters in the production process and the chemical components of the binder systems are influencing the creep behaviour? How long can cores bear their own weight without leaving the geometrical specifications? Based on the results of this dissertation more research is necessary to fully apply this knowledge in foundries. In my opinion, a unified theory of creep at room temperature and hot distortion during casting is possible as well, if the creep parameters are studied with respect to temperature.

The tools developed in this dissertation are able to show the benefits of mechanical simulations for foundry cores and to realise process improvements. Hopefully, this will lead to the necessary industrial and academic support to further develop these methods to fully model all processes in the life cycle of a core from the core shooting to the decoring.

A List of Figures

B List of Tables

C Bibliography

ABBO, A. J., A. V. LYAMIN, S. W. SLOAN and J. P. HAMBLETON (2011). A C2 continuous approximation to the Mohr–Coulomb yield surface. In: *International Journal of Solids and Structures* **48**.21, 3001–3010.

ABICHOU, T., C. H. BENSON and T. B. EDIL (2000). Foundry Green Sands as Hydraulic Barriers: Laboratory Study. In: *Journal of Geotechnical and Geoenvironmental Engineering* **126**.12, 1174–1183.

ASSMANN, B. and P. SELKE (2004). *Technische Mechanik Band 3: Kinematik und Kinetik*. **13**. Oldenburg Verlag.

ATRI, R., K. RAVICHANDRAN and S. JHA (1999). Elastic properties of in-situ processed Ti–TiB composites measured by impulse excitation of vibration. In: *Materials Science and Engineering: A* **271**.1-2, 150–159.

BAILEY, R. W. (1935). The Utilization of Creep Test Data in Engineering Design. In: *Proceedings of the Institution of Mechanical Engineers* **131**.1, 131–349.

BAKHTIYAROV, S., R. A. OVERFELT, A. SURYAWANSHI and J. CAPPS (2009). Numerical Simulations and Experimental Study of Hot Core Distortion Phenomenon in Aluminum Casting. In: *Volume 3*. ASMEDC, 1025–1034.

BARGAOUI, H., F. AZZOUZ, D. THIBAULT and G. CAILLETAUD (2017). Thermomechanical behavior of resin bonded foundry sand cores during casting. In: *Journal of Materials Processing Technology* **246**, 30–41.

BARNETT, R., P. HERMANN, J. WINGFIELD and C. CONNORS (1967). *Fracture of Brittle Materials under Transient Mechanical and Thermal Loading*. Ohio.

BASSALI, W. A. (1960). The transverse flexure of a thin circular plate subject to parabolic loading over a concentric ellipse. In: *ZAMP Zeitschrift für angewandte Mathematik und Physik* **11**.3, 176–191.

BAUER, H. (1991). *Wahrscheinlichkeitstheorie*. 4., völlig überarb. und neugestaltete Aufl. De-Gruyter-Lehrbuch. Berlin: de Gruyter.

BEELEY, P. R. (2001). *Foundry technology*. 2. ed. Oxford: Butterworth-Heinemann. URL: `http://site.ebrary.com/lib/alltitles/docDetail.action?docID=10175602`.

BENNETT, J. (1991). *A Weibull Brittle Material Failure Model for the ABAQUS Computer Program*. Tech. rep. NEW Mexico 87545: Los Alamos National Laboratory.

BENZ, T. and R. SCHWAB (2008). A quantitative comparison of six rock failure criteria. In: *International Journal of Rock Mechanics and Mining Sciences* **45**.7, 1176–1186.

BÉSUELLE, P., J. DESRUES and S. RAYNAUD (2000). Experimental characterisation of the localisation phenomenon inside a Vosges sandstone in a triaxial cell. In: *International Journal of Rock Mechanics and Mining Sciences* **37**.8, 1223–1237.

BIGONI, D. and A. PICCOLROAZ (2004). Yield criteria for quasibrittle and frictional materials. In: *International Journal of Solids and Structures* **41**.11-12, 2855–2878.

BÜHRIG-POLACZEK, A. and H. TRÄGER (2010). Foundry Technology. In: *Ullmann's encyclopedia of industrial chemistry*. **1**. Chichester: Wiley, 271.

CAMPBELL, J. (2015). *Complete Casting Handbook: Metal Casting Processes, Metallurgy, Techniques and Design*. Second Edition. Amsterdam: Elsevier. URL: `http://www.sciencedirect.com/science/book/9780444635099`.

CAYLAK, I. and R. MAHNKEN (2010). Thermomechanical characterisation of cold box sand including optical measurements. In: *International Journal of Cast Metals Research* **23**.3, 176–184.

CHUANG, T.-J. (1986). Estimation of power-law creep parameters from bend test data. In: *Journal of Materials Science* **21**.1, 165–175.

COLMENARES, L. and M. ZOBACK (2002). A statistical evaluation of intact rock failure criteria constrained by polyaxial test data for five different rocks. In: *International Journal of Rock Mechanics and Mining Sciences* **39**.6, 695–729.

COMMON, J. W. (1940). 'Core Handling Machine'. US2270509.

CONEV, M., I. VASKOVÁ, M. HRUBOVČÁKOVÁ and P. HAJDÚCH (2017). Decoring Behaviour of Chosen Moulding Materials with Alkali Silicate Based Inorganic Binders. In: *Archives of Metallurgy and Materials* **62**.2, 703–706.

CZERWINSKI, F., M. MIR and W. KASPRZAK (2015). Application of cores and binders in metalcasting. In: *International Journal of Cast Metals Research* **28**.3, 129–139.

DANZER, R., P. SUPANCIC, J. PASCUAL and T. LUBE (2007). Fracture statistics of ceramics – Weibull statistics and deviations from Weibull statistics. In: *Engineering Fracture Mechanics* **74**.18, 2919–2932.

DANZER, R. (1992). A general strength distribution function for brittle materials. In: *Journal of the European Ceramic Society* **10**.6, 461–472.

DASSAULT SYSTEMS (2020). SIMULIA User Assistance 2020. Accessed: 2020-12-22. URL: `https://help.3ds.com/2020/english/dssimulia_established/simacaeelmrefmap/simaelm-c-solidcont.htm?contextscope=all`.

DEGARMO, E. P., J. T. BLACK and R. A. KOHSER (2008). *Materials and Processes in Manufacturing*. 10. ed. New York NY: Wiley.

DEHLER, W. and J. F. LABUZ (2007). Stress Path Testing of an Anisotropic Sandstone. In: *Journal of Geotechnical and Geoenvironmental Engineering* **133**.1, 116–119.

DIN 843-2 (2016). *Hochleistungskeramik - Mechanische Eigenschaften monolithischer Keramik bei Raumtemperatur - Teil 2: Bestimmung des Elastizitätsmoduls, Schubmoduls und der Poissonzahl; Deutsche Fassung EN 843-2:2006.*

DIN 8580 (2003). *DIN 8580: Fertigungsverfahren - Begriffe, Einteilung*. Norm.

DINI, G., M. LANZETTA, M. SANTOCHI, G. TANTUSSI and A. FRANCO (1999). An Approach to Selective Laser Sintering (SLS) of Pre-Coated Sands for Shell Moulding. In: *AMST '99*. Ed. by E. KULJANIC. International Centre for Mechanical Sciences, Courses and Lectures. Vienna and s.l.: Springer Vienna, 545–556.

DONG, S., Y. IWATA, H. HOHJO, H. IWAHORI, T. YAMASHITA and H. HIRANO (2010). Shell Mold Cracking and Its Prediction during Casting of AC4C Aluminum Alloy. In: *MATERIALS TRANSACTIONS* **51**.8, 1420–1427.

DRUCKER, D. C. and W. PRAGER (1952). Soil mechanics and plastic analysis or limit design. In: *Quarterly of Applied Mathematics* 10, 141–148.

EHLERS, W. (1993). Constitutive Equations for Granular Materials in Geomechanical Context. In: *Continuum Mechanics in Environmental Sciences and Geophysics*. Ed. by K. HUTTER. **29**. Vienna: Springer Vienna, 313–402.

EHLERS, W. and W. VOLK (1997). On shear band localization phenomena of liquid-saturated granular elastoplastic porous solid materials accounting for fluid viscosity and micropolar solid rotations. In: *Mechanics of Cohesive-frictional Materials* **2**.4, 301–320.

ETTEMEYER, F., M. SCHWEINEFUSS, P. LECHNER, J. STAHL, T. GRESS, J. KAINDL, L. DURACHA, W. VOLK and D. GÜNTHER (2021). Characterisation of the decoring behaviour of inorganically bound cast-in sand cores for light metal casting. In: *Journal of Materials Processing Technology, (In review 2020.12.12)*.

ETTEMEYER, F., P. LECHNER, T. HOFMANN, H. ANDRÄ, M. SCHNEIDER, D. GRUND, W. VOLK and D. GÜNTHER (2019). Digital sand core physics: Predicting physical properties of sand cores by simulations on digital microstructures. In: *International Journal of Solids and Structures*.

FAIRHURST, C. (1964). On the validity of the 'Brazilian' test for brittle materials. In: *International Journal of Rock Mechanics and Mining Sciences & Geomechanics Abstracts* **1**.4, 535–546.

FAN, Z. T., N. Y. HUANG and X. P. DONG (2004). In house reuse and reclamation of used foundry sands with sodium silicate binder. In: *International Journal of Cast Metals Research* **17**.1, 51–56.

FERRARIS, M., M. SALVO, S. RIZZO, V. CASALEGNO, S. HAN, A. VENTRELLA, T. HINOKI and Y. KATOH (2012). Torsional Shear Strength of Silicon Carbide Components Pressurelessly Joined by a Glass-Ceramic. In: *International Journal of Applied Ceramic Technology* **9**.4, 786–794.

FETT, T., G. RIZZI, E. ERNST, R. MÜLLER and R. OBERACKER (2007). A 3-balls-on-3-balls strength test for ceramic disks. In: *Journal of the European Ceramic Society* **27**.1, 1–12.

FUCHS, G. (2016). 'Entwicklung eines Prüfstandes zur akustischen Messung von elastischen Konstanten anorganischer Formstoffe'. MA thesis. TU München.

GALLES, D. and C. BECKERMANN (2015). Effect of sand dilation on core expansion during steel casting. In: *IOP Conference Series: Materials Science and Engineering* **84**, 012022.

GAMISCH, M. (2002). Mechanisches Entkernen von Al-Gussteilen mit geringer Beanspruchung des Gussteils. In: *Giesserei Rundschau* **49**, 43–45.

GARCIA, D. (2010). Robust smoothing of gridded data in one and higher dimensions with missing values. In: *Computational Statistics and Data Analysis* **54**, 1167–1178.

GAUTAM, T. P. (2018). Cohesive Soils. In: *Encyclopedia of Engineering Geology*. Ed. by P. T. BOBROWSKY and B. MARKER. Encyclopedia of Earth Sciences Series. Cham: Springer International Publishing, 161–162.

GODFREY, D. J. (1985). Fabrication, formulation, mechanical properties, and oxidation of sintered Si 3 N 4 ceramics using disc specimens. In: *Materials Science and Technology* **1**.7, 510–515.

GONG, J. (2003). Correlation between Weibull moduli for tensile and bending strength of brittle ceramics: a numerical simulation analysis based on a three-parameter Weibull distribution. In: *Journal of materials science* 38.

GRANAT, K., D. NOWAK, M. PIGIEL, M. STACHOWICZ and R. WIKIERA (2008). The influence of water glass on the properties of microwave cured molding sands. In: *Archives of Foundry Engineering* **8**.

GRIEBEL, B. (2016). *Einflussanalyse anorganisch gebundener Formstoffe*. Duisburg.

GRIEBEL, B., D. BRECHEISEN, R. RAMAKRISHNAN and W. VOLK (2016). Optical Measurement Techniques Determine Young's Modulus of Sand Core Materials. In: *International Journal of Metalcasting* **10**.4, 524–530.

GROSS, D. and T. SEELIG (2011). Einige Grundlagen der Festkörpermechanik. In: *Bruchmechanik*. Ed. by D. GROSS and T. SEELIG. Berlin, Heidelberg: Springer Berlin Heidelberg, 5–39.

GROSS, D. and T. SEELIGER (2016). *Bruchmechanik: Mit einer Einführung in die Mikromechanik*. 6. Auflage. Lehrbuch. Berlin, Heidelberg: Springer Vieweg. URL: `http://dx.doi.org/10.1007/978-3-662-46737-4`.

GROTE, K.-H. (2007). *Dubbel: Taschenbuch für den Maschinenbau*. 22. Aufl. s.l.: Springer-Verlag. URL: `http://search.ebscohost.com/login.aspx?direct=true&scope=site&db=nlebk&db=nlabk&AN=261907`.

HAKE, E. and K. MESKOURIS (2007). *Statik der Flächentragwerke: Einführung mit vielen durchgerechneten Beispielen*. 2., korrigierte Auflage. Springer-Lehrbuch. Berlin, Heidelberg: Springer-Verlag Berlin Heidelberg. URL: `http://dx.doi.org/10.1007/978-3-540-72624-1`.

HANS-JÜRGEN WARNECKE (1993). *Einfuhrung in die Fertigungstechnik*. Stuttgart: B. G. Teubner.

HAR, J. and K. T. KUMAR (2012). Continuum Mechanics. In: *Advances in Computational Dynamics of Particles, Materials and Structures*. Ed. by J. HAR and K. K. TAMMA. Chichester, UK: John Wiley & Sons, Ltd, 173–266.

HARPER, J. and J. DORN (1957). Viscous creep of aluminum near its melting temperature. In: *Acta Metallurgica* **5**.11, 654–665.

HARTMANN, C., J. WANG, D. OPRITESCU and W. VOLK (2018). Implementation and evaluation of optical flow methods for two-dimensional deformation measurement in comparison to digital image correlation. In: *Optics and Lasers in Engineering* **107**, 127–141.

HEARN, E. J. (1997). Introduction to Advanced Elasticity Theory. In: *Mechanics of Materials 2*. Elsevier, 220–299.

HERRING, C. (1950). Diffusional Viscosity of a Polycrystalline Solid. In: *Journal of Applied Physics* **21**.5, 437–445.

HILL, R. (1950). C. A theory of the plastic bulging of a metal diaphragm by lateral pressure. In: *The London, Edinburgh, and Dublin Philosophical Magazine and Journal of Science* **41**.322, 1133–1142.

HOLT, R. M., T. E. UNANDER and C. J. KENTER (1993). Constitutive mechanical behaviour of synthetic sandstone formed under stress. In: *International Journal of Rock Mechanics and Mining Sciences & Geomechanics Abstracts* **30**.7, 719–722.

ILER, R. K. (1979). *The chemistry of silica: Solubility, polymerization, colloid and surface properties, and biochemistry*. New York, NY: Wiley.

IZDEBSKA-SZANDA, I., A. BALIŃSKI and M. ANGRECKI (2012). Evaluation of Reclamability of Molding Sands with New Inorganic Binders. In: *Archives of Foundry Engineering* **12**.2, 161.

IZDEBSKA-SZANDA, I., F. PEZARSKI and E. SMOLUCHOWSKA (2008). Investigating the kinetics of the binding process in moulding sands using new, environment-friendly, inorganic binders. In: *Achieves of Foundry Engineering* **8**.2, 61–66.

KIESLINGER, A. (1962). Zur Kohäsion des Sandes (Unfälle und Unfallverhütung in Sandgruben). In: *Zeitschrift der Deutschen Geologischen Gesellschaft* **114**, 151–152. URL: `http://www.schweizerbart.de//papers/zdgg%5C_alt/detail/114/51408/Zur%5C_Kohasion%5C_des%5C_Sandes%5C_Unfalle%5C_und%5C_Unfallverhutung%5C_in%5C_Sandgruben`.

KOBLAR, D. and M. BOLTEŽAR (2013). Evaluation of the Frequency-Dependent Young's Modulus and Damping Factor of Rubber from Experiment and Their Implementation in a Finite-Element Analysis. In: *Experimental Techniques* **141**.1, n/a–n/a.

KOGEL, J. E. (2006). *Industrial minerals & rocks: Commodities, markets, and uses*. 7th ed. Littleton: Society for Mining, Metallurgy, and Exploration.

KONZACK, C. (2013). Entkernen von Gussprototypen mit Stoßwellen: Das Säubern von Gussteilen mit der Stoßwellentechnologie verkürzt die Produktionszeit bei ACTech deutlich. In: *GIESSEREI* **2013**.11, 62–63.

KOVARI, K. and A. TISA (1975). Multiple Failure State and Strain Controlled Triaxial tests. In: *Rock Mechanics and Rock Engineering* **7**.1, 17–33.

LAMON, J. (1988). Ceramics Reliability: Statistical Analysis of Multiaxial Failure Using the Weibull Approach and the Multiaxial Elemental Strength Model. In: *The Amercian Society of Mechanical Engineers*.

LANDUA, W. and J. MÜLLER (1988). 'Core or Shell Bundling Machine'. US 4744853.

LANGDON, T. G. (2000). Identifiying creep mechanisms at low stresses. In: *Materials Science and Engineering: A* **283**.1-2, 266–273.

LECHNER, P., C. HARTMANN, F. ETTEMEYER and W. VOLK (2021). A Plane Stress Failure Criterion for Inorganically-Bound Core Materials. In: *Materials* **14**.2.

LECHNER, P., P. FILIPPOV, N. KRASCHIENSKI, F. ETTEMEYER and W. VOLK (2019). A Novel Method for Measuring Elastic Modulus of Foundry Silicate Binders. In: *International Journal of Metalcasting* **34**.3, 38.

LECHNER, P., G. FUCHS, C. HARTMANN, F. STEINLEHNER, F. ETTEMEYER and W. VOLK (2020). Acoustical and Optical Determination of Mechanical Properties of Inorganically-Bound Foundry Core Materials. In: *Materials* **13**.11, 2531. URL: `https://doi.org/10.3390/ma13112531`.

LECHNER, P., J. STAHL, F. ETTEMEYER, B. HIMMEL, B. TANANAU-BLUMENSCHEIN and W. VOLK (2018). Fracture Statistics for Inorganically-Bound Core Materials. In: *Materials (Basel, Switzerland)* **11**.11.

LECHNER, P., J. STAHL, C. HARTMANN, F. ETTEMEYER and W. VOLK (2021). Mohr–Coulomb characterisation of inorganically-bound core materials. In: *Journal of Materials Processing Technology* **296**, 117214.

LECKIE, F. A. and D. J. D. BELLO (2009). Failure Criteria. In: *Strength and Stiffness of Engineering Systems*. Ed. by D. J. BELLO and F. A. LECKIE. Mechanical Engineering Series. Boston, MA: Springer US, 1–15.

LEE, R. W. (1983). Automated Storage and Handling of Cores and Moulds in a Foundry. In: *Proceedings of the Institution of Mechanical Engineers, Part B: Management and engineering manufacture* **197**.1, 7–18.

LI, D. and L. N. Y. WONG (2013). The Brazilian Disc Test for Rock Mechanics Applications: Review and New Insights. In: *Rock Mechanics and Rock Engineering* **46**.2, 269–287.

LIU, F., Z. FAN, X. LIU, H. WANG and J. HE (2014). Research on Humidity Resistance of Sodium Silicate Sand Hardened by Twice Microwave Heating Process. In: *Materials and Manufacturing Processes* **29**.2, 184–187.

LOTTER, B. and H.-P. WIENDAHL (2006). *Montage in der industriellen Produktion: Ein Handbuch für die Praxis ; mit 16 Tabellen*. VDI-Buch. Berlin, Heidelberg: Springer-Verlag Berlin Heidelberg. URL: `http://dx.doi.org/10.1007/3-540-36669-5`.

LUDING, S., M. LÄTZEL, W. VOLK, S. DIEBELS and H. J. HERRMANN (2001). From discrete element simulations to a continuum model. In: *Computer Methods in Applied Mechanics and Engineering* **191**.1-2, 21–28.

MAJOR-GABRYŚ, K. and S. M. DOBOSZ (2007). High-temperature expansion and knock-out properties of moulding sands with water glass. In: *Archives of Foundry Engineering* **7**.1, 127–130.

MANG, H. A. and G. HOFSTETTER (2013). *Festigkeitslehre*. Berlin, Heidelberg: Springer Berlin Heidelberg.

MASOUDI ALAVI, A. (2019). *Strukturelle Phasenanalyse von chemischen Prozessadditiven in der Silikat-Industrie: Untersuchung der Wechselwirkung von Alkali-Wassergläsern mit Aluminium-Tetrametaphosphat*. BestMasters. URL: `https://doi.org/10.1007/978-3-658-25694-4`.

MATHWORKS (2016). *Statistics and Machine Learning Toolbox User's Guide*.

MCINTOSH, G. J. (2013). Theoretical investigations into the nucleation of silica growth in basic solution part I–ab initio studies of the formation of trimers and tetramers. In: *Physical chemistry chemical physics : PCCP* **15**.9, 3155–3172.

MISES, r. (1913). Mechanik der festen Körper im plastisch-deformablen Zustand. In: *Nachrichten von der Gesellschaft der Wissenschaften zu Göttingen*.

MITCHELL, J. K. and K. SOGA (2005). *Fundamentals of soil behavior*. 3. ed. Hoboken, NJ: Wiley. URL: `http://www.loc.gov/catdir/enhancements/fy0617/2004025690-b.html`.

MORRELL, R. (1998). *Biaxial flexural strength testing of ceramic materials*. National Physical Laboratory Teddington, United Kingdom. URL: `https://www.researchgate.net/publication/236381914_Biaxial_Flexure_Test_for_Ceramics`.

MÜLLERSCHÖN, H. (2000). 'Spannungs-Verformungsverhalten granularer Materialien am Beispiel von Berliner Sand'. Dissertation. Stuttgart: Universität Stuttgart.

MURAKAMI, S. and S. IWATSUKI (1969). Transient creep of circular cylindrical shells. In: *International Journal of Mechanical Sciences* **11**.11, 897–912.

MUSCHNA, M. (2020). Accessed: 2020-12-22. URL: `http://www.mgm-foundry.de/de/produkte/kernhandling-systeme/`.

NI, C.-j., G.-c. LU, Q.-d. ZHANG, T. JING, J.-j. WU, L.-l. YANG and Q.-f. WU (2016). Influence of core box vents distribution on flow dynamics of core shooting process based on experiment and numerical simulation. In: *China Foundry* **13**.1, 22–29.

PABST, W. and E. GREGOROVA (2013). Elastic Properties of Silica Polymorphs - A review. In: *Cermics - Silikaty* 57, 167–184.

PALACHY, T., P. PADEVET and M. POLAK (2009). Comparison of Two Experimental Techniques for Determination of Young's Modulus of Concrete Specimens. In: *Proceedings of the 5th WSEAS International Conference on Applied and Theoretical Mechanics (MECHANICS '09)*.

PAN, B., K. LI and W. TONG (2013). Fast, robust and accurate digital image correlation calculation without redundant computations. In: *Experimental Mechanics* **53** (7), 1277–1289.

PASTERNAK, M. (1989). *Fachkunde Gießereitechnik: Mit 17 Tab.* 2., unveränd. Aufl. Leipzig: Dt. Verl. für Grundstoffindustrie.

POLZIN, H. (2014). *Inorganic binders: For mould and core production in the foundry*. 1. Aufl. s.l.: Fachverlag Schiele Schön. URL: `http://gbv.eblib.com/patron/FullRecord.aspx?p=1896368`.

QUAYUM, M. S., X. ZHUANG and T. RABCZUK (2015). Computational model generation and RVE design of self-healing concrete. In: *Frontiers of Structural and Civil Engineering* **9**.4, 383–396.

RAMAKRISHNAN, R. (2016). '3-D-Drucken mit einem anorganischen Formstoffsystem'. Dissertation. München: Technische Universität München.

RAMAKRISHNAN, R., W. VOLK, B. GRIEBEL and D. GÜNTHER (2014). 3D Printing of Inorganic Sand Moulds for Casting Applications. In: *Advanced Materials Research* 1018, 441–449.

RAO, T. V. R. (2003). *Metal Casting: Principles and Practice*. New Delhi: New Age International Publishers.

ROEBBEN, G., B. BOLLEN, A. BREBELS, J. VAN HUMBEECK and O. VAN DER BIEST (1997). Impulse excitation apparatus to measure resonant frequencies, elastic moduli, and internal friction at room and high temperature. In: *Review of Scientific Instruments* **68**.12, 4511–4515.

ROOCH, A. (2014). *Statistik für Ingenieure: Wahrscheinlichkeitsrechnung und Datenauswertung endlich verständlich*. Springer-Lehrbuch. Berlin: Springer Spektrum. URL: `http://dx.doi.org/10.1007/978-3-642-54857-4`.

ROSCOE, K. H. and H. B. POOROOSHASB (1963). A Theoretical and Experimental Study of Strains in Triaxial Compression Tests on Normally Consolidated Clays. In: *Géotechnique* **13**.1, 12–38.

SAHADE, V., A. DHAKE, N. DIXIT and S. P. DESHPAND (2016). Magnetic Mould Casting: Methodology and Comparison with Traditional Sand Casting Process. In: *2nd International Conference on Advances in Mechanical Engineering(ICAME-2016)* **2016**.Vol. 3, Special Issue 1.

SCHNEIDER, M., T. HOFMANN, H. ANDRÄ, P. LECHNER, F. ETTEMEYER, W. VOLK and H. STEEB (2018). Modelling the microstructure and computing effective elastic properties of sand core materials. In: *International Journal of Solids and Structures* **143**, 1–17.

SCHOLZ, C. H. (1968). Mechanism of creep in brittle rock. In: *Journal of Geophysical Research* **73**.10, 3295–3302.

SCHWICKAL, H. H. (2015). 'Regeneration anorganisch gebundener Kernaltsande auf Basis einer erweiterten chemischen Formstoffprüfung'. Dissertation. München: Technische Universität München.

SHETTY, D. K., A. R. ROSENFIELD, W. H. DUCKWORTH and P. R. HELD (1983). A Biaxial-Flexure Test for Evaluating Ceramic Strengths. In: *Journal of the American Ceramic Society* **66**.1, 36–42.

SLOAN, S. W. and J. R. BOOKER (1986). Removal of singularities in tresca and mohr-coulomb yield functions. In: *Communications in Applied Numerical Methods* **2**.2, 173–179.

SOBCZYK, M. (2008). 'Untersuchung zur Nutzung der Vakuumtrocknungshärtung für die Herstellung und den Einsatz magnesiumsulfatgebundener Kerne für den Leichtmetallguss'. Dissertation. Magdeburg: Universität Magdeburg.

STACEY, T. R. (1980). A simple device for the direct shear-strength testing of intact rock. In: *Journal of the Southern African Institute of Mining and Metallurgy* **80**.3, 129–130.

STACHOWICZ, M., K. GRANAT and D. NOWAK (2011). Influence of water-glass grade and quantity on residual strength of microwave-hardened moulding sands. Part 2. In: *Archives of Foundry Engineering* **11**.2, 143–148.

STAUDER, B. J., M. BERBIC and P. SCHUMACHER (2019). Mohr-Coulomb failure criterion from unidirectional mechanical testing of sand cores after thermal exposure. In: *Journal of Materials Processing Technology* **274**, 116274.

STAUDER, B. J., H. HARMUTH and P. SCHUMACHER (2018a). De-agglomeration rate of silicate bonded sand cores during core removal. In: *Journal of Materials Processing Technology* **252**, 652–658.

STAUDER, B. J., H. HARMUTH and P. SCHUMACHER (2018b). De-agglomeration rate of silicate bonded sand cores during core removal. In: *Journal of Materials Processing Technology* **252**, 652–658.

STAUDER, B. J., H. KERBER and P. SCHUMACHER (2016). Foundry sand core property assessment by 3-point bending test evaluation. In: *Journal of Materials Processing Technology* **237**, 188–196.

STRAUSS, K. (2014). *Applied Science in the Casting of Metals*. Kent: Elsevier Science.

T. N. KESHISHYAN, A. I. RABUKHIN, M. M. SMIRNOVA and AND V. G. DOROFEEV (1975). METHOD OF DETERMINATION OF STATIC MODULUS OF ELASTICITY. In: *Glass and Ceramics* 32(6), 380–382.

THORBORG, J., S. KUMAR, I. WAGNER and J. C. STURM (2020). The virtual core - modelling and optimization of core manufacturing and application. In: *IOP Conference Series: Materials Science and Engineering* **861**, 012004.

TOGNANA, S., W. SALGUEIRO, A. SOMOZA and A. MARZOCCA (2010). Measurement of the Young's modulus in particulate epoxy composites using the impulse excitation technique. In: *Materials Science and Engineering: A* **527**.18-19, 4619–4623.

VOLK, W. (1999). *Untersuchung des Lokalisierungsverhaltens mikropolarer poröser Medien mit Hilfe der Cosserat Theorie*.

WALLENHORST, C. (2010). Grundlagen zum Verständnis der anorganischen Kernfertigung. In: *GIESSEREI-PRAXIS*, 181–184.

WATERS, T. F. (1996). *Fundamentals of Manufacturing For Engineers*. Reprinted. London: UCL Press.

WEIBULL, W. (1939). A Statistical Theory of the Strength of Materials. In: *Swedish Institute for Engineering Reseach*.

WEIBULL, W. (1951). A Statistical Distribution Function of Wide Applicability. In: *Journal of Applied Mechanics*.

WEISSBACH, W. (2004). *Werkstoffkunde und Werkstoffprüfung*. 15., überarbeitete und erweiterte Auflage. Viewegs Fachbücher der Technik. Wiesbaden and s.l.: Vieweg+Teubner Verlag. URL: `http://dx.doi.org/10.1007/978-3-322-93987-6`.

WEISSENBEK, E., T. KAUTZ, J. BROTZKI and J. MÜLLER (2011). Zylinderkopffertigung der Zukunft. In: *MTZ - Motortechnische Zeitschrift* **72**.6, 484–489. URL: `https://doi.org/10.1365/s35146-011-0111-6`.

WINARTOMO, B., U. VROOMEN, A. BÜHRIG-POLACZEK and M. PELZER (2005). Multiphase modelling of core shooting process. In: *International Journal of Cast Metals Research* **18**.1, 13–20.

WITH, G. and H. H. M. WAGEMANS (1989). Ball-on-Ring Test Revisited. In: *Journal of the American Ceramic Society* **72**.8, 1538–1541.

YOSHIDA, F. (2018). Description of non-linear unloading curve and closure of cyclic stress-strain loop based on Y-U model. In: *Materials & Design* **1063**, 012094.

YOUN, H. and F. TONON (2010). Multi-stage triaxial test on brittle rock. In: *International Journal of Rock Mechanics and Mining Sciences* **47**.4, 678–684.

ZARETSKIY, L. (2016). Modified Silicate Binders New Developments and Applications. In: *International Journal of Metalcasting* **10**.1, 88–99.

ZHAO, B., D. LIU and Q. DONG (2011). Experimental research on creep behaviors of sandstone under uniaxial compressive and tensile stresses. In: *Journal of Rock Mechanics and Geotechnical Engineering* **3**, 438–444. URL: `http://www.sciencedirect.com/science/article/pii/S1674775515301426`.

D Appendix

D.1 Raw data

Table D.1: Raw data included in figure 5.1 and 5.2.

	10 s	24 h
1.5 %	3.08	4.10
2.0 %	4.30	5.76
2.5 %	4.88	7.57

(a) Young's modulus in GPa.

	10 s	24 h
1.5 %	0.108	0.178
2.0 %	0.100	0.237
2.5 %	0.182	0.260

(b) Poisson ratio.

Table D.2: Raw data included in figure 5.3.

10 %	25 %	40 %	60 %
6.04	6.04	6.05	3.12

(a) Young's modulus in GPa.

10 %	25 %	40 %	60 %
0.235	0.234	0.248	-

(b) Poisson ratio.

Table D.3: Raw data included in figure 5.4.

IN-1	IN-2	OR-1	OR-2	OR-3
5.76	6.36	3.62	3.89	3.99

(a) Young's modulus in GPa.

IN-1	IN-2	OR-1	OR-2	OR-3
1.99 e+03	2.14 e+03	1.06 e+03	1.18 e+03	1.53 e+03

(b) Young's modulus normalised with tensile strength.

Table D.4: Raw data included in figure 6.18 - 6.21.

	10 s	120 s	24 h
1.5 %	0.903 (18.1)	1.46 (14.1)	2.20 (12.1)
2.0 %	1.27 (16.9)	2.10 (26.5)	3.12 (25.7)
2.5 %	1.55 (16.1)	2.42 (44.8)	4.38 (26.0)

(a) Tensile stress in MPa. The Weibull shape parameter is added in parentheses.

	10 s	120 s	24 h
1.5 %	2.49 (-)	2.70 (13.7)	3.24 (14.8)
2.0 %	3.42 (-)	3.83 (16.7)	4.90 (16.7)
2.5 %	4.57 (-)	5.30 (20.9)	7.24 (32.4)

(b) Compressive stress in MPa. The Weibull shape parameter is added in parentheses.

	10 s	120 s	24 h
1.5 %	0.91	1.23	1.63
2.0 %	1.38	1.87	2.31
2.5 %	1.49	2.06	3.07

(c) Cohesion stress in MPa.

	10 s	120 s	24 h
1.5 %	37.3	28.9	22.2
2.0 %	41.1	26.9	21.8
2.5 %	35.3	29.2	18.8

(d) Friction angle in deg.

Table D.5: Raw data included in figure 6.22.

10 %	25 %	40 %	60 %
3.31 (43.7)	2.95 (60.9)	3.26 (48.7)	0.99 (38.4)

(a) Tensile stress in MPa. The Weibull shape parameter is added in parentheses.

10 %	25 %	40 %	60 %
5.30 (23.4)	4.88 (24.9)	4.90 (25.1)	1.91 (15.3)

(b) Compressive stress in MPa. The Weibull shape parameter is added in parentheses.

10 %	25 %	40 %	60 %
2.41	2.11	2.23	0.83

(c) Cohesion in MPa.

10 %	25 %	40 %	60 %
20.7	19.6	16.9	27.3

(d) Friction angle in deg.

D.2 Student Theses

The following student research projects were conducted within the scope of this doctoral thesis at the Chair of Metal Forming and Casting (utg) at the Technical University of Munich (TUM). The processing, evaluation, interpretation, and presentation of results arose under my scientific guidance. While no results have been incorporated directly into this thesis, the methods and the knowledge gained in these research projects have been very important for the success of this dissertation. I would like to express my sincere gratitude to all students for their contribution.

Name	**Type**	**Title (Year)**
Luber, A.	Student Thesis	Messung des E-Moduls anorganischer Bindersysteme mittels 3-Punkt-Biegeversuch (2017)
Kraschienski, N.	Bachelor’s Thesis	Young’s Modulus of Silicate Binders in Foundry Cores (2017)
Fuchs, G.	Master’s Thesis	Entwicklung eines Prüfstandes zur akustischen Messung von elastischen Konstanten anorganischer Formstoffe (2019)
Reyes Barriga, F.	Master’s Thesis	Design and Test of a Specimen for Validation of Material Models of Inorganically-bounded Foundry Cores (2019)
Binder, S.	Student Thesis	Simulation zur inversen Materialcharakterisierung von anorganischen Formstoffen (2019)